

MEASURING AIR-WATER INTERFACIAL AREAS: CONTRIBUTIONS OF
CAPILLARY AND FILM DOMAINS IN NATURAL POROUS MEDIA

Juliana Botelho Araújo

Copyright © Juliana Araujo 2014

A Dissertation Submitted to the Faculty of the

DEPARTMENT OF SOIL, WATER, AND ENVIRONMENTAL SCIENCE

In Partial Fulfillment of the Requirements

For the Degree of

DOCTOR OF PHILOSOPHY

In the Graduate College

THE UNIVERSITY OF ARIZONA

2014

THE UNIVERSITY OF ARIZONA
GRADUATE COLLEGE

As members of the Dissertation Committee, we certify that we have read the dissertation prepared by Juliana Botelho Araújo, titled “Measuring Air-Water Interfacial Areas: Contributions Of Capillary And Film Domains In Natural Porous Media” and recommend that it be accepted as fulfilling the dissertation requirement for the Degree of Doctor of Philosophy.

_____ Date: (July 7, 2014)
Mark L. Brusseau

_____ Date: (July 7, 2014)
Marcel G. Schaap

_____ Date: (July 7, 2014)
Markus Tuller

Final approval and acceptance of this dissertation is contingent upon the candidate's submission of the final copies of the dissertation to the Graduate College.

I hereby certify that I have read this dissertation prepared under my direction and recommend that it be accepted as fulfilling the dissertation requirement.

_____ Date: (July 7, 2014)
Dissertation Director: Dr. Mark L. Brusseau

STATEMENT BY AUTHOR

This dissertation has been submitted in partial fulfillment of the requirements for an advanced degree at the University of Arizona and is deposited in the University Library to be made available to borrowers under rules of the Library.

Brief quotations from this dissertation are allowable without special permission, provided that an accurate acknowledgement of the source is made. Requests for permission for extended quotation from or reproduction of this manuscript in whole or in part may be granted by the copyright holder.

SIGNED: Juliana Botelho de Araújo

ACKNOWLEDGMENTS

I would like to express my utmost gratitude to Dr. Mark Brusseau for his mentorship, and guidance. His patience and helpful discussions have been instrumental throughout this journey. Also, I would like to extend my gratitude to the members of my defense committee Dr. Markus Tuller and Dr. Marcel G. Schaap for their much appreciated insightful discussions, and laboratory assistance. Funding for this work was provided from the Superfund Research Program and is greatly appreciated.

I would especially like to acknowledge the beam line staff of GSECars at the Argonne National Laboratory, and Dr. Mark Rivers and Nancy Lazaraz for their time and support in Chicago. Also, my gratitude to Matthew Narter for guiding me through the tomography experiments process at the synchrotron facility and Dr. Jon Mainhagu for his assistance in the tomography column design. I am especially thankful to Asma El Ouni and Dr. Hua Zhong for their endless assistance and camaraderie during the sleepless nights at the synchrotron facility. I am appreciative of the support received from everyone in the Contaminant Transport lab.

Most importantly I would like to thank both my parents Marcelo and Ana Vitória for being an endless source of inspiration and believing that I could one day accomplish this endeavor. I am indebted to my family, and those who have become family along the way, for their kindness and wisdom.

TABLE OF CONTENTS

ABSTRACT	6
CHAPTER 1: INTRODUCTION.....	8
CHAPTER 2: PRESENT STUDY.....	19
REFERENCES.....	31
APPENDICES.....	36
APPENDIX A: Image Segmentation For Determining Total And Capillary Air-Water Interfacial Areas In Natural Porous Media.....	36
APPENDIX B: Sequential Image Segmentation Approach For Determining Total And Capillary Air-Water Interfacial Areas In Natural Porous Media.....	90
APPENDIX C: Simulation on the Effects of Surface Areas on Capillary Interfacial Area Behavior.....	119
APPENDIX D: Determination of Film, Capillary, and Total Air-Water Interfacial Area Using X-Ray Microtomography.....	131
APPENDIX E: Comparison Of Tracer-Based Methods For Measuring Air-Water Interfacial Area In Porous Media.....	167
APPENDIX F: Porous Media Characterization.....	215

ABSTRACT

The air-water interface in variably saturated porous media is recognized to influence interfacial retention of organic and inorganic contaminants, and mediate various mass-transfer processes. The formation and presence of water films commonly solvating the surfaces of soil/sediment grains in unsaturated systems, as well as their impact on flow and retention processes have been of sustained interest. X-ray microtomography was used to measure air-water interfacial area at multiple wetting-phase saturations for natural porous media. First, a study was conducted to evaluate image-processing procedures suitable for characterizing fluids and associated interfaces in natural porous media. A simple method was developed for the analysis of all phases in the system, using global threshold for phase identification and combination of binary files (M1). This method was then compared to a simultaneous multiphase segmentation approach using locally adaptive threshold selection (M2). Both methods were used to process data sets comprised of multiple drainage steps for water-saturated packed columns imaged via synchrotron x-ray microtomography. The results of both methods were evaluated based on comparison of values determined for porosity and specific solid surface area to independently measured porosity and specific solid surface areas. The results show both methods are suitable for determination of total air-water interfacial area, which requires characterization of only the non-wetting phase. Conversely, determination of capillary interfacial area requires characterization of all phases present and thus, is more sensitive to the challenges associated with image processing. The

simultaneous multiple-phase segmentation (M2) method provides an integrated and consistent analysis of the phases, and anticipated to improve water-phase detection.

Using the advanced segmentation approach, the air-water interfacial area is presented as a result of direct measurement of contact areas between the two fluids. This is in contrast to previously reported data, which were derived indirectly from calculations based on individually measured phase surface areas and conceptualizations of fluid distributions. The effects of these assumptions on the capillary interfacial behavior are evaluated. Results from this study confirmed the initial hypothesis that the behavior of fluid surface areas will affect the theoretical shape of the capillary curve. The results support the understanding of the capillary interfacial area behavior in response to changes in the configuration of fluid surface areas during a drainage cycle. Furthermore, results for the measured air-water interface allows for further identification of fluid domains, such as the relationship between film interfacial area, capillary domains (menisci), and the total-measurable interfacial area. Experiments were also conducted using aqueous-phase interfacial partitioning tracer tests for comparison. Results support the hypothesis that different methods provide characterization of different interfacial domains. Overall, this study provides an imaging-based approach for evaluation of water configuration, and presents a measurement-based framework for further understanding of the role of fluid-fluid interfaces in natural porous media.

CHAPTER I

INTRODUCTION

I. 1. Background

The human environment is located at the Earth's surface and is heavily dependent on soil-water-atmospheric interactions. The geological material located between the land surface and the top of the underlying groundwater-saturated zone is known as the vadoze zone. It is typically comprised of unconsolidated sediment. Through the hydrologic cycle, all physical, chemical and biological processes in nature are interactive. Pollutants generally enter water supplies through surface soils and surface water bodies. The vadoze zone is considered the critical zone for pollutants, capable of buffering contaminants that would otherwise directly enter the groundwater. Near the surface, the vadoze zone includes the root zone (rhizosphere) in direct contact with surface water and the atmosphere. The transport of pollutants is influenced by properties of soil, contaminant chemistry, and fluid flow.

Fluid-fluid interfacial areas in porous media are of considerable interest due to the impact they have on a wide range of processes. The air-water interfacial area is recognized to influence multiphase flow (e.g. Dullien 1985; Bear 1988) and to control interfacial retention of chemical contaminants, pathogens and colloids in the soil (e.g. Brusseau and Rao, 1990). Moreover, it moderates various mass-transfer processes occurring in the porous media, such as evapotranspiration, volatilization, gas exchange occurring across two immiscible fluid phases.

There have been several publications highlighting the need for including the fluid-fluid interfacial areas in models to date, specifically to those which seek to characterize fluid flow and mechanisms occurring at the pore scale, (e.g. Skopp, 1985; Hassanizadeh and Gray, 1993; Gvirtzman and Roberts, 1991; Reeves and Celia, 1996; Celia et al., 1998; Kawanishi et al., 1998). These fluid-fluid interfacial areas are manifestations of pore-scale distribution of fluids in the porous medium. There are only two primary methods available to measure fluid-fluid interfacial areas for porous media systems: partitioning interfacial tracer tests and imaging methods involving microtomography.

1.1.1 Interfacial Partitioning Tracer Tests (IPTT)

Interfacial partitioning tracer tests provide indirect measurements of interfacial areas based on the retention behavior of tracers that accumulate at the interface. This category of measurements involves tests whereby a fluid containing a tracer that partition to the non-wetting/wetting fluid interface is injected into the porous medium. The retention behavior of the tracer is measured and used to determine the interfacial area present in the system. The interfacial areas estimated in this manner are considered to represent the effective total air-water interfacial area (A_{aw}). The total air-water interface includes the capillary and film-associated areas at target saturation. Measurements obtained with tracer-based methods may be influenced by accessibility of some interfaces to the tracers of choice, sorption by the solid phase, and impact of the tracer on fluid configuration (e.g. Kim et al., 1997, 1999; Kim et al., 2006; Brusseau et al., 1997; Anwar

et al., 2000; Schaefer et al., 2000; Costanza-Robinson and Brusseau 2003; Brusseau et al., 2007).

There are several ways by which to implement an interfacial partitioning tracer test. Karkare and Fort, 1996 proposed a method for experimentally determining the air-water interface in unsaturated porous media. Their method was based on establishing a critical surfactant concentration necessary to induce water movement. Soon after, Silverstein and Fort, 1997 performed similar experiments and developed a simple model to investigate behavior in air-water systems. Anwar et al. (2000) and Schaefer et al. (2000) reported on a mass balance method (MB) to measure interfacial areas in simple porous media using surfactant sorption properties at different interfaces in the system. The governing principle to the mass balance approach is to allow the column sufficient time for the interfacial tracer (surfactant) solution to achieve concentration equilibrium through recirculation (e.g. Anwar et al., 2000) or through diffusive mass transfer (e.g. Schaefer et al., 2000).

Among others, Kim et al. (1997; 1999; 2006), Brusseau et al. (2007), and El Ouni, 2013, reported on methodology using an aqueous interfacial tracer solution in miscible-displacement experiments to correlate retardation obtained from a breakthrough curve to interfacial areas. This technique can also be used with gas-phase interfacial tracers (e.g. Brusseau et al., 1997, 2006; Peng and Brusseau, 2005a, 2005b; Costanza-Robinson and Brusseau, 2002a, 2002b, 2006; Sung and Chen, 2011).

Henry and Smith (2002), Karkare et al., (1993); Karkare and Fort, (1994; 1996) reported on induced drainage caused by surface-active solutes. Costanza-Robinson et al.

(2012) conducted miscible-displacement surfactant tracer tests and concluded that changes in surface tension caused by the injection of surfactant induced drainage and thus complicated the determination of water contents. Similar conclusions were also observed by (Kibbey and Chen, 2012; Kibbey, 2013). Changes in interfacial tension are speculated to change configuration of fluid-fluid interfaces thereby affecting interfacial area measurements. However, Brusseau et al. (2007) conducted surfactant tracer tests using the miscible-displacement method and did not observe significant drainage effects. This was accomplished through the use of a vacuum system to produce uniform flow.

Brusseau and colleagues (Costanza-Robinson and Brusseau 2002; Brusseau et al., 2007) evaluated the various interfacial partitioning tracer test methods and proposed that different methods measure different domains. More recently, Kibbey and Chen (2012) similarly suggested that the vast majority of studies vary fundamentally in terms of types of tracers used and how various tracers interact with the interfaces. These factors complicate comparisons between each method, particularly at different water saturations. Sung et al. (2010) tested aliphatic alcohol as a potential gaseous interfacial tracer. They concluded that the gas-phase miscible displacement test yields results closest to the true interfacial area at low saturations, consistent with the prior results reported by Brusseau and colleagues (Brusseau et al., 1997, 2006, 2007; Costanza-Robinson and Brusseau 2002; Peng and Brusseau, 2005). Interfacial measurements using aqueous tracers are considered to underrepresent the interfacial area, due to limited accessibility of the surfactant solution to pore regions that are not contributing to advective flow. These regions may to some extent be accessed through diffusive processes. Conversely, when

this technique is used with gas-phase tracers, almost all available interfaces are accessible.

Interfacial partitioning tracer tests (IPTT) are useful for applications where knowledge of retention, mass transfer, and transformation processes are needed. Although much research has been conducted to measure the air-water interface, there is still no clear evidence that the methods yield consistent information. Continued investigation of these methods is warranted, as measurements of interfacial areas using interfacial tracers are used as commonly used for comparison in modeling efforts and for comparison to microtomography.

1.1.2 Microtomography

Imaging methods such as synchrotron X-ray tomography have made possible more accurate visualization of the three-dimensional structure of porous systems at micrometer-scale resolution. The processing of image data is a critical component of these techniques. Many studies highlight complex segmentation methods with the focus on petrology and mineral distribution in rocks (e.g. Nakashima and Kamiya, 2007; Ketcham et al. 2005a, 2005b; Altman et al., 2005a, 2005b; Macedo et al. 1999; Vaz et al. 2002, 2011; Gualda and Rivers 2006; Gualda et al. 2010; Baker et al. 2012), as well as other uses such as membrane imaging (e.g. Remigy et al. 2007) and bone analysis (Ketcham and Ryan 2004). Others, (e.g. Iassonov et al. 2009b; Iassonov and Tuller 2010; Schlüter et al. 2010; Kulkarni et al. 2012) have discussed the robustness of specific segmentation methods for phase separation or grey-scale threshold selection. Baveye et

al. (2010b) attempted to determine the variation among the outcomes of various image thresholding strategies for the same sample, including the testing of image enhancement filters. They concluded that there is considerable observer influence associated with thresholding due to methods used, and in some instances variations within the method itself. Several reviews have been published related to image analysis and thresholding methods commonly applied in porous media research (Pal and Pal 1993; Sheppard et al., 2004; Taud et al., 2005; Taina et al. 2008; Tarquis et al., 2008; Iassonov et al., 2009a; and Wildenschild and Sheppard 2013) for example.

Prior investigations of image processing have focused on characterizing solids and pore space. Ketcham and Carlson (2001) described the process of image acquisition and possible complications in data interpretation, such as artifacts that for example, can cause the edges around the grains to be blurred, or the appearance of rings within the image (Ketcham and Carlson 2001). These artifacts can complicate the quantification of a material and its boundaries, thus making threshold selection difficult. For example, Taud et al. (2005) and Peng et al. (2012) observed that rock porosities estimated from image analysis changed with small variations in threshold. As a result of threshold selection, the pore space can appear different than in the original greyscale, blur, or change their perceived connectivity once segmented (Taud et al. 2005). In general, images are rarely perfect representations of the attenuation coefficients, as they are influenced by optical transfer functions, scatter, and noise (Kaestner et al. 2008).

Another concern is the impact of heterogeneity of the sample (spatial variability of material properties) on imaging and analysis. This often manifests as non-uniform

sample illumination and differing attenuation coefficients, which leads to variation in grey scale for a single phase (e.g. Houston et al. 2013a, 2013b; Hapca et al. 2013). This in turn can complicate phase segmentation and separation of multiple phases. The degree of grey-scale variance is influenced by heterogeneity in grain sizes, distribution, surface roughness, and mineralogical composition. Partial volume effects, which occur when the target structural features such as pores have similar dimensions as the image resolution, are also a concern (Schlüter et al. 2010; Houston et al., 2013). In some instances, the intensity of grey-scale can also vary with the point of view of the sample. For example a very bright oxide particle can over illuminate certain regions, and lead to shadows or darker regions nearby.

Characterizing fluids and associated interfacial areas within porous media adds additional complexity to image analysis. For example, fluid-fluid interfacial area has two components: the area associated with capillary domains, and the area associated with non-wetting fluid in contact with wetting-phase films. When a porous medium desaturates, the wetting phase accumulates around the grains. As the disconnected wetting-phase films become thinner, they become more difficult to distinguish from the solid grains. This issue becomes more prominent when dealing with natural porous media. Kaestner et al. (2008) offered an overview of image processing procedures using a partially saturated porous medium, with the focus on enhancement filters. Their research particularly highlights the difficulties in delineating the water phase from the sand grains.

The segmentation step is considered to be the critical component of image processing. There are two general approaches for segmentation, global and local

thresholding. In general, a global threshold is determined by the midpoint greyscale value between the phase of interest, and background phase of least contrast (ASTM 1992; Ketcham and Iturrino 2005; Schnaar and Brusseau 2005, 2006a, 2006b; Baveye et al. 2010a; Peng et al. 2012) and this single threshold is used for the entire image domain. Global thresholding is widely used for segmentation of x-ray tomographic data (i.e. Oh and Lindquist 1999, Wang et al. 2011). The majority of research to date focused on characterizing air-water interfacial area has employed global thresholding approaches for segmentation. Brusseau and colleagues (Brusseau et al., 2006, 2007, 2008, 2009, 2010; Schnaar and Brusseau, 2005, 2006a; 2006b; Narter and Brusseau, 2010) used global thresholding, enhanced by the application of dual-energy imaging and image subtraction, for determining total non-wetting/wetting interfacial area, which requires characterization of only the non-wetting phase volume and surface area. For determining capillary interfacial area, the volumes and surface areas of all phases must be characterized. Schnaar and Brusseau (2006) and Costanza-Robinson et al. (2008) employed sequential single-phase (global-threshold-based) segmentation, after which the binarized data were combined and processed for phase quantification.

The global thresholding approach, given its use of a single value for the entire image, may produce misclassification errors when considering the complex spatial structure of porous media, and corresponding greyscale variations. Often, these variations are observed within a single sample volume. This is particularly of concern for characterizing systems containing multiple fluids. This approach can lead to bias and inconsistencies in image analysis (e.g. Schnaar and Brusseau, 2005, 2006a; Iassonov et

al., 2009b; Iassonov and Tuller, 2010). Thus, it is clear that more sophisticated means of phase identification are needed to address multi-phase systems.

Local thresholding approaches that consider the spatial information of neighboring voxels have been suggested as means to improve segmentation of complex structures (e.g. Pal and Bhandari 1993; Pal and Pal 1993; Baveye et al. 2010a; Hapca et al. 2013). There are a variety of locally adaptive based techniques presented in the literature. Motivated by the difficulties encountered in applying global thresholding methods to biphasic rock samples, Oh and Lindquist 1999 developed a local threshold method to improve segmentation. Wang et al. 2011 simulated soil images and applied several commonly used segmentation algorithms to address the lack of benchmark parameters available by which to judge segmentation methods. They concluded that there was no single segmentation method that preserved pore characteristics in all situations, although some methods yielded better results depending on quality of greyscale separation between phases. Houston et al. (2013a) further reported on improvements to the original Oh and Lindquist (1999) method. Kulkarni et al. 2012 developed a simultaneous multi-phase segmentation program incorporating a variety of local threshold selection methods. Hapca et al. 2013 presented a fully automated, operator-independent method for the segmentation of three-dimensional images.

The resolution available and image analysis software have both significantly improved in the last few years, thus, allowing for more detailed studies at the pore scale. As the theoretical models have also advanced, sizeable amounts of quantitative data have emerged. There is opportunity for direct measurements of fluid-fluid interfacial areas,

which offer the prospect of validating predictive theories (e.g. models) as well as further studies in natural porous media.

I.2. Research Objective

The purpose of the work presented here is to measure air-water interfacial areas at multiple wetting-phase saturations for natural porous media. Interfacial Partitioning tracer experiments were conducted with the goal to understand the features inherent to each method, and their efficacy in providing measurements of air-water interfacial area. X-ray microtomography was used to further characterize the relationship between film interfacial area, capillary domains (menisci), and the total-measurable interfacial area. For the first time, the air-water interfacial area is determined as a result of direct measurement of the actual contact surfaces between air and water. This is in contrast to previously reported data, which were derived indirectly from calculations based on measured phase surface areas and assumed conceptualizations of fluid distributions.

Microtomography is the first method to our knowledge that is able to distinguish between the total and the capillary-associated interfacial area. This is due to the ability to calculate the surface area of all phases present in the system from an image set directly. Most of the existing investigations of interfacial area in porous media (e.g. Saripalli et al., 1997; Chen and Doolen, 1998; Dalla et al. 2002; Culligan et al., 2004, 2006; Chen et al., 2004, 2007; Chen and Kibbey, 2006; Pyrak-Nolte et al., 2008; Porter and Wildenschild, 2009; Porter et al., 2009, 2010) have been focused on determination of the capillary interfaces, in part, because current models have their origins in examination of the

hysteresis phenomenon. Additionally prior studies have relied heavily on the use of glass beads or synthetic media.

CHAPTER II PRESENT STUDY

II. 1 Explanation of Dissertation Format

This dissertation comprises two chapters and six appendices. Chapter I is the introduction explaining the background for this research and the research objectives. Chapter II is a summary of the present study, and includes the most notable findings discussed in detail in Appendices A, B, C, D, and E. Additional information regarding additional experiments conducted to characterize the porous media is included in Appendix F.

Appendices A, B, D, are manuscripts and will be submitted to peer-reviewed journals. My advisor Dr. Brusseau provided advice and guidance in all of the work presented in the Appendices. For the manuscript presented in Appendix A, Dr. Tuller provided the image segmentation analysis software, and critical assistance in terms of identifying segmentation problems to establish the collaboration effort. Ramaprasad Kulkarni conducted the independent image analysis using this program (M2) in Appendix A. Dr. Marcel Schaap also provided experimental guidance for microtomography experiments, and much appreciated discussions regarding theoretical pore scale modeling efforts. The data presented in this work, the experimental data collection and analysis are my own and represent my original work.

II.2 Research Summary

The methods, materials, results and conclusions of this study are presented in the Appendices appended to this document. The following is a summary of the primary objectives and the most notable findings in the research presented herein.

II.2.1 Comparison of Image Segmentation For Determining Total And Capillary Air-Water Interfacial Areas In Natural Porous Media (Appendix A)

The primary objective of this study was to compare two image-processing procedures for characterizing fluids and associated interfaces in natural porous media. The two approaches included (a) a simpler method employing global thresholding and sequential single-phase segmentation (M1), and (b) a more complex method applying local threshold selection for simultaneous multiple-phase segmentation (M2). The volumes of air, water, and solid phases were used for quantitative comparison to independently measured porosities. The methods were used to process data sets comprised of multiple drainage steps for water-saturated packed columns imaged via synchrotron x-ray microtomography. The results of both methods were evaluated on how well they compared to independently measured porosity (n) and specific solid surface areas (SSA). These were used as benchmarks to evaluate robustness of segmentation methods. The results show that both methods are suitable for determination of total air-water interfacial area (A_{aw}), which requires characterization of only the non-wetting phase. Conversely, determination of capillary interfacial area (C_{aw}) requires characterization of all phases present, and was concluded to be more sensitive to threshold selection processes during image processing analysis. The simultaneous

multiple-phase segmentation method (M2) provides an integrated and consistent analysis of the phases, and is generally anticipated to provide more reliable determination of capillary interfacial area (C_{aw}).

The results from performance evaluation of 45-50 sand (Figures 1 and 7) and Vinton (Figures 3 and 9) media suggest both M1 and M2 results are sufficiently comparable. However, the glass bead sample comparison to independent parameters revealed noteworthy differences in the segmented solid surface areas using Method 2. These differences were attributed to pixilation effects caused by difficulties in boundary identification of water-solid interface. Pixilation was speculated to have contributed to the overestimation of all surface areas (i.e. air, water, and solid). This hypothesis was tested with 45-50 sand with noise-reduction filters applied to M2 segmentation (M2-filt.). This scenario led to significant improvement of the measured surface area of water and solid phases.

It was hypothesized that M2 would better detect the water phase at lower saturations, due to its local threshold selection in the segmentation stage of analysis. A main advantage of Method 2 is its ability to segment all desired phases simultaneously from a single grey-scale image, allowing for the discrimination of intermediate greyscales often overlooked by global thresholding methods (e.g. M1). The advantage of using this information is improved segmentation with less voxel misclassification (e.g. Wang et al. 2011, Houston et al. 2013a). The C_{aw} values obtained using Method 1 for the Glass Beads was more consistent based on the criteria established to determine reliability in this study. However, inspection of the surface area results suggests that M2 improved segmentation

of the water, especially at low saturations. Consequently, leading to the overall improvement of capillary interfacial area for the two natural porous media.

There is good potential for advances using M2 with the implementation of advanced locally adaptive automated algorithms, and possibly more advanced system characterization features such as fluid-fluid contact, fluid configuration, and connectivity of phases. All offer new horizons for future interfacial area research using high resolution imaging technology.

II.2.2 Sequential Image Segmentation Approach For Determining Total And Capillary Air-Water Interfacial Areas In Natural Porous Media (Appendix B)

The capillary interfacial area is calculated from the geometrical conceptualization of fluid configuration in the porous media (e.g. Montemagno and Ma, 1999; Dalla et al. 2002). Based on this model all phases in the system, (air, water, and solid) need to be identified. Using a single-phase analysis (SP) approach, where each phase is processed separately (e.g. Schnaar and Brusseau, 2005, 2006a, 2006b; Schnaar, 2006; Brusseau et al., 2008; Narter and Brusseau, 2010; Narter, 2012) there is potential for two (or three) phases to overlap after segmentation and phase-separation because the phases are processed individually. The objectivity of simplistic segmentation methods is commonly questioned in the search for advanced segmentation methods (e.g. Wang et al., 2011; Kulkarni et al. (2012). Due to the lack of independent parameters in which to benchmark segmentation results, it was crucial to establish a methodology to ground the results to independently measured parameters. In this study, sequential single-phase segmentation

of synchrotron-based microtomography is evaluated, and a combined phase approach is introduced. The primary goal is to improve water-phase detection and capillary interfacial area (C_{aw}). The volumes and surface areas were extracted directly from segmentation for calculation of interfacial areas. Porosity was also used in this study as a measure to evaluate the representativeness of the method for the air-water systems investigated.

The total interfacial area (A_{aw}) results based on the integrated combined sequential approach (Method 1) were not affected by small changes in threshold, cropping regions, or the combination of pre-segmented individual phases. This was attributed to the clear resolution of the air phase in X-ray tomography images. This information is used also for comparison using different segmentation approaches, such as for comparison study presented in Appendix A.

The suitability of each segmentation method for estimating C_{aw} is contingent upon scrutiny of the total A_{aw} , the specific solid surface area (SSA), porosity, and segmented volumes. The A_{max} is associated with the assumption of an infinitesimally thin layer of water solvating the solid surface. Thus, allowing for comparison to GSSA values, and is expected to be comparable to specific solid surface areas. Combining the air and solid phases provides more robust data compared to other combinations due to the independent metrics used to ground truth results from solid phase analysis. For example, the porosities obtained from analysis of the solid phase (both separately and as combined data) are similar to the independently determined gravimetric porosities. Also, the specific solid surface areas are comparable to the calculated theoretical GSSA values. Similar to the air phase analysis, segmentation of the solid phase is not as sensitive to threshold variations.

Unfortunately, there is no direct independent parameter to ground truth results for the water phase, and thus to quantify the capillary interfacial area C_{aw} . The integration of two robust individually segmented phases (air and solid) in this approach was shown to minimize phase overlap and provides more consistent determination of the wetting phase (water). Overall, this approach may help highlight possible spatial variability of water phase at the pore scale.

II.1.3 The Effects of Surface Areas on Capillary Interfacial Area Behavior (Appendix C)

Due to the extensive evaluation of surface areas required for threshold method comparison (Appendix C), a simple spreadsheet was developed to evaluate the effects of surface area compartment on the behavior of the calculated capillary interfacial area (C_{aw}) function. The specific total air-water interfacial area (A_{aw}) is measured based on the assumption that all solid surfaces are solvated by water, such that air-surfaces are always in contact with water phase. Consequently, the air surface area can be used as a proxy for total interfacial area. The C_{aw} was calculated as one half of the difference between the combined sum of the water phase (a_w) and air phase (a_a) surface areas and the solid phase (a_s) surface area (e.g., Montemagno and Ma, 1999; Dalla et al., 2002) respectively per equation 1.

$$C_{nw} = \frac{1}{2}(a_a + a_w - a_s) \quad (1)$$

The capillary interfacial area calculated from equation (1) refers to interfaces associated with the menisci of contacts between air and “bulk” water (partially filled capillaries, pendular rings, and wedges). This equation is developed from a simple phase-balance analysis of surface areas and interfacial contacts in a three-phase (solid, wetting fluid, non-wetting fluid) porous medium, and includes the assumption that wetting films are not present on solid surfaces. Several assumptions are used in this study, and are necessary to adapt to microtomography conditions. For example, at full water saturation, the air phase is not present ($a_a = 0$ at $S_w = 1$), and the water surface area should be similar to the solid surface area ($a_w = a_s$). Based on experimental data (Appendix A) the water surface area is smaller than the solid surface area, presumably due to grain-grain contacts. Likewise, the air surface area should approximate the solid surface area at $S_w = 0$ ($a_a = a_s$ and $a_w = 0$). These assumptions are essential in understanding interfacial domains measured using microtomography.

Results from this study confirmed the initial hypothesis that the behavior of fluid surface areas will affect the theoretical shape of the capillary curve. The results support the understanding of the capillary interfacial area behavior in response to changes in the configuration of fluid surface areas during a drainage cycle.

II.4 Determination of Film, Capillary, and Total Air-Water Interfacial Area Using X-Ray Microtomography (Appendix D)

The air-water interface in variably saturated porous media is recognized to influence interfacial retention of organic and inorganic contaminants, and mediate various mass-transfer processes. The formation and presence of water films commonly

solvating the surfaces of soil/sediment grains in unsaturated systems, as well as their impact on flow and retention processes have been of sustained interest. X-ray microtomography was used to measure air-water interfacial area at multiple wetting-phase saturations for natural sand. Specifically, the relationship between film interfacial area, capillary domains (menisci), and the total-measurable interfacial area was investigated. For the first time, air-water interfacial area is determined as a result of direct measurement of the actual contact surfaces between air and water. This is in contrast to previously reported data, which were derived indirectly from calculations based on measured phase surface areas and conceptualizations of fluid configurations. This study provides an imaging-based approach at evaluation of air-water interfaces, and presents a measurement-based framework for further understanding of their role in natural complex media.

II.5 Comparison Of Tracer-Based Methods For Measuring Air-Water Interfacial Area In Porous Media (Appendix E)

In this study the focus was placed on aqueous-phase interfacial tracer tests. The air-water interfacial area is measured as a function of water saturation for a natural porous medium using (a) modified aqueous-phase interfacial partitioning tracer tests (IPTT), and (b) surfactant mass balance method (MB). The objective is to understand the features inherent in each method, and its impact on overall measurements of air-water interfacial area in the system. Results are compared to interfacial partitioning tracer test measurements from the literature. Gas-phase tracer tests are presented here for reference, because it is the closest measurement to the true total surface area in a system.

The dependence of A_{aw} on S_w complicates the comparison between approaches in terms of absolute values. Thus, all results are plotted together in Figure 9 (Appendix E) with a regression derived from the gas-IPTT results. The different aqueous-test data sets are similar to the gas-IPTT data at high S_w . It is clearly observed that values from the GPTT experiments are much higher than the aqueous-phase measurements presented herein for lower saturations. This is expected as the aqueous-phase based experiments are limited by the areas of surfactant solution accessible to the interface (e.g. Anwar et al., 2000; Schaefer et al., 2000; Brusseau et al., 2007, 2010). Conversely, gas-phase tracer test results are the closest measurement to the true solid surface area, which includes surface roughness (e.g. Costanza-Robinson and Brusseau, 2002b; Peng and Brusseau, 2005a; 2005b; Brusseau et al., 2006, 2007; Sung and Chen, 2011).

Primarily, aqueous phase tracers have limited access to interfaces, whereas gas-phase tracers have almost unlimited access to air-water interfaces. The latter includes domains associated with bulk fluid contributing to advective flow and residual water (e.g. Costanza-Robinson and Brusseau, 2002b). These regions may to some extent be accessed through diffusive processes. Films are present coating the water-wet geomechanics, unless it is oven dried. Similarly, comparison between residual tracer tests in Figure 9 (Appendix E) suggests that each aqueous-phase approach results in A_{aw} information perhaps more relevant at different saturation of interest.

The modified residual-IPTT approach is experimentally simple, using saturated flow conditions. This allows for faster experiments and direct analysis during the experiment. The saturated flow conditions limit the practical water saturation (S_w) range

to approximately 0.70-1.0. The standard IPTT test conducted under unsaturated flow conditions is more challenging and requires longer test times due to the imposed boundary conditions. Using this approach, the water content can be reduced further, to an operational range between 1 and approximately 0.50 S_w . The limitations of both aqueous-phase miscible-displacement methods are that only one interfacial area value can be obtained per experiment. The mass balance method (MB) was designed to circumvent these limitations by enabling A_{aw} interfacial values to be measured for multiple water saturations with a single experiment. The disadvantage is that one may still need several experiments to obtain A_{aw} values for a full drainage curve, from saturation to drier conditions due to the variability in S_w range. It is worthy of mention that the procedure is significantly more time consuming (2-3 weeks) when applied to highly heterogeneous soils, such as Vinton, than in simple media (e.g. 45-50). In comparison, approximately 5-10 days is required to complete an experiment using the residual IPTT approach. The duration of the experiments is primarily dictated by equilibrium, and drainage procedures, and is highly influenced by user expertise.

Overall, results presented in this study are within the expected values based on simulated gas-phase tracer test results. Significant differences in interfacial measurements were not observed for the different methods of aqueous-phase tracer tests. This indicates that the various methods can provide reasonably similar measures of air-water interfacial area within the restrictions of each method.

II. 6 Conclusions and Future Directions

The primary goal for this research was to measure the air-water interface in several porous media. In the present study X-ray microtomography was used for direct measurements of air-water interfaces, in a variety of porous media. Experiments were also conducted using aqueous-phase interfacial partitioning tracer tests for comparison. Gas-phase IPTT results from our group were used for comparison between the true total interfacial area and microtomography results. These results confirm the hypothesis that different methods are restricted to specific interfaces for characterization (e.g. Appendix E).

Much research has been conducted to measure the air-water interface, and still there has not been a consensus of evidence for which of several approaches used to infer air-water interfacial area (A_{aw}) will yield consistent information. The aqueous tracers are restricted to areas contributing to bulk fluid flow, and thus only a fraction of the total interface can be measured. Varying experimental techniques can further restrict areas available for characterization. For example, microtomography methods (Appendix A, B) cannot resolve water films, or areas associated with surface roughness. Similarly, aqueous-based tracer method results suggest that interfacial areas have access to interfaces near the path of fluid flow (i.e. residual air) that are accessed via diffusion. These experiments are also sensitive to tracer concentration and sorption. Sorption is especially important in measurements using natural soils and sediments.

For the first time, results of direct measurement of air-water interfacial contact areas are presented. Microtomography is the primary method for direct measurements at

the pore scale. However, due to the necessary assumptions and lack of image segmentation methods, this opportunity was not available until recently. As a consequence of using microtomography methods, portions of this work required heavy image analysis efforts, and deep knowledge of segmentation processes required to quantitatively extract parameters of interest. It was with this objective that the study was developed in Appendix A and B. The integrated approach (Method 1) was shown to yield reliable results, based on benchmarks and comparison to independently measured parameters. However, in an effort to address long standing criticism regarding the objectivity of the segmentation algorithms used in previous studies (e.g. Schnaar 2006, Brusseau et al., 2007, 2008; Narter, 2012) the comparative study (Appendix A) was conducted. Results showed that the advanced segmentation method met expectations by improving segmentation of water, and allowing for direct air-water contact area measurement. The measured contact interfacial areas included additional air-water interface that is not included in the standard approach for calculating capillary interfacial areas. This result was instrumental in the characterization and discernment of the different domains measured directly using microtomography. Overall, the work presented in this dissertation contributed to the ability to quantify total, capillary, and film interfacial domains. These parameters can be used in predictive models of flow and transport in the porous media.

REFERENCES

- Anwar, A., M. Bettahar, and U. Matsubayashi (2000), A method for determining air-water interfacial area in variably saturated porous media, *Journal of Contaminant Hydrology*, 43(2), 129-146.
- Brusseau, M. L., and P. S. C. Rao (1990), Modeling Solute Transport in Structured Soils - a Review, *Geoderma*, 46(1-3), 169-192.
- Brusseau, M. L., J. Popovicova, and J. A. K. Silva (1997), Characterizing gas-water interfacial and bulk water partitioning for gas phase transport of organic contaminants in unsaturated porous media, *Environmental Science & Technology*, 31(6), 1645-1649.
- Brusseau, M. L., M. Narter, and H. Janousek (2010), Interfacial Partitioning Tracer Test Measurements of Organic-Liquid/Water Interfacial Areas: Application to Soils and the Influence of Surface Roughness, *Environmental Science & Technology*, 44(19), 7596-7600.
- Brusseau, M. L., S. Peng, G. Schnaar, and M. S. Costanza-Robinson (2006), Relationships among air-water interfacial area, capillary pressure, and water saturation for a sandy porous medium, *Water Resources Research*, 42(3).
- Brusseau, M. L., S. Peng, G. Schnaar, and A. Murao (2007), Measuring air-water interfacial areas with X-ray microtomography and interfacial partitioning tracer tests, *Environmental Science & Technology*, 41(6), 1956-1961.
- Brusseau, M. L., H. Janousek, A. Murao, and G. Schnaar (2008), Synchrotron X-ray microtomography and interfacial partitioning tracer test measurements of NAPL-water interfacial areas, *Water Resources Research*, 44(1).
- Celia, M. A., W. G. Gray, C. D. Montemagno, and P. C. Reeves (1998), On the inclusion of interfacial area in models of two-phase flow in porous media, in *Iahs-Aish P*, edited by M. Herbert and K. Kovar, pp. 81-87.
- Chen, D. Q., L. J. Pyrak-Nolte, J. Griffin, and N. J. Giordano (2007), Measurement of interfacial area per volume for drainage and imbibition, *Water Resources Research*, 43(12).
- Chen, L., and T. C. G. Kibbey (2006), Measurement of air-water interfacial area for multiple hysteretic drainage curves in an unsaturated fine sand, *Langmuir*, 22(16), 6874-6880.
- Chen, S., and G. D. Doolen (1998), Lattice Boltzmann method for fluid flows, *Annual Review of Fluid Mechanics*, 30, 329-364.

- Cheng, J. T., L. J. Pyrak-Nolte, D. D. Nolte, and N. J. Giordano (2004), Linking pressure and saturation through interfacial areas in porous media, *Geophysical Research Letters*, 31(8).
- Costanza-Robinson, M. S., and M. L. Brusseau (2002a), Gas phase advection and dispersion in unsaturated porous media, *Water Resources Research*, 38(4).
- Costanza-Robinson, M. S., and M. L. Brusseau (2002b), Air-water interfacial areas in unsaturated soils: Evaluation of interfacial domains, *Water Resources Research*, 38(10).
- Costanza-Robinson, M. S., and M. L. Brusseau (2006), Gas-Phase Dispersion in Porous Media, *Theor Appl Trans Por*, 20, 121-132.
- Culligan, K. A., D. Wildenschild, B. S. B. Christensen, W. G. Gray, and M. L. Rivers (2006), Pore-scale characteristics of multiphase flow in porous media: A comparison of air-water and oil-water experiments, *Advances in Water Resources*, 29(2), 227-238.
- Culligan, K. A., D. Wildenschild, B. S. B. Christensen, W. G. Gray, M. L. Rivers, and A. F. B. Tompson (2004), Interfacial area measurements for unsaturated flow through a porous medium, *Water Resources Research*, 40(12), n/a-n/a.
- Dalla, E., M. Hilpert, and C. T. Miller (2002), Computation of the interfacial area for two-fluid porous medium systems, *Journal of Contaminant Hydrology*, 56(1-2), 25-48.
- El Ouni, A. (2013), Measuring Air-Water Interfacial Area in Unsaturated Porous Media Using the Interfacial Partitioning Tracer Test Method, edited, p. 62 leaves, University of Arizona, University of Arizona.
- Gvirtsman, H., and P. V. Roberts (1991), Pore Scale Spatial-Analysis of 2 Immiscible Fluids in Porous-Media, *Water Resources Research*, 27(6), 1165-1176.
- Haines, W. B. (1930), Studies in the physical properties of soil V The hysteresis effect in capillary properties, and the modes of moisture distribution associated therewith, *Journal of Agricultural Science*, 20, 97-116.
- Hassanizadeh, S. M., and W. G. Gray (1993), Toward An Improved Description Of The Physics Of 2-Phase Flow, *Advances in Water Resources*, 16(1), 53-67.
- Karkare, M. V., and T. Fort (1994), Flow In Unsaturated Porous-Media Due To Water-Insoluble Surfactants - Role Of Momentum-Transfer From A Spreading Monolayer, *Langmuir*, 10(10), 3701-3704.
- Karkare, M. V., and T. Fort (1996), Determination of the air-water interfacial area in wet "unsaturated" porous media, *Langmuir*, 12(8), 2041-2044.

Karkare, M. V., H. T. La, and T. Fort (1993), Criteria For Effectiveness Of Surfactants As Water-Moving Agents In Unsaturated Wet Sand, *Langmuir*, 9(7), 1684-1690.

Kawanishi, T., Y. Hayashi, P. V. Roberts, and M. J. Blunt (1998), Fluid-fluid interfacial area during two and three phase fluid displacement in porous media: a network model study, *Iahs-Aish P*(250), 89-96.

Kibbey, T. C. G. (2013), The configuration of water on rough natural surfaces: Implications for understanding air-water interfacial area, film thickness, and imaging resolution, *Water Resources Research*, 49(8), 4765-4774.

Kibbey, T. C. G., and L. X. Chen (2012), A pore network model study of the fluid-fluid interfacial areas measured by dynamic-interface tracer depletion and miscible displacement water phase advective tracer methods, *Water Resources Research*, 48.

Kim, H., P. S. C. Rao, and M. D. Annable (1997), Determination of effective air-water interfacial area in partially saturated porous media using surfactant adsorption, *Water Resources Research*, 33(12), 2705-2711.

Kim, H., P. S. C. Rao, and M. D. Annable (1999), Gaseous tracer technique for estimating air-water interfacial areas and interface mobility, *Soil Science Society of America Journal*, 63(6), 1554-1560.

Kim, H., K. M. Choi, J. W. Moon, and M. D. Annable (2006), Changes in air saturation and air-water interfacial area during surfactant-enhanced air sparging in saturated sand, *Journal of Contaminant Hydrology*, 88(1-2), 23-35.

Montemagno, C. D., and Y. Ma (1999), Measurement fo Interfacial Surface Area for Two-Phase Flow in Porous Media from PVI Data, in *Characterization and measurement of the hydraulic properties of unsaturated porous media: proceedings of the International Workshop on Characterization and Measurement of the Hydraulic Properties of Unsaturated Porous Media: Riverside, California, October 22-24, 1997*, edited by M. T. van Genuchten, F. J. Leij and L. Wu, pp. 121-132, U.S. Salinity Laboratory, Agricultural Research Service Dept. of Environmental Sciences, University of California, Riverside, CA.

Narter, M. (2012), Characterizing Non-Wetting Fluid in Natural Porous Media Using Synchrotron X-Ray Microtomography, edited, p. 172 leaves, University of Arizona, University of Arizona.

Narter, M., and M. L. Brusseau (2010), Comparison of interfacial partitioning tracer test and high-resolution microtomography measurements of fluid-fluid interfacial areas for an ideal porous medium, *Water Resources Research*, 46.

Peng, S., and M. L. Brusseau (2005a), Gas-phase partitioning tracer test method for water content measurement: Evaluating efficacy for a range of porous-medium textures, *Vadose Zone Journal*, 4(3), 881-884.

Peng, S., and M. L. Brusseau (2005b), Impact of soil texture on air-water interfacial areas in unsaturated sandy porous media, *Water Resources Research*, 41(3).

Porter, M. L., and D. Wildenschild (2009), Image analysis algorithms for estimating porous media multiphase flow variables from computed microtomography data: a validation study, *Computational Geosciences*, 14(1), 15-30.

Porter, M. L., M. G. Schaap, and D. Wildenschild (2009), Lattice-Boltzmann simulations of the capillary pressure-saturation-interfacial area relationship for porous media, *Advances in Water Resources*, 32(11), 1632-1640.

Porter, M. L., D. Wildenschild, G. Grant, and J. I. Gerhard (2010), Measurement and prediction of the relationship between capillary pressure, saturation, and interfacial area in a NAPL-water-glass bead system, *Water Resources Research*, 46(8).

Pyrak-Nolte, L. J., D. D. Nolte, D. Chen, and N. J. Giordano (2008), Relating capillary pressure to interfacial areas, *Water Resources Research*, 44(6).

Reeves, P. C., and M. A. Celia (1996), A Functional Relationship Between Capillary Pressure, Saturation, and Interfacial Area as Revealed by a Pore-Scale Network Model, *Water Resources Research*, 32(8), 2345-2358.

Saripalli, K. P., H. Kim, P. S. C. Rao, and M. D. Annable (1997), Measurement of specific fluid - Fluid interfacial areas of immiscible fluids in porous media, *Environmental Science & Technology*, 31(3), 932-936.

Schaefer, C. E., D. A. DiCarlo, and M. J. Blunt (2000), Determination of Water-Oil Interfacial Area during 3-Phase Gravity Drainage in Porous Media, *J Colloid Interface Sci*, 221(2), 308-312.

Schnaar, G. (2006), Pore-Scale Characterization of Organic Immiscible Liquid in Natural Porous Media Using Synchrotron X-ray Microtomography, edited, p. 208 leaves, University of Arizona, Tucson, Arizona.

Schnaar, G., and M. L. Brusseau (2005), Pore-scale characterization of organic immiscible-liquid morphology in natural porous media using synchrotron X-ray microtomography, *Environmental Science & Technology*, 39(21), 8403-8410.

Schnaar, G., and M. L. Brusseau (2006a), Characterizing pore-scale dissolution of organic immiscible liquid in natural porous media using synchrotron X-ray microtomography, *Environmental Science & Technology*, 40(21), 6622-6629.

Schnaar, G., and M. L. Brusseau (2006b), Characterizing pore-scale configuration of organic immiscible liquid in multiphase systems with synchrotron X-ray microtomography, *Vadose Zone Journal*, 5(2), 641-648.

Silverstein, D. L., and T. Fort (1997), Studies in air-water interfacial area for wet unsaturated particulate porous media systems, *Langmuir*, 13(17), 4758-4761.

Skop, J. (1985), Oxygen Uptake and Transport in Soils: Analysis of the Air-water Interfacial Area, *Soil Science Society of America Journal*, 49(6), 1327-1331.

Sung, M., and B. H. Chen (2011), Using aliphatic alcohols as gaseous tracers in determination of water contents and air-water interfacial areas in unsaturated sands, *J Contam Hydrol*, 126(3-4), 226-234.

Wildenschild, D., and A. P. Sheppard (2013), X-ray imaging and analysis techniques for quantifying pore-scale structure and processes in subsurface porous medium systems, *Advances in Water Resources*, 51, 217-246.

Wildenschild, D., J. W. Hopmans, M. L. Rivers, and A. J. R. Kent (2005), Quantitative analysis of flow processes in a sand using synchrotron-based X-ray microtomography, *Vadose Zone Journal*, 4(1), 112-126.

Wildenschild, D., J. W. Hopmans, C. M. P. Vaz, M. L. Rivers, D. Rikard, and B. S. B. Christensen (2002), Using X-ray computed tomography in hydrology: systems, resolutions, and limitations, *Journal of Hydrology*, 267(3-4), 285-297.

APPENDIX A

IMAGE SEGMENTATION FOR DETERMINING TOTAL AND CAPILLARY

AIR-WATER INTERFACIAL AREAS IN NATURAL POROUS MEDIA

Juliana B. Araújo¹, Ramaprasad Kulkarni³, Markus Tuller¹, and Mark L. Brusseau^{1, 2*}

¹Soil, Water, and Environmental Science Department

²Hydrology and Water Resources Department

School of Earth and Environmental Sciences

³Electrical and Computer Engineering Department

The University of Arizona

Shantz Bldg.

Tucson, AZ 85721

Submitted to:

Journal Name in bold

Date

June 20, 2014

*Corresponding author: Brusseau@email.arizona.edu

1. ABSTRACT

This study was conducted to investigate image-processing procedures suitable for characterizing fluids and associated interfaces in natural porous media. We compare two approaches for image analysis: (a) a simpler method employing global thresholding and sequential single-phase segmentation (M1), and (b) a more complex, local-thresholding method based on grey-scale clustering for phase identification and simultaneous multiple-phase segmentation using a statistical algorithm (M2). The methods were used to process data sets comprised of multiple drainage steps for water-saturated packed columns imaged via synchrotron x-ray microtomography. The results of both methods were evaluated on how well they compared to independently measured porosity and specific solid surface areas. The results show that both methods are suitable for determination of total air-water interfacial area, which requires characterization of only the non-wetting phase. Conversely, determination of capillary interfacial area requires characterization of all phases present and thus, is more sensitive to the challenges associated with image processing. The simultaneous multiple-phase segmentation (M2) method provides an integrated and consistent analysis of the phases, and thus is generally anticipated to provide more reliable determination of capillary interfacial area. The need for application of pre-segmentation filters was investigated for Method 2, and it was observed that their use significantly improved output.

Keywords: X-ray Microtomography, air-water interfacial area, capillary, segmentation, image analysis, local and global threshold

2. INTRODUCTION

Imaging methods such as synchrotron X-ray tomography have made possible more accurate visualization of the three-dimensional structure of porous systems at micrometer-scale resolution. The processing of image data is a critical component of these techniques. Many studies highlight complex segmentation methods with the focus on petrology and mineral distribution in rocks (e.g. Nakashima and Kamiya, 2007; Ketcham et al. 2005a, 2005b; Altman et al., 2005a; Altman et al., 2005b, Macedo et al. 1999; Vaz et al. 2002; Vaz et al. 2011; Gualda and Rivers 2006; Gualda et al. 2010; Baker et al. 2012), as well as other uses such as membrane imaging (e.g. Remigy et al. 2007) and bone analysis (Ketcham and Ryan 2004). Others, (e.g. Iassonov et al. 2009b; Iassonov and Tuller 2010; Kulkarni et al. 2012; Schlüter et al. 2010) have discussed the robustness of specific segmentation methods for phase separation or grey-scale threshold selection. Baveye et al. (2010b) attempted to determine the variation among the outcomes of various image thresholding strategies for the same sample, including the testing of image enhancement filters. They concluded that there is considerable observer influence associated with thresholding due to methods used, and in some instances variations within the method itself. Several reviews have been published related to image analysis and thresholding methods commonly applied in porous media research (Taina et al. 2008; Tarquis et al., 2008; Pal and Pal 1993; Taud et al., 2005; Iassonov et al., 2009a; Sheppard et al., 2004; and Wildenschild and Sheppard 2013 for example).

Prior investigations of image processing methods have focused primarily on characterizing solids and pore space. Ketcham and Carlson (2001) described the process

of image acquisition and possible complications in data interpretation, such as artifacts that for example, can cause the edges around the grains to be blurred, or the appearance of rings within the image (Ketcham and Carlson 2001). These artifacts can complicate the quantification of a material and its boundaries, thus making threshold selection difficult. For example, Taud et al. (2005) and Peng et al. (2012) observed that rock porosities estimated from image analysis changed with small variations in threshold. As a result of threshold selection, the pore space can appear different than in the original greyscale, blur, or change their perceived connectivity once segmented (Taud et al. 2005). In general, images are rarely perfect representations of the attenuation coefficients, as they are influenced by optical transfer functions, scatter, and noise (Kaestner et al. 2008).

Another concern is the impact of heterogeneity of the sample (spatial variability of material properties) on imaging and analysis. This often manifests as non-uniform sample illumination and differing attenuation coefficients, which leads to variation in grey scale for a single phase (Houston et al. 2013a; Houston et al. 2013b; Hapca et al. 2013). This in turn can complicate phase segmentation and separation of multiple phases. The degree of grey-scale variance is influenced by heterogeneity in grain sizes, distribution, surface roughness, and mineralogical composition. Partial volume effects, which occur when the target structural features such as pores have similar dimensions as the image resolution, are also a concern (Schlüter et al. 2010; Houston et al., 2013; Brown et al., 2014). In some instances, the intensity of grey-scale can also vary with the point of view of the sample. For example a very bright oxide particle can over illuminate certain regions, and lead to shadows or darker regions nearby.

Characterizing fluids and associated interfacial areas within porous media adds additional complexity to image analysis. For example, fluid-fluid interfacial area has two components: the area associated with capillary domains, and the area associated with non-wetting fluid in contact with wetting-phase films. When a porous medium desaturates, the wetting phase accumulates around the grains. As the disconnected wetting-phase films become thinner, they become more difficult to distinguish from the solid grains. This issue becomes more prominent when dealing with natural porous media. Kaestner et al. (2008) offered an overview of image processing procedures using a partially saturated porous medium, with the focus on enhancement filters. Their research particularly highlights the difficulties in delineating the water phase from the sand grains.

The segmentation step is generally considered the critical component of image processing. There are two general approaches for segmentation, global and local thresholding. In general, a global threshold is determined by the midpoint greyscale value between the phase of interest, and background phase of least contrast (ASTM 1992; Ketcham and Iturrino 2005; Baveye et al. 2010a; Peng et al. 2012; Schnaar and Brusseau 2005, 2006a, 2006b), and this single threshold is used for the entire image domain. Global thresholding is widely used for segmentation of x-ray tomographic data (i.e. Oh and Lindquist 1999, Wang et al. 2011). The majority of research to date focused on characterizing air-water interfacial area has employed global thresholding approaches for segmentation. Brusseau and colleagues (Schnaar and Brusseau, 2005; Brusseau et al., 2006; Schnaar and Brusseau, 2006b; 2006a; Brusseau et al., 2007; Brusseau et al., 2008; Brusseau et al., 2009; Brusseau et al., 2010; Narter and Brusseau, 2010) used global

thresholding, enhanced by the application of dual-energy imaging and image subtraction, for determining total non-wetting/wetting interfacial area, which requires characterization of only the non-wetting phase volume and surface area. For determining capillary interfacial area, the volumes and surface areas of all phases must be characterized. Schnaar and Brusseau (2006) and Costanza-Robinson et al. (2008) employed sequential single-phase (global-threshold-based) segmentation, after which the binarized data were combined and processed for phase quantification.

The global thresholding approach, given its use of a single value for the entire image, may produce misclassification errors when considering the complex spatial structure of porous media, and corresponding greyscale variations. Often, these variations are observed within a single sample volume. This is particularly of concern for characterizing systems containing multiple fluids. Hence, this approach can lead to bias and inconsistencies in image analysis (e.g. Schnaar and Brusseau, 2005; 2006a; Iassonov et al., 2009b; Iassonov and Tuller, 2010). Thus, it is clear that more sophisticated means of phase identification are needed to address multi-phase systems.

Local thresholding approaches that consider the spatial information of neighboring voxels have been suggested as means to improve segmentation of complex structures (e.g. Pal and Bhandari 1993; Pal and Pal 1993; Baveye et al. 2010a; Hapca et al. 2013). There are a variety of locally adaptive based techniques presented in the literature. Motivated by the difficulties encountered in applying global thresholding methods to biphasic rock samples, Oh and Lindquist 1999 developed a local threshold method to improve segmentation. Wang et al. 2011 simulated soil images and applied

several commonly used segmentation algorithms to address the lack of benchmark parameters available by which to judge segmentation methods. They concluded that there was no single segmentation method that preserved pore characteristics in all situations, although some methods yielded better results depending on quality of greyscale separation between phases. Houston et al. (2013a) further reported on improvements to the original Oh and Lindquist (1999) method. Kulkarni et al. 2012 developed a simultaneous multi-phase segmentation program incorporating a variety of local threshold selection methods. Hapca et al. 2013 presented a fully automated, operator-independent method for the segmentation of three-dimensional images.

This study was conducted to investigate image-processing procedures suitable for characterizing fluids and associated interfaces in natural porous media, which are inherently more complex, heterogeneous systems than the model media often used in prior studies. The goal is to minimize user bias, while optimizing the results in terms of quality and time. We compare two approaches for image analysis: (a) a simpler method employing global thresholding and sequential single-phase segmentation (M1), and (b) a more complex, local-thresholding method based on grey-scale clustering for phase identification and simultaneous multiple-phase segmentation using a statistical algorithm (M2). The utility of filtering is examined for the second method. Data collected from synchrotron-based x-ray microtomographic analysis for three porous media are used for this investigation.

3. MATERIALS AND METHODS

3.1 Materials

Three porous media were used, ranging in grain size and complexity: 1-mm borosilicate glass beads (Sigma-Aldrich), a well-sorted 45-50 mesh quartz sand (Accusand, Unimin Co.), and Vinton soil (Roger Road Farm, Lysimeter, Tucson, AZ). The relevant physical properties of the porous media are shown in Table 1. The saturating solution contained 12% potassium iodine (KI) (Fisher Scientific) to enhance contrast between the phases in the system.

3.2 Experiment Set-Up

Thin-walled acrylic columns, $L = 3$ cm, $d_{in} = 0.5$ cm, or aluminum columns, $L = 3.22$ cm, $d_{in} = 0.63$ cm, were packed with the desired porous media, with reasonably uniform bulk densities under slurry conditions. A (5-15 μm) hydrophilic capillary membrane was placed on the bottom of the column. A mesh was used at the top of the soil pack to prevent the soil from escaping, although in some cases a porous polypropylene frit was added to hold the membrane in place while packing. The saturated column was sealed and stored for imaging.

The columns were imaged prior to drainage. Drainage was induced by removing small increments of water from the column at a low flow rate, 0.050 ml/min, and allowing the fluid to equilibrate for at least 15 minutes prior to imaging. An electronic programmable syringe pump (KD Scientific) with a 2.5 mL gas-tight syringe was connected to a pressure transducer and to the bottom of the column. The top was open to

the atmosphere. After the final drainage step, the column was sealed for transport back to the lab, where contents of the column were used to measure the final water content. In some instances, this also served as a second measurement of bulk density. The data presented in this study reflect a single drainage sequence per porous medium.

3.3 Image Acquisition

X-ray microtomography images were collected at the GeoSoilEnviroCARS (GSECARS) BM-13D beamline at the Advanced Photon Source, Argonne National Laboratory, IL. The effective resolution for our experiments is $\sim 10 \mu\text{m}$. The field of view encapsulating the porous media is approximately 5 mm. The images were collected from the centers of the columns, to minimize the potential influence of end effects. Analysis of the data sets indicated that representative elementary volume (REV) requirements were met for the imaged volumes employed (Brusseau et al. 2006; Narter 2012; Culligan et al. 2004; Costanza-Robinson et al. 2008; Costanza-Robinson et al. 2011).

Sequential images of the columns were collected above and below the iodine edge, at 33.269 KeV and 33.069 KeV. The above-edge image (A-image) is used to enhance the liquid phase, and below-the-edge image (B-image) is used to distinguish the solid phase (e.g. Wildenschild et al. 2002; Schnaar and Brusseau, 2006a; Costanza-Robinson et al. 2008). The images were pre-processed using GSECARS-developed software (Rivers et al. 2010; Rivers 2012). The program is a set of IDL© (ITT, Visual Information Solutions) routines that were designed to view the CCD camera data, remove artifacts, correct for dark currents, and white field correction. Furthermore, it builds a

sinogram, aligns the rotation axis, removes ring artifacts, and filters noise. Finally, the program writes the reconstructed data as a single three-dimensional volume file, which can be exported into a series of individual slices or imported into a 3D viewer such as ImageJ (Rasband, 1997-2012). Further details regarding the facility are available at the GSECars webpage, (<http://cars9.uchicago.edu/software/idl/tomography.html>).

3.4 Image Processing

All of the images used for comparison between methods used the same-cropped images and number of slices for consistency. The original grey-scale images were cropped using the same exact vector in MatLab (The MathWorks Inc.). The circular crop area was chosen based on a diameter that encompasses a large portion of the sample to remove the column wall, while maintaining a reasonable representative volume, REV. The cropped slices were used as the input grey-scale volume for further processing using two segmentation approaches, as explained in the following two sub-sections.

3.4.1 Image Analysis—Method 1

The governing principle for Method 1 is to use the best image to represent a particular phase, and is developed with the goal for analysis of natural complex porous media. There are three approaches in the evolution of Method 1, which are discussed in detail in Appendix B.

The quantitative image analysis is achieved using Blob3D, a software package written using IDL© language (ITT, Visual Information Solutions), and specifically

designed for processing large three-dimensional computed tomography data sets. The software is available free of cost, and offers the ability to distinguish several components of interest sequentially, and uses an interactive user interface. The program extracts information within the data volume, such as number of blobs, surface area, and phase-volumes. The surface area extracted is based on an isosurface created during the separation procedure (post-segmentation step). The isosurface surrounds the phase voxels. As noted by Porter and Wildenschild (2009), a Marching Cubes algorithm is used to determine areas associated with the isosurfaces. The volumes are calculated for each phase based on the number of voxels it occupies (BLOB3D manual). Details on how Blob3D handles each step can be found in Ketcham, (2005). A brief description is also provided in Appendix B. Several researchers have used it to quantify interfacial areas, (e.g. Costanza-Robinson et al. 2008; Schnaar and Brusseau 2005, 2006a, 2006b; Brusseau et al. 2007; Brusseau et al. 2008; Narter 2012).

The above-the-edge and below-the-edge image data are used for segmentation of air and solid respectively. During the first iteration, the two phases are segmented independently using a user selected global threshold. This approach relies solely on the grey-level information, and does not account for spatial variability within the sample. When the phase of interest is air, the grey-scale value is measured for multiple random sections of clearly discernible air and solid phases. The threshold value is set to fall at the midpoint value between the values of the target phase and other phase in the array. Median smoothing was used to suppress the noise inherent to the raw image data. Median smoothing filter reduces noise by replacing a voxel with the median greyscale values

from closely surrounding voxels, with minimal alteration to phase geometry (Blob3D user manual; Brusseau et al. 2006, 2008, 2009; Porter and Wildenschild, 2009). It also helps to avoid the creation of pixilation artifacts around the solid grains, which can erroneously increase the calculated surface area.

Once the threshold value has been set, the image segmentation is initiated. All components were separated automatically due to the presence of numerous air blobs, and to eliminate user bias. While feasible for simpler systems such as Glass Beads, manual separation is cumbersome when applied highly heterogeneous media such as Vinton sand. After binarization of A-image (air) and B-image (solid) are completed, the two individual binary image sets are combined using IDL. This combination creates another binary file whereby each phase in the combined image is represented by a distinct, single grey-scale value, this file is then used as input for another round of segmentation, and the images are segmented sequentially (air, solid, water). This approach uses the mass-balance continuum concept that the sum of the volumes of all segmented phases should equal the total volume analyzed. Hence, the S_w from air ($1-S_n$) should closely match that obtained directly from water analysis. Likewise, the porosity based on the sum of voids should be equal to the porosity obtained from the solid analysis, $(V_{air} + V_{water} + V_{solids}) = V_{img}$. All parameters are calculated using the areas and volumes extracted directly from the Blob3D software (Ketcham 2005). Note that when all three phases are segmented from one set of images, the software ensures that pixels attributed to one phase cannot be assigned to another phase (eliminating phase overlap). Schnaar and Brusseau (2006) and Costanza-Robinson et al. (2008) used a similar combination

technique, employing independent segmentation of air and water. Culligan et al. (2004, 2006) and Porter and Wildenschild (2009) used a similar method employing independent segmentation of air and solid.

3.4.2 Image Analysis—Method 2

This method is based on grey-scale clustering and simultaneous multiple-phase segmentation. This method does account for intra-phase spatial variations of grey scale. The several stages of processing are combined into a MatLab program, PMIA (Kulkarni et al. 2012). The algorithm used for segmentation is a semi-automated code based on Markov-Random Field image model with ICM optimization and k-means seeding. It is a three-dimensional multiphase code that only uses one dataset for segmentation of all 3-phases, either above or below the iodine edge. Thus, there are no error-prone alignment and subtraction analysis required. Further information regarding the algorithm and its routines is discussed in detail in Iassonov et al. (2009b) and Kulkarni et al. (2012).

For the analysis of the data presented here, the images were not subjected to pre-processing (filtering) prior to segmentation. Instead, an applied connected component-labeling (CCM) filter was used after segmentation to remove small unrealistic voxel clusters. For example, voxels enclosed by another phase due to noise, or presence of bright oxides in the grain. After segmentation, the phase volumes were calculated by means of voxel counting. These volumes are used for calculating the porosity and volumetric water contents. The range of image intensity exhibited in Vinton sand samples (low contrast between the water and solid phases) required an initial seeding value to

initialize the segmentation process using Method 2. This value was established by the operator, in contrast to the automated approach used in the analysis of the 45/50 and Glass beads samples.

The next step was to apply different methods for extracting surface areas for all phases. The methods described in Lindblad (2005) and Windreich et al. (2003), as well as surface counting were thoroughly tested on a sphere, a cylinder, and a cube at varying resolutions. For the surface-counting method, the total area of a digitized element is obtained by summing all of the surface area of the voxels comprising that element. However, this approach leads to overestimation of surface areas due to pixilation (e.g., Porter and Wildenschild 2009). Based on the initial evaluation (data not shown), the Lindblad approach provides the best results for known geometrical shapes, and was chosen in this work (M2) for the calculation of surface areas.

The Lindblad approach counts the number of occurrences of a set of local configuration of neighboring voxels. Each voxel is classified based on the number of face-neighbors, and each configuration is assigned a contribution weight. Lindblad used a Monte Carlo optimization approach for determination of optimal weights for a 2x2x2 (binary voxel) configuration. The total surface area of an object is then calculated by summing the local contributions over the surface of the object. Increasing the number of possible configurations improves estimates of surface area contributions (Lindblad 2005). Note that the Lindblad (2005) configuration is in essence equivalent to the Marching Cube surface reconstruction algorithm, and thus the configurations implemented in this approach are the same. However, this approach avoids topological ambiguities posed by

the standard Marching Cube algorithm (Lindblad, 2005). In a comparative study, Porter and Wildenschild (2009) investigated various commonly used algorithms for estimating surface areas. Overall, their results indicate that the binary Marching Cube approach yields optimal results with minimal error compared to laboratory measurements (Porter and Wildenschild 2009).

Pre-processing of microtomographic data prior to segmentation by application of various filter and smoothing steps is standard practice. It was hypothesized that the use of advanced segmentation approaches with M2 may negate the need for such pre-processing. This hypothesis was tested by conducting one complete set of data processing wherein no filtering or smoothing was conducted. A second set of data processing was then conducted wherein standard filtering and smoothing functions were applied. For the latter case, median smoothing and unsharp filtering were applied uniformly to the entire domain. In this stage, the user examined the binarized image and applied the CCM post-processing filter to remove small segmentation errors in segmentation, and optimize the post-processing component. The application of filters was based on several subsample test sequences, and optimized for the majority.

3.4.3 M1-M2 Hybrid Method

The hybrid method was used to ensure that extraction of surface area and volume data were solely a function of segmentation algorithms rather than phase volume and area calculation methods. Thus, trinary (i.e. one binary value assigned to each of the three phases) images segmented using Method 2 program were used as input for data

extraction using the Method 1 segmentation program, Blob3D. The threshold selection for re-segmentation was in this case simple, since the images had already been processed and each phase had already been assigned a unique greyscale value. This approach simply re-segments the trinary images using software from M1. It then uses the newly segmented data to re-calculate volume and surface areas. No filters were used for the re-segmentation process.

3.5 Interfacial Area Data Analysis

The total surface area of air, the nonwetting phase was used to determine total air-water interfacial area (A_{aw}). This is based on the assumption that all porous medium grains are solvated by water, including thin films of which are not resolved by the microtomography method. The interfacial areas reported in this work represent the specific interfacial area, unless otherwise noted, with units of cm^2/cm^3 or cm^{-1} . The surface areas are normalized by the imaged domain volume, for comparison of various samples and interfacial areas at different water contents.

Additional data processing was conducted to determine capillary interfacial area. Specific capillary interfacial area (C_{aw}) was calculated as one half of the difference between the combined sum of the water phase and air phase surface areas and the solid phase surface area (e.g., Montemagno and Ma, 1997; Dalla et al., 2002); where a_a , a_s , a_w , indicates the specific total surface areas of air, solid, and water phases respectively (equation 1):

$$C_{aw} = \frac{1}{2}(a_a + a_w - a_s) \quad (1)$$

The capillary interfacial area calculated from equation (1) refers to interfaces associated with the menisci of contacts between air and “bulk” water (partially filled capillaries, pendular rings, and wedges). This equation is developed from a simple phase-balance analysis of surface areas and interfacial contacts in a three-phase (solid, wetting fluid, non-wetting fluid) porous medium. Water films are assumed to be absent for this model.

3.6 Performance Evaluation

The main objective of this study was to compare two image-processing procedures and assess their suitability for characterization of fluid-fluid interfacial areas in natural porous media. The quality of the outputs of Method 1 and Method 2 are assessed based on comparison to independently measured parameters to the extent possible. This is of particular importance to determine the reliability of C_{aw} values obtained using these two methods.

First, the volume of each phase is evaluated to ensure mass balance. The sum of volume of air (V_a) and volume of water (V_w) equals the volume of voids (V_v). The volume of voids can also be calculated based on the segmented volume of solids (V_s). This is accomplished by subtracting the resulting volume of solids (V_s) from the total imaged volume (V_t). The total imaged volume (V_t) is obtained by summing all resulting volumes, or by calculating it independently from geometrical considerations (measured diameter and length of imaged domain). The two values of V_s should be consistent.

The volume of voids divided by the imaged volume also determines porosity ($n = V_v/V_t$). The porosity from image analysis is compared to porosity calculated from the measured bulk density value obtained during column preparation. This latter value is used as a benchmark for the porosity values obtained from the segmented data.

Water saturation (S_w) can be calculated using either the volume of water, V_w/V_v , or the volume of air, ($=1-(V_a/V_v)$). In this study, the S_w determined by volume of water will be used in most cases when the wetting phase is processed. The water content can also be measured when practical, and can be used for benchmarking the S_w data.

It is common to measure the solid surface area to characterize porous media. The volume-normalized specific solid surface areas are calculated from segmentation of solid surface area directly. A theoretical value can be calculated with the assumption that the surfaces of the solids are smooth. The geometrical smooth-sphere surface area (GSSA) $= 6(1-n)/d_{50}$, where d_{50} is the mean particle diameter. This value is calculated for each method using their respective calculated porosities and the mean particle diameter (Table 1). Measured values of solid surface area are obtained using the N_2 -Brunauer, Emmet and Teller (BET) technique. This value represents the total solid surface area available in the system as measured by adsorption of gas molecules onto the solid surface (e.g. Orchiston 1953; Brunauer et al., 1938), and incorporates surface area associated with microscopic surface roughness. NBET values can be used as a benchmark for the Glass Beads used in this work as they have been confirmed to have smooth surfaces (Narter and Brusseau, 2010).

For the evaluation of total (measurable) interfacial area, (A_{aw}), the maximum interfacial area (A_{max}) is used. This value is an index for a given system, effectively a measure of a theoretical maximum interfacial area in a system (*Brusseau et al.* 2009, 2010) for a given technique. The A_{max} is calculated from the linear regression from the relationship between A_{aw} and S_w . The A_{max} can be compared to geometric smooth sphere (GSSA) values, considering that the maximum air-water interfacial area is associated with the condition of an infinitesimally thin layer of water solvating the solid surface. Under such conditions, it is anticipated that the corresponding interfacial area will be similar to the solid surface area. Unfortunately, there is no direct independent parameter to quantify the capillary interfacial area C_{aw} . The suitability of each segmentation Method for estimating C_{aw} is contingent upon scrutiny of the total A_{aw} , the specific solid surface area (SSA), porosity, and segmented volumes.

4. RESULTS AND DISCUSSION

4.1 Phase Volumes, Porosity, and Water Saturation

Figure 1 shows the volumes of the air, water, and solid phases for 45-50 mesh Accusand. The volumes of each phase are obtained directly from the resulting segmented images using Method 1 and Method 2. The volume of air is observed to increase linearly with drainage while the volume of water decreases accordingly (Figure 1). This behavior is consistent with the drainage procedure, which begins with a saturated porous medium. Similar results are observed for glass beads (Figure 2) and Vinton soil (Figure 3). The volumes of all phases as a function of experimental steps are presented in Appendix C for

all porous media, to eliminate the impact of differences in water saturations obtained with the methods.

The volume of air (Figure 1, 2, 3) determines the non-wetting phase saturation (S_n) and provides data for an indirect calculation of the wetting-phase saturation ($S_w=1-S_n$). The volume of water provides direct calculation of S_w . Figure 4 shows the correlation between wetting-phase saturation obtained from segmenting the water phase using Method 1 and Method 2. The figure shows that the two sets of values correspond well to one another, although minor discrepancies are observed, such that the points do not fall in the ideal 1:1 line. This inconsistency is attributed primarily to differences in the volume of water determined for the segmentation methods. Small variations in the volume of air and water can affect the overall calculated S_w values.

Figures 1, 2, and 3 compare the volume of solids as a function of S_w using Method 1 and Method 2. For 45-50 sand (Figure 1), the difference in the resulting segmented volume of solids is less than 1%, with a maximum (3%) difference occurring at S_w of approximately 0.33. The differences obtained between M1 and M2 versus the hybrid (M1-M2) method are 1%. For the Glass Beads sample (Figure 2), the volume of solids varies on average 3% between Method 1 and Method 2, ranging from 1% to 4%. For Vinton sand, the average difference in the volume of solids is 5% between M1 and M2.

The same volume (cropping region and length) was used for the image data for each experimental step to eliminate potential errors due to the characterization of different domains. Thus, the volume of solids is expected to remain constant at each drainage step, and therefore serves as a means to test replicate measurement of the

imaged domain. The solid volumes vary somewhat per experiment step, particularly for Vinton soil. However, the coefficients of variation are 5% or less for the data sets. This relatively low variability supports the general robustness of the procedures used to obtain and process the image data.

The volumes of solids can be used, along with the measured particle densities (GB=2.213, 45/50= 2.368, Vinton=2.494 g/cm³), to calculate the bulk densities for the imaged domains. These values (GB=1.31, 45/50=1.72, Vinton=1.67 g/cm³) are very similar to the independently measured values obtained for the entire column (GB=1.30 45/50= 1.74, Vinton=1.53 g/cm³).

The volume of solids can also be used to estimate porosity of the imaged domains, which can be compared to independently measured column-scale values based on the gravimetric measured bulk density. Table 1 shows the values obtained for porosity for Methods 1 and 2. Even though the 45-50 and Vinton sands are heterogeneous, the porosity from each drainage step (V_v or V_s) is expected to have little deviation between one another, as well as from the independent gravimetric measured porosity. When comparing the results for porosity, we observe approximately 1% variability between each water saturation step, and approximately 5% difference between calculated and independent porosity values for the porous medium.

Figure 4 highlights the relationship between porosities and water saturation (S_w) based on the analysis of the fluids and of the solids for the Glass beads, Accusand, and Vinton sand, respectively. Results show that the volume of voids obtained from image analysis of the solid phase is very close to the volume of voids obtained from analysis of

air and water phases. Likewise, the water saturation obtained directly from the water phase analysis is comparable to the saturation based on the air-phase analysis ($S_w=1-S_n$). These results indicate that a high degree of phase balance exists, which means that issues such as phase overlap were minimized for both methods. Application of Method 2 offers the advantage of simultaneous multiphase segmentation, compared to the multi-step procedure used for M1.

4.2 Phase Surface Areas

Figures 1, 2, and 3 show the surface areas of all phases (air, water, and solid) as a function of water saturation, obtained from segmented images using Methods 1 and 2. Similar plots are also shown in Appendix C as a function of experimental step. The surface area of air for the 45-50 sand is shown Figure 1. The results obtained from Method 1, Method 2, and the hybrid M1-M2 method are generally comparable, with an average difference of 7% between M1 and M2, 6% between M2 and the hybrid, and 12% between M1 and the hybrid approach. Figure 2 shows the air surface area results for the Glass Beads sample. The difference between M1 and M2 ranges between 23-50%, with an overall average difference of 32%. Figure 3 shows the surface areas of air for Vinton sand. The values obtained using M2 is consistently higher than M1, with an average difference of 39%, varying between 20-73%.

The surface areas of water, the phase most sensitive to image processing, are presented in Figure 1 for 45-50 sand. The surface area of water obtained from M2 is once again observed to be higher than surface areas obtained by M1, with an average

difference of 18%, ranging between 1% and 37%. For M1-hybrid the difference is 23%, and between M2-Hybrid 6%. In general, results obtained from segmentation using M2 are expected to be very similar to results obtained using the hybrid (M1-M2) method, since segmentation was obtained using M2. Figure 2 shows the surface area of water for the Glass Beads sample. It is observed that the surface area of water for M1 is less variable than that obtained using M2. On average, the difference between the surface areas of water obtained with the two methods for Glass beads is 42%, ranging between 24-58%. The variability for Glass Beads between the methods is approximately two times the average difference observed for 45-50 sand.

Figure 3 shows the surface area of water for Vinton sand. The mean absolute difference in surface areas between the two methods is 13%, ranging between 1% and 21%. The last two steps corresponding to S_w of 0.64-0.61 respectively are anomalous. Inspection of the segmented binary data for these steps in particular, resulted in higher wetting-phase saturation, suggesting the possible misclassification of the water phase. Method 2 shows a decreasing water surface area in contrast to M1. In total, the surface areas obtained with M2 were generally higher than those obtained with M1 for all phases for all three media.

For all porous media samples, the surface area of water is generally observed to remain fairly constant for all drainage steps even though water is drained from the column. While the surface area of water should remain constant for a water-wetting medium due to the presence of water film, this behavior is not expected to be observed for microtomography, given that thin wetting films are not resolved by the method. Thus,

the observed minimal change in water surface area, particularly for 45-50 sand and glass beads (for which drainage proceeded to relatively low saturations), must reflect artifacts of image processing. This was tested by re-processing the 45-50 and glass-bead data sets using method 2, this time with the application of noise-reduction filters. The results obtained for the 45-50 medium with filtering exhibit the expected decrease in water surface area (see Figure 1). In addition, the filtering resulted in lower magnitudes of surface area than the original M2 approach. These results suggest that in some instances images at lower water saturations may have been affected by noise such that noise-reduction filtering was required for accurate segmentation. Similar results are also observed for the glass beads (data not shown).

The surface areas of solids are presented in Figures 1, 2, 3 for 45-50, glass beads, and Vinton soil, respectively. Just as the volume of solids is expected to remain constant for each experiment step, the surface areas resulting from multiple solid-phase analyses should be similarly constant. The coefficients of variation for solid surface areas are 4% for M1 and 3% for M2 and 4% Hybrid for 45-50 sand. Method 1 has a 3% coefficient of variation for both the Glass Beads and Vinton sand. Meanwhile, a 4% variation is calculated for Vinton sand for M2. These results support the robustness of the methods. However, for the glass beads, a much larger coefficient of variation (14%) is calculated for the M2 data.

There is an average difference of 4% between M1 and M2 for the surface area of solids for 45-50 sand, 9% difference between M2 and the hybrid, and 12% between M1 and the hybrid. The solid surface areas of the Glass Beads from M2 are approximately

two times those obtained from M1. This difference is greater in steps 5 and 6 ($S_w \sim 0.17-0.23$), where it reaches a maximum of 81% and 78%, respectively. The average difference between methods is 15%, ranging between 9% and 21%, for Vinton sand.

The volume-normalized specific solid surface area (SSA) is calculated directly from segmented solid phase data. Results are listed in Table 2. The reported values are comparable to values reported in the literature, $91 \pm 12 \text{ cm}^{-1}$ for 45/50, $30 \pm 2 \text{ cm}^{-1}$ for Glass Beads, and 142-151 cm^{-1} for Vinton sand (Brusseau et al 2007; Brusseau et al. 2008; Brusseau et al. 2009; Narter and Brusseau 2010). Differences in SSA values determined with the two methods are observed for all three media. Particularly noteworthy is the large difference observed for the Glass Beads, with 65 cm^{-1} for M2, and 34 cm^{-1} for M1.

For further evaluation, the specific solid surface area determined for the Glass Beads is compared to two independent measures. The first is a calculation based on geometrical considerations for a pack of smooth spheres (GSSA). The GSSA is calculated for each method using their respective porosities (obtained from the image data) and the mean particle diameter (Table 1). The second independent measure is the specific solid surface area based on the NBET measured solid surface area and the image-based bulk density (Table 2). The Glass Beads are used for the comparison given that they can be treated as a monodisperse pack of smooth spheres. The GSSA value ($31 \pm 0.01 \text{ cm}^{-1}$) is very similar to the specific solid surface area determined using measured NBET data (27.5 cm^{-1}), supporting the robustness of the GSSA estimation for this medium. The SSA calculated using the M1 data ($34 \pm 1 \text{ cm}^{-1}$) is slightly larger than the two independent specific solid surface area values. This result indicates that the image segmentation and

processing for M1 produced a reasonably accurate representation of the Glass Beads. Conversely, the SSA determined using M2 data ($65 \pm 6 \text{ cm}^{-1}$) is significantly larger than the two independent SSA values. Differences in segmentation results of Glass Beads may be attributed to the absence of noise-reduction filters for application of Method 2. Processing the glass beads with filters resulted in a SSA of 31 cm^{-1} , which is similar to the independent values. This improved processing was enhanced by using the contrast-enhanced images (above the edge). Analysis of A-edge images without the use of filters showed improvement in resulting SSA value, although the noise present in the solid phase was clearly observable (data not shown).

The use of filters such as median smoothing helps to reduce noise in the greyscale image and help sharpen the boundaries between two objects (e.g. Tuller et al. 2013; Kaestner et al., 2008; Costanza-Robinson et al. 2008; Wildenschild and Sheppard 2013). Pixilation effects have been observed in other studies (e.g. Costanza-Robinson et al. 2008). Culligan et al. (2004) used a local threshold method for a mixed-size glass beads system. Still, they reported having user-assisted threshold value selection to locate the wetting-nonwetting, wetting-solid, and nonwetting-solid interfaces in any given volume. They also attributed their difficulties to the overlap of the water and solid phases in the gray-scale histogram. The segmentation of glass beads may also be influenced by the brightness of the beads. Since they are translucent, x-rays absorption intensity without the presence of the dopant (Appendix B, Figure 9) may be too similar to the water phase, and any edge artifacts inherent in tomography technology are likely enhanced. This particular problem in distinguishing the boundaries of solid and water phase was a significant

motivation for the work presented herein, including the development of Method 1 (Appendix B).

4.4 Total Air-water interfacial Area

The total air-water interfacial areas (A_{aw}) obtained using Method 1 (ISSP) and Method 2 (PMIA) are shown in Figure 5 for 45/50 sand, Figure 6 for glass beads, and Figure 7 for Vinton sand. Values obtained with M2 are higher than those obtained with M1 for all porous media, consistent with the larger phase surface areas obtained with M2. Figures 5-7 also shows the calculated 95% confidence intervals for both Method 1 and Method 2. The upper and lower limits for the 95% confidence intervals are calculated from the regressions.

For 45-50 sand, the results for both methods fall within the calculated upper and lower ranges. Therefore, A_{aw} results using M1 and M2 segmentation methods are considered to be statistically similar. For Glass beads (Figure 6), there is a large difference between A_{aw} values obtained with M1 and M2, and the 95% confidence intervals do not overlap. This is attributed to the significance differences observed for the air surface areas, as discussed above. For Vinton sand (Figure 7), while there are some significant differences, the confidence intervals of the two methods overlap. Figure 5 also shows the result for A_{aw} obtained from the hybrid M1-M2 test. Results show that the hybrid values are very similar to M2. Thus, confirming that the differences in methods arise mainly from the inner-workings of the segmentation process, such as threshold

selection and phase identification. The key factor influencing the robustness of the A_{aw} is attributed to the segmentation step rather than the separation stage of image analysis.

The accuracy of the total air-water interface results was evaluated by comparing the maximum estimated interfacial area, (A_{max}) to measured values of the specific solid surface area (Brusseau et al., 2008; Brusseau et al., 2009; Schnaar 2006; Schnaar and Brusseau 2006a; Narter and Brusseau 2010). The A_{max} is calculated based on the linear regression from the relationship between A_{aw} and S_w . Table 2 shows the A_{max} for each segmentation approach. For 45-50 sand, the A_{max} values estimated from both Methods are comparable to the SSA values for M1 (105 cm^{-1}) and M2 (109 cm^{-1}) determined using the microtomography data. These results support the contention that both methods produce reasonable values for A_{aw} for 45-50 sand. The A_{max} for Vinton sand is 144 cm^{-1} (M1) and 170 cm^{-1} (M2). In both cases, the A_{max} values are smaller than the SSA measured directly from image analysis using M1 (190 cm^{-1}), and M2 (223 cm^{-1}).

For Glass Beads media, the A_{max} value obtained using M1 is $29 \pm 1.4 \text{ cm}^{-1}$. This value is comparable to the calculated GSSA value ($31 \pm 0.01 \text{ cm}^{-1}$) and the imaged based NBET-measured value (27.5 cm^{-1}), and to the gravimetric based $28 \pm 2 \text{ cm}^{-1}$ reported in Narter and Brusseau 2010 for Glass Beads. For M1, the similarity of A_{max} to the independent measures of solid surface area suggests that Method 1 produced an accurate measurement of A_{aw} . For M2, the A_{max} is 39 cm^{-1} , approximately 30% larger than the independently determined solid surface area, and GSSA ($31 \pm 0.01 \text{ cm}^{-1}$) values. Interestingly, this disparity is much smaller than the difference between the image-based SSA (65 cm^{-1}) and the independent values. This suggests that segmentation of the air

surface area by M2 was not as problematic as it was for the solid surface area. As previously discussed, pixilation effects are likely to have contributed to the general overestimation of all surface areas using M2. The application of noise reduction filters resulted in an A_{\max} value of 28 cm^{-1} , a significant improvement.

4.5 Capillary air-water interfacial area

Figure 8 shows the capillary-associated interfacial area measured using M1 and M2 for 45-50 sand. The results show substantial differences obtained from the two methods. The capillary-associated interfacial areas (C_{aw}) obtained by M2 and the hybrid approaches are larger than obtained using M1. These disparities are related to the differences in the magnitudes of the phase surface areas (Figure 2) determined with the two methods previously discussed. The profiles exhibited by the C_{aw} - S_w functions do not match the expected behavior for capillary interfacial area, wherein the area first increases during drainage and then decreases at lower saturations (e.g., Reeves and Celia 1999; Dalla et al. 2002; Culligan et al. 2004; Culligan et al. 2006; Brusseau et al. 2007; Porter et al. 2009; Schaap and Tuller 2010). The additional M2-filtered analysis also presented in Figure 8 uses M2 as the primary segmentation with a noise reduction filter not used in the standard M2. The results for this data set better represent the expected behavior, indicating that M2 with filtering provided a more robust determination of C_{aw} compared to the other two methods.

Figure 9 shows the capillary-associated interfacial area for Glass Beads. Differences between M1 and M2 are observed to begin at lower water saturations

($S_w < 0.40$). The calculated C_{aw} from Method 1 is observed to yield higher values than Method 2. The lower C_{aw} obtained from M2 can be related to the overestimation of solid surface area. The specific capillary interfacial area relationship (equation 1) indicates that higher values of solid surface areas (i.e., SSA) will decrease the value of capillary interfacial area.

Figure 10 shows the capillary-associated interfacial area for Vinton sand. The differences in capillary interfacial area values obtained with the two methods are very small compared to the other media. For Vinton sand (Figure 10), the lack of low S_w data precludes evaluation in terms of method performance at lower saturations (<65%). As previously discussed, the heterogeneity of the grains, in terms of size and distribution, and grain density can contribute to uneven attenuation, leading to noise in the original grey-scale image. The considerable differences in the physical characteristics of the Vinton sand relative to the other sand in this study, segmentation using M2 required the manual input of seeding values by the user to ensure proper initial conditions. It has been commonly noted that to achieve better segmentation of geological media, still require some form of user input albeit using improved local threshold methods (e.g. Baveye et al. 2010a; Wang et al. 2011; Hapca et al. 2013; Wildenschild and Sheppard 2013). The decrease in surface area of water as a function of decreasing water saturation obtained with M2 (Figure 3) suggests that M2 may have indeed improved segmentation of the water phase in this complex medium.

4.5.1. Comparison to Prior Research

There are limited data with which to compare results from this study. Dalla et al. (2002) produced simulated capillary and total nonwetting-wetting interfacial areas using a computational model. For this model, they created a synthetic smooth-sphere pack based on a given porosity (0.36), bulk density (1.72 g/cm^3), and grain size distribution ($d_{50} \approx 0.33 \text{ mm}$, $U \approx 2.2$). The porous medium was designed to resemble the porous media described by Kim et al. (1997). The synthetic medium was used to generate drainage simulations and associated interfacial area computations. The simulation results produced a maximum total interfacial area (A_{max}) of approximately 100 cm^{-1} . The corresponding capillary interfacial area (C_{aw}) is approximately 31 cm^{-1} at its peak at the corresponding $S_w = 0.25$. This synthetic porous medium is comparable to the 45-50 sand in terms of porosity, bulk density, and median grain size. The A_{max} values obtained with both M1 and M2 are comparable to the A_{max} reported by Dalla et al. (2002) for the synthetic medium. In addition, the C_{aw} obtained with M1 (maximum C_{aw} of 30 cm^{-1} occurring at $\sim 0.22 S_w$) is very similar to the simulated value reported by Dalla et al. Such is not the case for the values obtained with M2 (maximum $C_{\text{aw}} = 50 \text{ cm}^{-1}$).

Culligan et al. (2004) presented measured capillary interfacial values for Glass beads ($d_{50} = 0.87 \text{ mm}$) for various drainage and imbibition cycles. The maximum C_{aw} is $\sim 2.7 \text{ cm}^{-1}$ at $S_w \sim 0.30$. These values are much lower than the capillary values obtained herein for glass beads (Figure 9). Method 2 yields the closest value at $S_w 0.2$ with C_{aw} approximately 7.5 cm^{-1} . Porter et al. (2009) used a multiphase lattice-Boltzmann model to simulate drainage and imbibition data using measured data reported by Culligan et al.

(2004). They simulated a C_{aw} between 3.5-4.0 cm^{-1} occurring at S_w between 0.30-0.35 depending on the initial condition of the model. Brusseau et al (2009) measured total A_{aw} for several porous media using NAPL-water systems. For 1-mm Glass Beads they measured A_{max} of 34 cm^{-1} . Porter et al. (2010) reported results for models simulating drainage and imbibition cycles for non-aqueous phase liquid (NAPL)-water systems. The total A_{max} for these Glass Beads is 32 cm^{-1} , with a $C_{aw}=3.7 \text{ cm}^{-1}$ at $S_w \sim 0.27$. The capillary interfacial area values are much lower, especially for the Glass Beads.

For 45-50 sand, Brusseau et al (2009) reports A_{max} of 113 cm^{-1} for 45-50 NAPL-water system. These results are fall within the confidence interval calculated for the air-water system presented here. For this particular porous media total interfacial areas measured using NAPL-water systems are comparable (e.g. Brusseau et al. 2006; Brusseau et al. 2008; Brusseau et al. 2009; Brusseau et al. 2010). For Vinton sand, Brusseau et al. (2007) report measured A_{max} as 147 cm^{-1} and $C_{aw}=36 \text{ cm}^{-1}$ at much higher water saturation of 0.52. The capillary value is comparable to M2 (Figure 10). However, at $S_w=0.7$ the C_{aw} for both M1 and M2 are in range with values reported by Brusseau et al. (2007). The estimated maximum total interfacial areas are similar to the air-water system values obtained from the results presented herein (Figure 5-7, 8-10).

5. CONCLUSIONS

This study was conducted to compare two image-processing procedures for characterizing fluids and associated interfaces in natural porous media. The two approaches included (a) a simpler method employing global thresholding and sequential

single-phase segmentation (M1), and (b) a more complex method applying local threshold selection for simultaneous multiple-phase segmentation (M2). The volumes of air, water, and solid phases were used for quantitative comparison to independently measured porosities. These were used as benchmarks to evaluate robustness of segmentation methods.

The results from performance evaluation of 45-50 (Figures 1 and 7) and Vinton (Figures 3 and 9) media suggest both M1 and M2 results are sufficiently comparable. However, the glass bead sample comparison to independent parameters revealed noteworthy differences in the segmented solid surface areas using Method 2. These differences are attributed to pixilation effects caused by difficulties in boundary identification, and are speculated to have contributed to the overestimation of surface areas. As such, it is possible that these errors affect all of porous media studied, even if minimally. This hypothesis was tested by reprocessing the data with noise-reduction filters applied to M2 segmentation (M2-filt.). This scenario led to significant improvement of the measured surface areas of water and solid phases.

The segmentation of water phase is vital in the determination of capillary interfacial area. The quality of the capillary analysis is based on comparison of the water saturation, independent porosity, and the overall mass balance of the total segmented volume (V_t). Individual assessment of air and water surface areas and volumes evaluated against independent parameters are the most reliable indicator of dependable capillary interfacial area results. The C_{aw} values obtained using Method 1 for the Glass Beads was more consistent based on the criteria established to determine reliability in this study.

However, inspection of the data suggests that M2 improves determination of the capillary interfacial area for the two natural porous media, especially at low saturations, due to perceived improvement in the segmentation of the water phase.

Method 1 uses image analysis software that offers the advantage of a multiplatform user interface, which does not require the full version of proprietary software (e.g. IDL). The main advantage is the ability to visualize the blobs and the pre-segmentation stages, such as threshold selection. However, it requires heavy use of expert time. The major disadvantage of M1 is the multiple steps necessary prior to obtaining a trinary image ready for analysis.

It was hypothesized that M2 would better detect the water phase at lower saturations, due to its local threshold selection in the segmentation stage of analysis. A main advantage of Method 2 is its ability to segment all desired phases simultaneously from a single grey-scale image, allowing for the discrimination of intermediate greyscales often overlooked by global thresholding methods (e.g. M1). The advantage of using this information is improved segmentation with less voxel misclassification (e.g. Wang et al. 2011, Houston et al. 2013a). Method 2 is very computational intensive due to its local threshold approach. However, M2 can be automated and processed in batches instead of manual processing.

Nonetheless, difficulties encountered in segmenting the surface area of the glass beads sample illustrate the continued need for user assistance in processing microtomographic image data. Especially considering that the reliability of estimated capillary interfaces is centered upon comparison of the surface area of air and solid

phases and total air-water interface to independently measured parameters. Quality control is a must to ensure that the program is segmenting the correct phases, and misclassifications are minor. There is good potential for advances using M2 with the implementation of advanced locally adaptive automated algorithms, and possibly more advanced system characterization features such as fluid-fluid contact, fluid configuration, and connectivity of phases. All offer new horizons for future interfacial area research using high resolution imaging technology.

5.1 Acknowledgments

The authors would like to thank Dr. Mark Rivers (APS), Dr. Marcel Schaap (The University of Arizona), and the UA Contaminant Transport Group for their assistance in data collection. This research was supported by the NIEHS-Superfund Research Program (Grant ES 04940). Use of the Advanced Photon Source, an Office of Science User Facility operated for the U.S. Department of Energy (DOE) Office of Science by Argonne National Laboratory, was supported by the U.S. DOE under Contract No. DE-AC02-06CH11357. We acknowledge the support of GeoSoilEnviroCARS (Sector 13), which is supported by the National Science Foundation—Earth Sciences (EAR-1128799), and the Department of Energy, Geosciences (DE-FG02-94ER14466).

6. REFERENCES

- Altman, S. J., W. J. Peplinski, and M. L. Rivers (2005a), Evaluation of synchrotron X-ray computerized microtomography for the visualization of transport processes in low-porosity materials, *Journal of Contaminant Hydrology*, 78(3), 167-183.
- Altman, S. J., M. L. Rivers, M. D. Reno, R. T. Cygan, and A. A. McLain (2005b), Characterization of adsorption sites on aggregate soil samples using synchrotron X-ray computerized microtomography, *Environmental Science & Technology*, 39(8), 2679-2685.
- ASTM (American Society for Testing and Materials), (1992). Standard guide for computed tomography (CT) imaging, ASTM designation E 1441-92a, in 1992 annual book of ASTM standards, section 3 metals test methods and analytical procedures: Philadelphia, ASTM, pp. 690-713.
- Baker, D. R., L. Mancini, M. Polacci, M. D. Higgins, G. A. R. Gualda, R. J. Hill, and M. L. Rivers (2012), An introduction to the application of X-ray microtomography to the three-dimensional study of igneous rocks, *Lithos*, 148, 262-276.
- Baveye, P. C., et al. (2010a), Observer-dependent variability of the thresholding step in the quantitative analysis of soil images and X-ray microtomography data, *Geoderma*, 157(1-2), 51-63.
- Baveye, P. C., et al. (2010b), Observer-dependent variability of the thresholding step in the quantitative analysis of soil images and X-ray microtomography data, *Geoderma*, 157(1-2).
- Brown, K., S. Schluter, A. Sheppard, and D. Wildenschild (2014), On the challenges of measuring interfacial characteristics of three-phase fluid flow with x-ray microtomography, *Journal of Microscopy*, 253(3), 171-182.
- Brunauer, S., P. H. Emmett, and E. Teller (1938), Adsorption of gases in multimolecular layers, *Journal of the American Chemical Society*, 60, 309-319.
- Brusseau, M. L., M. Narter, and H. Janousek (2010), Interfacial Partitioning Tracer Test Measurements of Organic-Liquid/Water Interfacial Areas: Application to Soils and the Influence of Surface Roughness, *Environmental Science & Technology*, 44(19), 7596-7600.

Brusseau, M. L., S. Peng, G. Schnaar, and M. S. Costanza-Robinson (2006), Relationships among air-water interfacial area, capillary pressure, and water saturation for a sandy porous medium, *Water Resources Research*, 42(3).

Brusseau, M. L., S. Peng, G. Schnaar, and A. Murao (2007), Measuring air-water interfacial areas with X-ray microtomography and interfacial partitioning tracer tests, *Environmental Science & Technology*, 41(6), 1956-1961.

Brusseau, M. L., H. Janousek, A. Murao, and G. Schnaar (2008), Synchrotron X-ray microtomography and interfacial partitioning tracer test measurements of NAPL-water interfacial areas, *Water Resources Research*, 44(1).

Brusseau, M. L., M. Narter, S. Schnaar, and J. Marble (2009), Measurement and Estimation of Organic-Liquid/Water Interfacial Areas for Several Natural Porous Media, *Environmental Science & Technology*, 43(10), 3619-3625.

Costanza-Robinson, M. S., K. H. Harrold, and R. M. Lieb-Lappen (2008), X-ray microtomography determination of air-water interfacial area-water saturation relationships in sandy porous media, *Environmental Science & Technology*, 42(8), 2949-2956.

Costanza-Robinson, M. S., B. D. Estabrook, and D. F. Fouhey (2011), Representative elementary volume estimation for porosity, moisture saturation, and air-water interfacial areas in unsaturated porous media: Data quality implications, *Water Resources Research*, 47(7), n/a-n/a.

Culligan, K. A., D. Wildenschild, B. S. B. Christensen, W. G. Gray, and M. L. Rivers (2006), Pore-scale characteristics of multiphase flow in porous media: A comparison of air-water and oil-water experiments, *Advances in Water Resources*, 29(2), 227-238.

Culligan, K. A., D. Wildenschild, B. S. B. Christensen, W. G. Gray, M. L. Rivers, and A. F. B. Tompson (2004), Interfacial area measurements for unsaturated flow through a porous medium, *Water Resources Research*, 40(12), n/a-n/a.

Dalla, E., M. Hilpert, and C. T. Miller (2002), Computation of the interfacial area for two-fluid porous medium systems, *Journal of Contaminant Hydrology*, 56(1-2), 25-48.

Gualda, G. A. R., and M. Rivers (2006), Quantitative 3D petrography using X-ray tomography: Application to Bishop Tuff pumice clasts, *J Volcanol Geoth Res*, 154(1-2), 48-62.

Gualda, G. A. R., A. S. Pamukcu, L. L. Claiborne, and M. L. Rivers (2010), Quantitative 3D petrography using X-ray tomography 3: Documenting accessory phases with differential absorption tomography, *Geosphere*, 6(6), 782-792.

Hapca, S. M., A. N. Houston, W. Otten, and P. C. Baveye (2013), New Local Thresholding Method for Soil Images by Minimizing Grayscale Intra-Class Variance, *Vadose Zone Journal*, 0(0), 0.

Houston, A. N., W. Otten, P. C. Baveye, and S. Hapca (2013a), Adaptive-window indicator kriging: A thresholding method for computed tomography images of porous media, *Computers & Geosciences*, 54, 239-248.

Houston, A. N., S. Schmidt, A. M. Tarquis, W. Otten, P. C. Baveye, and S. M. Hapca (2013b), Effect of scanning and image reconstruction settings in X-ray computed microtomography on quality and segmentation of 3D soil images, *Geoderma*, 207-208, 154-165.

Iassonov, P., and M. Tuller (2010), Application of Segmentation for Correction of Intensity Bias in X-Ray Computed Tomography Images, *Vadose Zone Journal*, 9(1).

Iassonov, P., T. Gebrenegus, and M. Tuller (2009a), Segmentation of X-ray computed tomography images of porous materials: A crucial step for characterization and quantitative analysis of pore structures, *Water Resources Research*, 45(9), n/a-n/a.

Iassonov, P., T. Gebrenegus, and M. Tuller (2009b), Segmentation of X-ray computed tomography images of porous materials: A crucial step for characterization and quantitative analysis of pore structures, *Water Resources Research*, 45.

Kaestner, A., E. Lehmann, and M. Stampanoni (2008), Imaging and image processing in porous media research, *Advances in Water Resources*, 31(9), 1174-1187.

Ketcham, R. A. (2005), Computational methods for quantitative analysis of three-dimensional features in geological specimens, *Geosphere*, 1(1), 32.

Ketcham, R. A., and W. D. Carlson (2001), Acquisition, optimization and interpretation of X-ray computed tomographic imagery: applications to the geosciences, *Computers & Geosciences*, 27(4), 381-400.

Ketcham, R. A., and T. M. Ryan (2004), Quantification and visualization of anisotropy in trabecular bone, *Journal of Microscopy-Oxford*, 213, 158-171.

Ketcham, R. A., and G. J. Iturrino (2005), Nondestructive high-resolution visualization and measurement of anisotropic effective porosity in complex lithologies using high-resolution X-ray computed tomography, *Journal of Hydrology*, 302(1-4), 92-106.

Kim, T. W., T. K. Tokunaga, D. B. Shuman, S. R. Sutton, M. Newville, and A. Lanzirotti (2012), Thickness measurements of nanoscale brine films on silica surfaces under geologic CO₂ sequestration conditions using synchrotron X-ray fluorescence, *Water Resources Research*, 48.

Kulkarni, R., M. Tuller, W. Fink, and D. Wildenschild (2012), Three-Dimensional Multiphase Segmentation of X-Ray CT Data of Porous Materials Using a Bayesian Markov Random Field Framework, *Vadose Zone Journal*, 11(1).

Lindblad, J. (2005), Surface area estimation of digitized 3D objects using weighted local configurations, *Image and Vision Computing*, 23(2), 111-122.

Macedo, A., C. M. P. Vaz, J. M. Naime, P. E. Cruvinel, and S. Crestana (1999), X-ray microtomography to characterize the physical properties of soil and particulate systems.

Nakashima, Y., and S. Kamiya (2007), Mathematica programs for the analysis of three-dimensional pore connectivity and anisotropic tortuosity of porous rocks using X-ray computed tomography image data, *Journal of Nuclear Science and Technology*, 44(9), 1233-1247.

Narter, M. (2012), Characterizing Non-Wetting Fluid in Natural Porous Media Using Synchrotron X-Ray Microtomography, edited, p. 172 leaves, University of Arizona, University of Arizona.

Narter, M., and M. L. Brusseau (2010), Comparison of interfacial partitioning tracer test and high-resolution microtomography measurements of fluid-fluid interfacial areas for an ideal porous medium, *Water Resources Research*, 46.

Oh, W., and W. B. Lindquist (1999), Image thresholding by indicator kriging, *Ieee Transactions on Pattern Analysis and Machine Intelligence*, 21(7), 590-602.

Orchiston, H. D. (1953), Adsorption Of Water Vapor .1. Soils At 25-Degrees-C, *Soil Science*, 76(6), 453-465.

Pal, N. R., and D. Bhandari (1993), Image Thresholding - Some New Techniques, *Signal Processing*, 33(2), 139-158.

Pal, N. R., and S. K. Pal (1993), A Review on Image Segmentation Techniques, *Pattern Recognition*, 26(9), 1277-1294.

Peng, S., Q. H. Hu, S. Dultz, and M. Zhang (2012), Using X-ray computed tomography in pore structure characterization for a Berea sandstone: Resolution effect, *Journal of Hydrology*, 472, 254-261.

Porter, M. L., and D. Wildenschild (2009), Image analysis algorithms for estimating porous media multiphase flow variables from computed microtomography data: a validation study, *Computational Geosciences*, 14(1), 15-30.

Porter, M. L., M. G. Schaap, and D. Wildenschild (2009), Lattice-Boltzmann simulations of the capillary pressure-saturation-interfacial area relationship for porous media, *Advances in Water Resources*, 32(11), 1632-1640.

Porter, M. L., D. Wildenschild, G. Grant, and J. I. Gerhard (2010), Measurement and prediction of the relationship between capillary pressure, saturation, and interfacial area in a NAPL-water-glass bead system, *Water Resources Research*, 46(8).

Remigy, J. C., M. Meireles, and X. Thibault (2007), Morphological characterization of a polymeric microfiltration membrane by synchrotron radiation computed microtomography, *Journal of Membrane Science*, 305(1-2), 27-35.

Rivers, M. L. (2012), tomoRecon: High-speed tomography reconstruction on workstations using multi-threading, *Proc Spie*, 8506.

Rivers, M. L., D. T. Citron, and Y. B. Wang (2010), Recent developments in computed tomography at GSECARS, *Proc Spie*, 7804.

Schaap, M. G., and M. Tuller (2010), Quantitative Pore-Scale Investigations of Multiphase Bio/Geo/Chemical Processes, *Vadose Zone Journal*, 9(3), 573-575.

Schlüter, S., U. Weller, and H.-J. Vogel (2010), Segmentation of X-ray microtomography images of soil using gradient masks, *Computers & Geosciences*, 36(10), 1246-1251.

Schnaar, G. (2006), Pore-Scale Characterization of Organic Immiscible Liquid in Natural Porous Media Using Synchrotron X-ray Microtomography, edited, p. 208 leaves, University of Arizona, Tucson, Arizona.

Schnaar, G., and M. L. Brusseau (2005), Pore-scale characterization of organic immiscible-liquid morphology in natural porous media using synchrotron X-ray microtomography, *Environmental Science & Technology*, 39(21), 8403-8410.

Schnaar, G., and M. L. Brusseau (2006a), Characterizing pore-scale configuration of organic immiscible liquid in multiphase systems with synchrotron X-ray microtomography, *Vadose Zone Journal*, 5(2), 641-648.

Schnaar, G., and M. L. Brusseau (2006b), Characterizing pore-scale dissolution of organic immiscible liquid in natural porous media using synchrotron X-ray microtomography, *Environmental Science & Technology*, 40(21), 6622-6629.

Sheppard, A. P., R. M. Sok, and H. Averdunk (2004), Techniques for image enhancement and segmentation of tomographic images of porous materials, *Physica a-Statistical Mechanics and Its Applications*, 339(1-2), 145-151.

Taina, I. A., R. J. Heck, and T. R. Elliot (2008), Application of X-ray computed tomography to soil science: A literature review, *Canadian Journal of Soil Science*, 88(1), 1-20.

Tarquis, A. M., R. J. Heck, J. B. Grau, J. Fabregat, M. E. Sanchez, and J. M. Anton (2008), Influence of thresholding in mass and entropy dimension of 3-D soil images, *Nonlinear Processes in Geophysics*, 15(6), 881-891.

Taud, H., R. Martinez-Angeles, J. F. Parrot, and L. Hernandez-Escobedo (2005), Porosity estimation method by X-ray computed tomography, *Journal of Petroleum Science and Engineering*, 47(3-4), 209-217.

Tuller, M., R. Kulkarni, and W. Fink (2013), Segmentation of X-Ray CT Data of Porous Materials: A Review of Global and Locally Adaptive Algorithms, in *Soil–Water–Root Processes: Advances in Tomography and Imaging*, edited by S. H. Anderson and J. W. Hopmans, pp. 157-182, Soil Science Society of America, Madison, WI

Vaz, C. M. P., I. C. de Maria, P. O. Lasso, and M. Tuller (2011), Evaluation of an Advanced Benchtop Micro-Computed Tomography System for Quantifying Porosities and Pore-Size Distributions of Two Brazilian Oxisols, *Soil Science Society of America Journal*, 75(3), 832.

Vaz, C. M. P., J. W. Hopmans, A. Macedo, L. H. Bassoi, and D. Wildenschild (2002), Soil water retention measurements using a combined tensiometer-coiled time domain reflectometry probe, *Soil Science Society of America Journal*, 66(6), 1752-1759.

Wang, W., A. N. Kravchenko, A. J. M. Smucker, and M. L. Rivers (2011), Comparison of image segmentation methods in simulated 2D and 3D microtomographic images of soil aggregates, *Geoderma*, 162(3-4), 231-241.

Wildenschild, D., and A. P. Sheppard (2013), X-ray imaging and analysis techniques for quantifying pore-scale structure and processes in subsurface porous medium systems, *Advances in Water Resources*, 51, 217-246.

Wildenschild, D., J. W. Hopmans, C. M. P. Vaz, M. L. Rivers, D. Rikard, and B. S. B. Christensen (2002), Using X-ray computed tomography in hydrology: systems, resolutions, and limitations, *Journal of Hydrology*, 267(3-4), 285-297.

Windreich, G., N. Kiryati, and G. Lohmann (2003), Voxel-based surface area estimation: from theory to practice, *Pattern Recognition*, 36(11), 2531-2541.

TABLES:**Table 1: Porous Medium Characteristics**

	Particle Density (g/cm ³)	*d ₅₀ (mm)	bulk density (g/cm ³)	² U (d ₆₀ /d ₁₀)	¹ n _{grav.}	³ n _{M1}	³ n _{M2}
45-50 Sand	2.64	0.35	1.8	1.1	0.34	0.39	0.35
Glass Beads	2.21	1.00	1.52	1	0.42	0.40	0.41
Vinton	2.59	0.28	1.54	2.4	0.41	0.39	0.36

* d₅₀=mean particle diameter

¹gravimetric porosity (*n*) from bulk density of sample

²U_a= uniformity coefficient, d_i is the percentage of grains smaller than a given sieve size.

³ CT-based porosity (*n*), calculated for each method.

Table 2: Comparison of porosity, maximum A_{aw} , and specific solid surface area

	¹ SSA _{M1}	¹ SSA _M	² A _{max, M1}	² A _{max, M2}	³ GSSA _{M1}	³ GSSA _{M2}	N ₂ BET
	(cm ⁻¹)	(cm ⁻¹)	(cm ⁻¹)	(cm ⁻¹)	(cm ⁻¹)	(cm ⁻¹)	(cm ⁻¹)
45-50	105±2	109±2	102±11	115±9	112±0.01	111±0.01	1333
GB	33.8 ±1	64.5±6	29.3±1	38.6±3	30.5 ±0.01	31.0 ±0.01	27.7
Vinton	190±8	223±8	144±13	170±13	131±0.02	137±0.02	5500

¹ Solid Surface area obtained directly from image analysis normalized by imaged volume.

² Maximum *measurable* specific interfacial area, $A_{max}=A_{aw}(1-S_w)$, ± indicates upper and lower 95% confidence interval.

³ Geometric specific solid surface area based on smooth-sphere assumption, $(=6(1-n)/d_{50})$, where d_{50} is mean particle diameter).

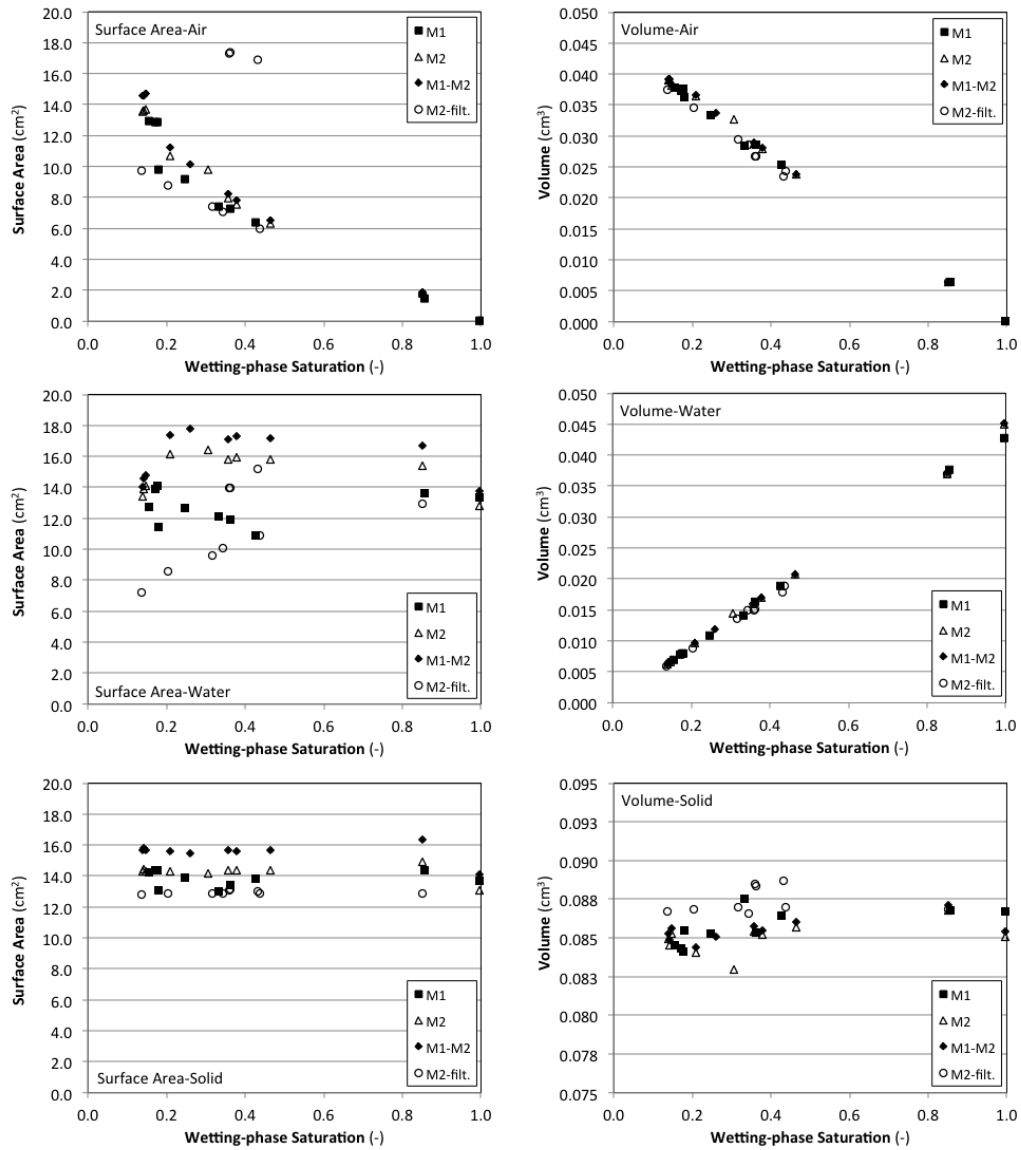


Figure 1: Volume (right) and Surface Area (left) of Air, Water, and Solids per wetting-phase saturation (S_w) for 45-50 sand. M2-filt. is the data set using M2 with noise-reducing pre-processing filters.

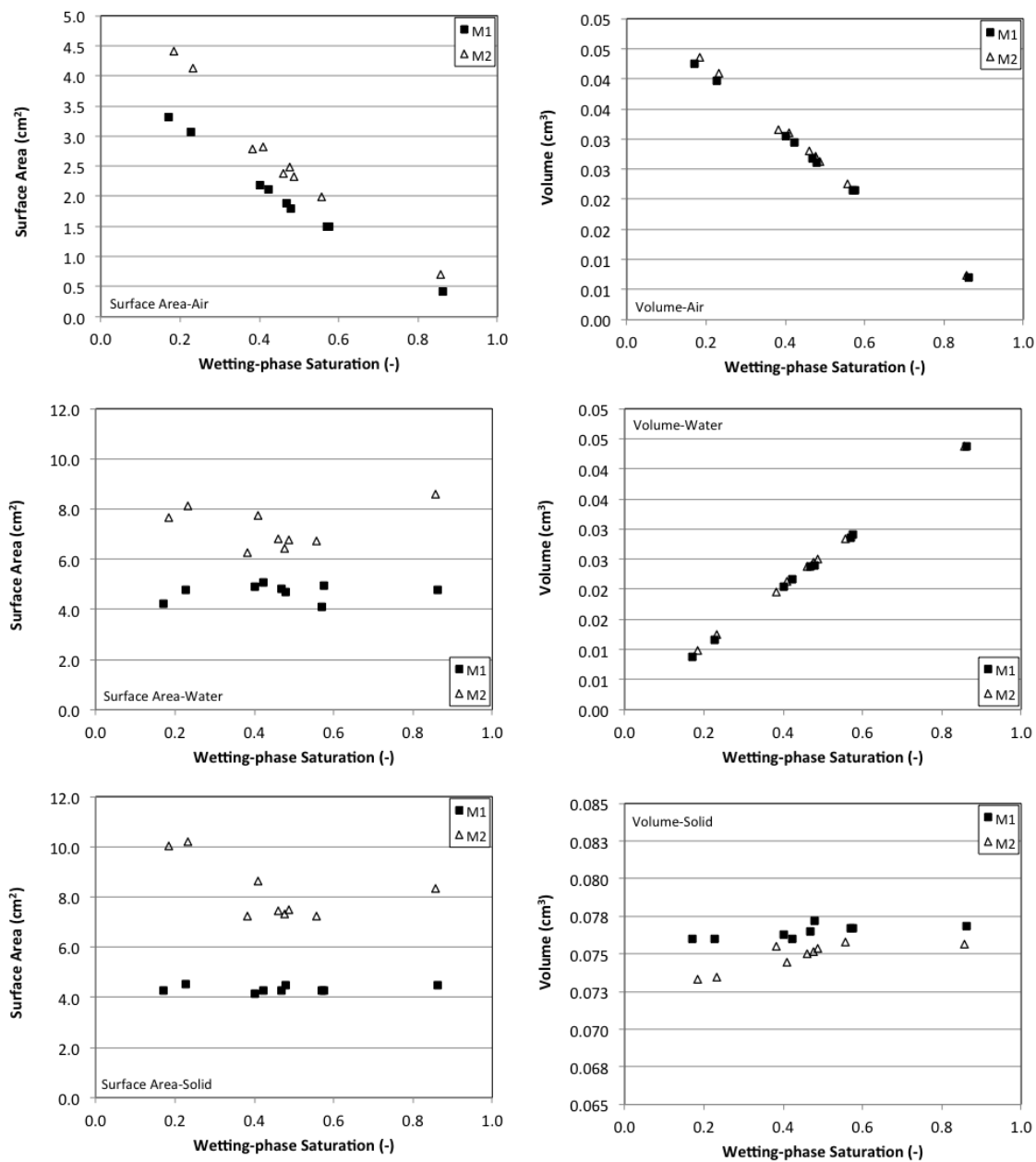


Figure 2: Volume (right) and Surface Area (left) of Air, Water and Solids per wetting-phase saturation for Glass Beads.

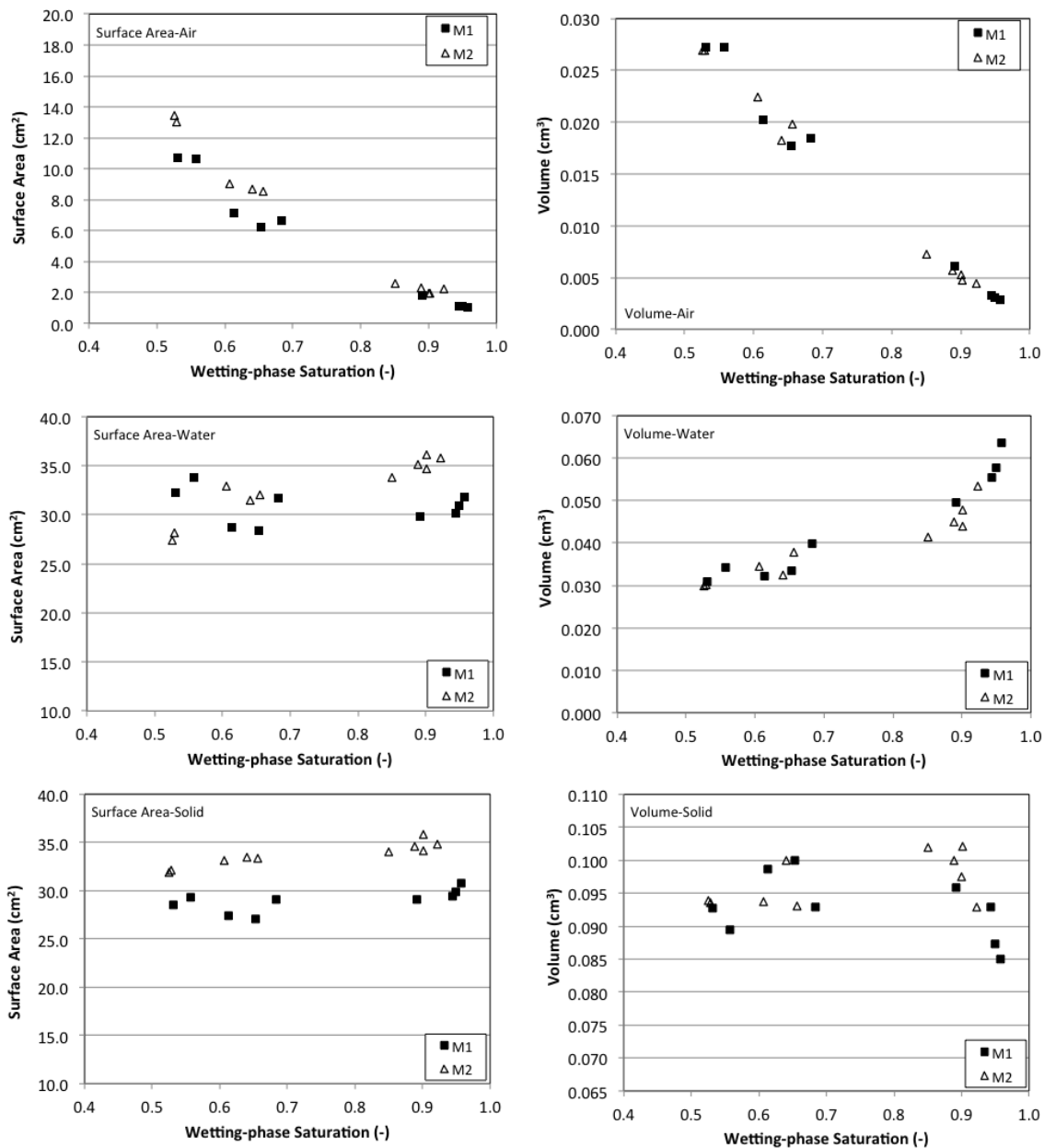


Figure 3: Volume (right) and Surface Area (left) of Air, Water and Solids per wetting-phase Saturation (S_w) for Vinton sand.

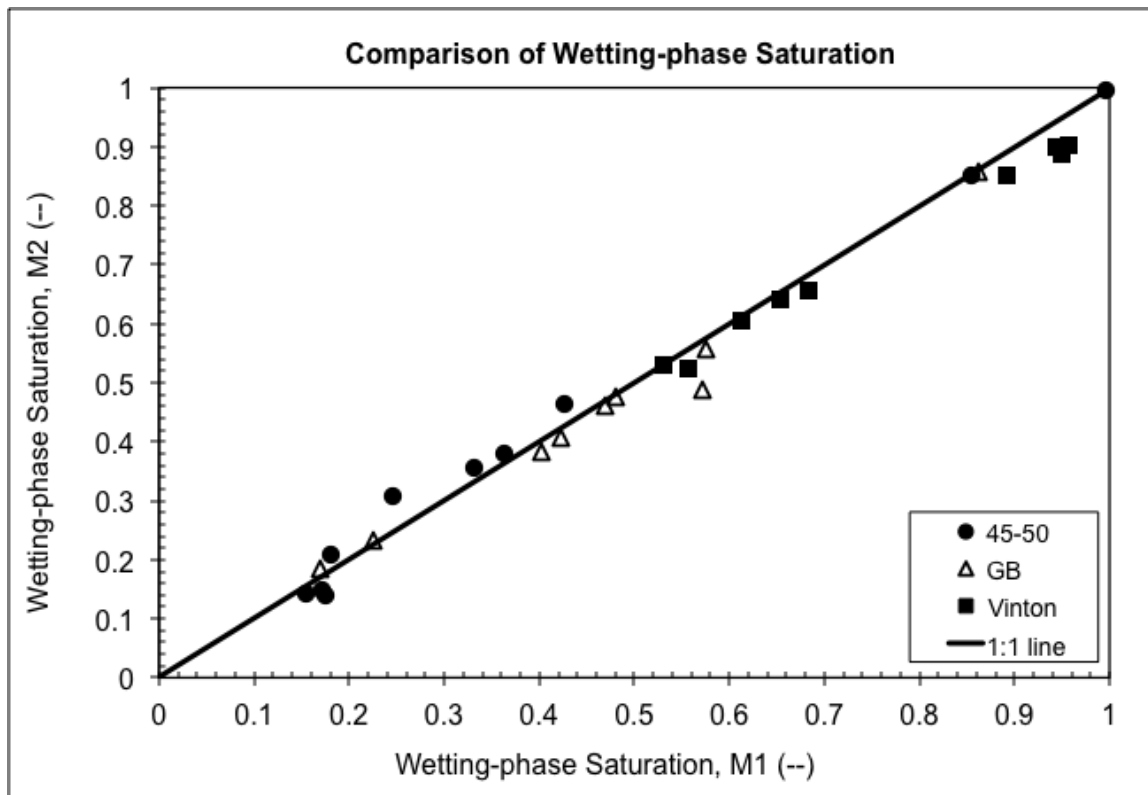


Figure 4: Comparison between saturation using M1 and M2 for various porous media. Wetting-phase saturations (S_w) obtained from water-volume directly from segmentation.

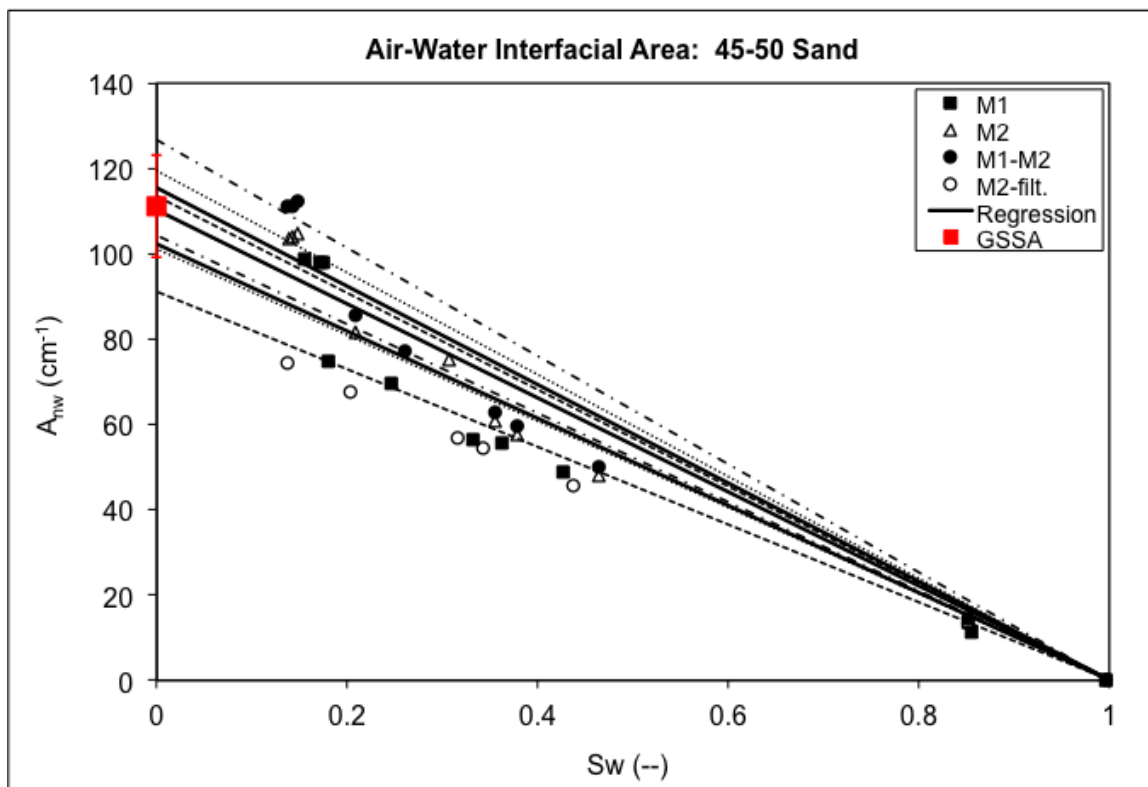


Figure 5: Comparison of Total (A_{aw}) air-water interfacial area between Method 1 (ISSP) and Method 2 (PMIA) for 45/50 sand. M1-M2 is a hybrid, uses images that were segmented using method 2 with the data calculated using method 1. M2-filt. is the independently analyzed data set using M2 with noise-reducing pre-processing filters. GSSA is geometric specific solid surface area.

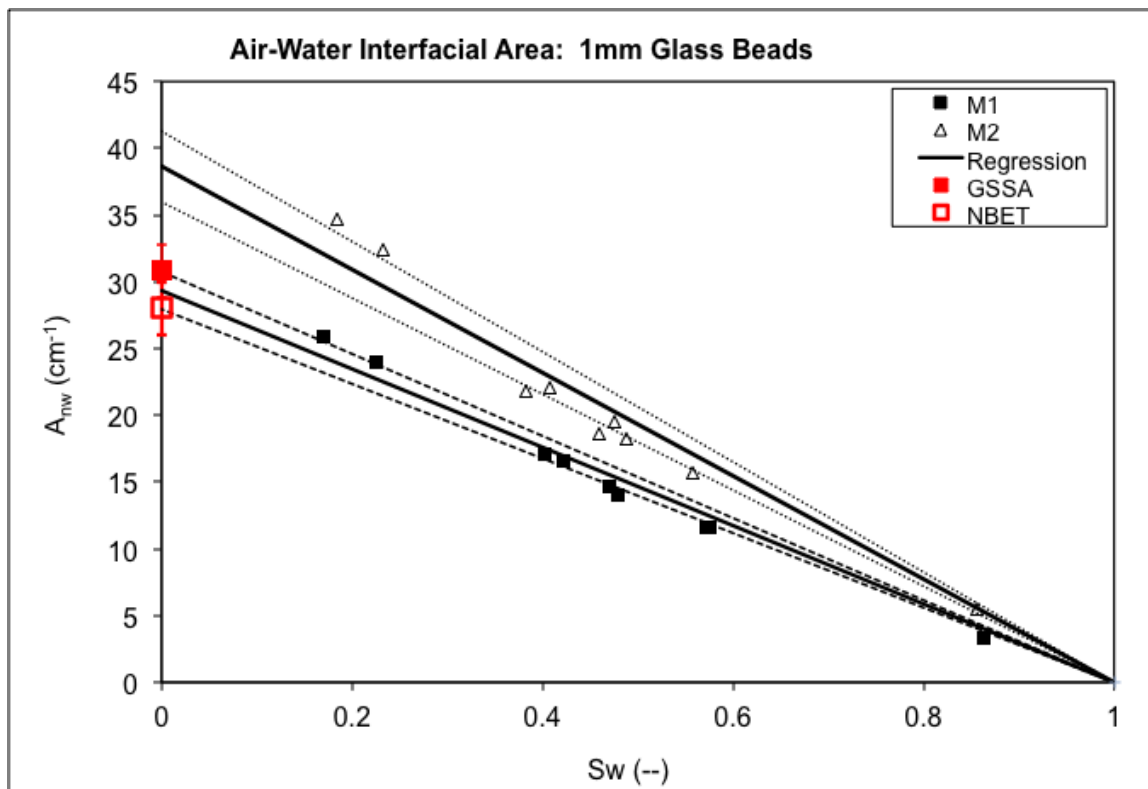


Figure 6: Comparison of A_{aw} between Method 1 (ISSP) and Method 2 (PMIA) for Glass beads. GSSA is geometric specific solid surface area.

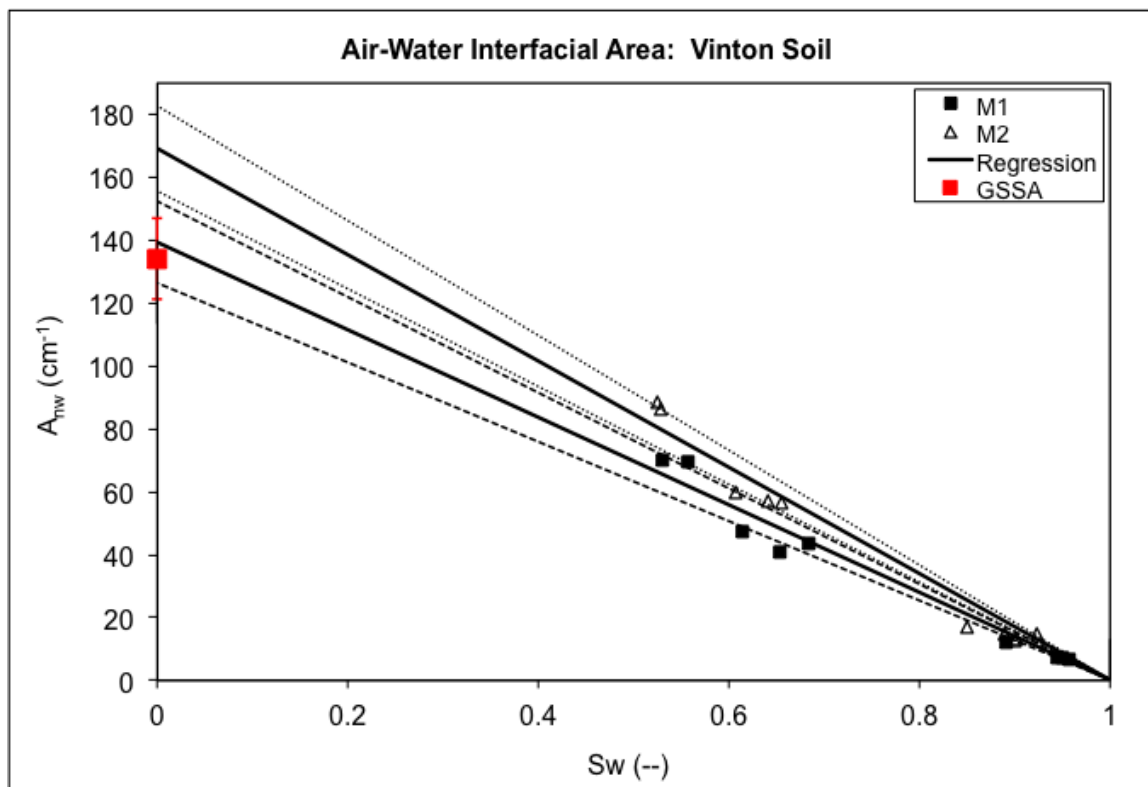


Figure 7: Comparison of A_{aw} between Method 1 (ISSP) and Method 2 (PMIA) for Vinton sand. GSSA is geometric specific solid surface area.

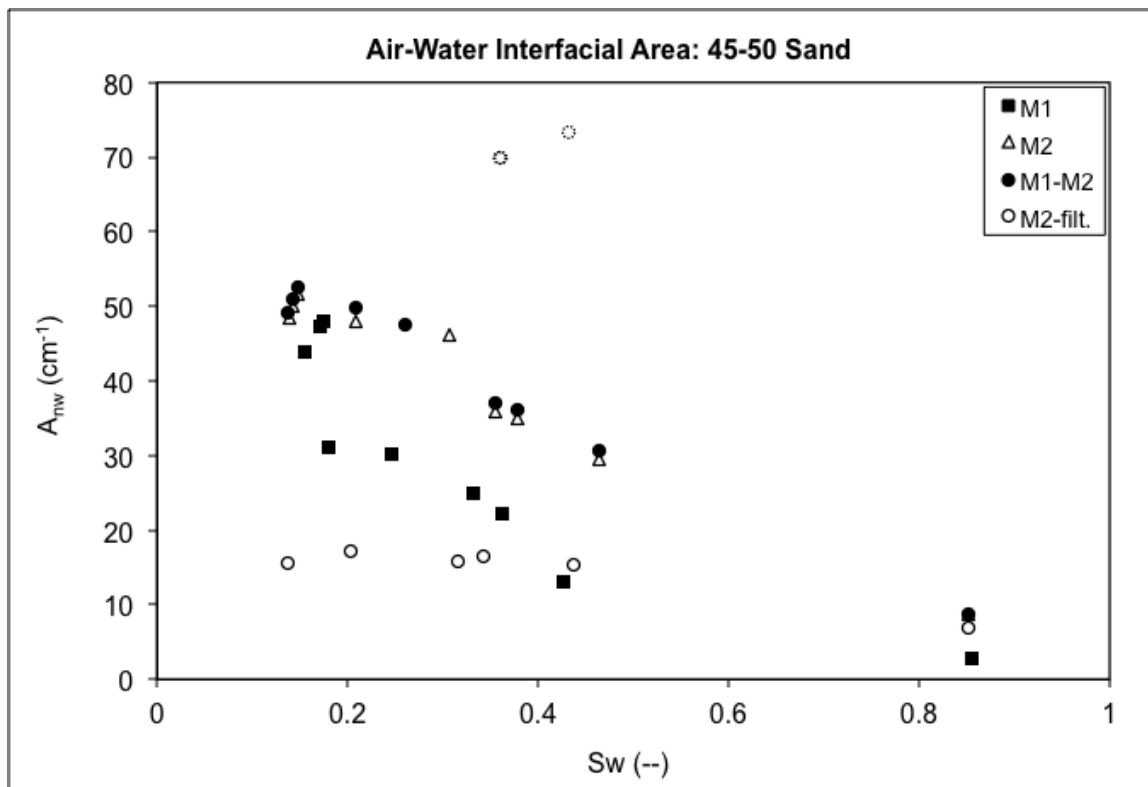


Figure 8: Comparison of *Capillary* (C_{aw}) air-water interfacial area between Method 1 (ISSP) and Method 2 (PMIA) for 45/50 sand. M1-M2 is a hybrid, uses images that were segmented using method 2 with the data calculated using method 1. M2-filt. is the independently analyzed data set using M2 with noise-reducing pre-processing filters. Dashed open circles represent outliers.

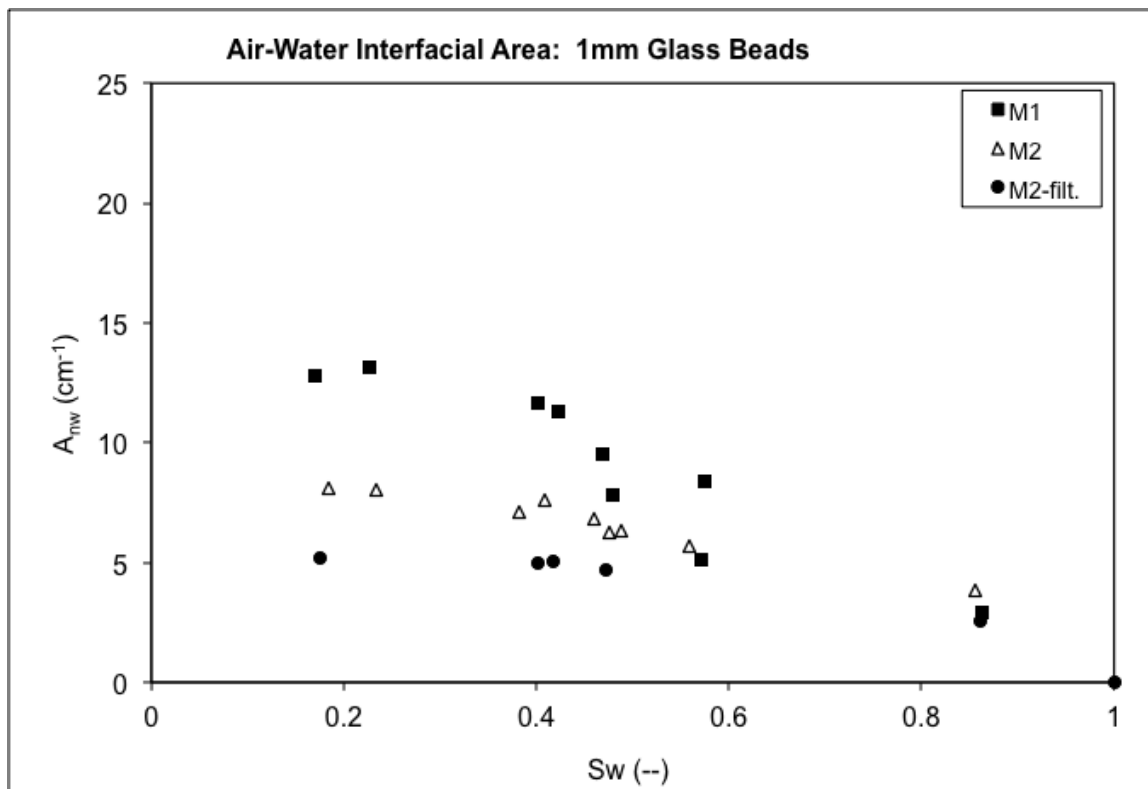


Figure 9: Comparison of C_{aw} between Method 1 (ISSP), Method 2 (PMIA) for Glass beads, and Method 2 with the application of noise-reducing filters.

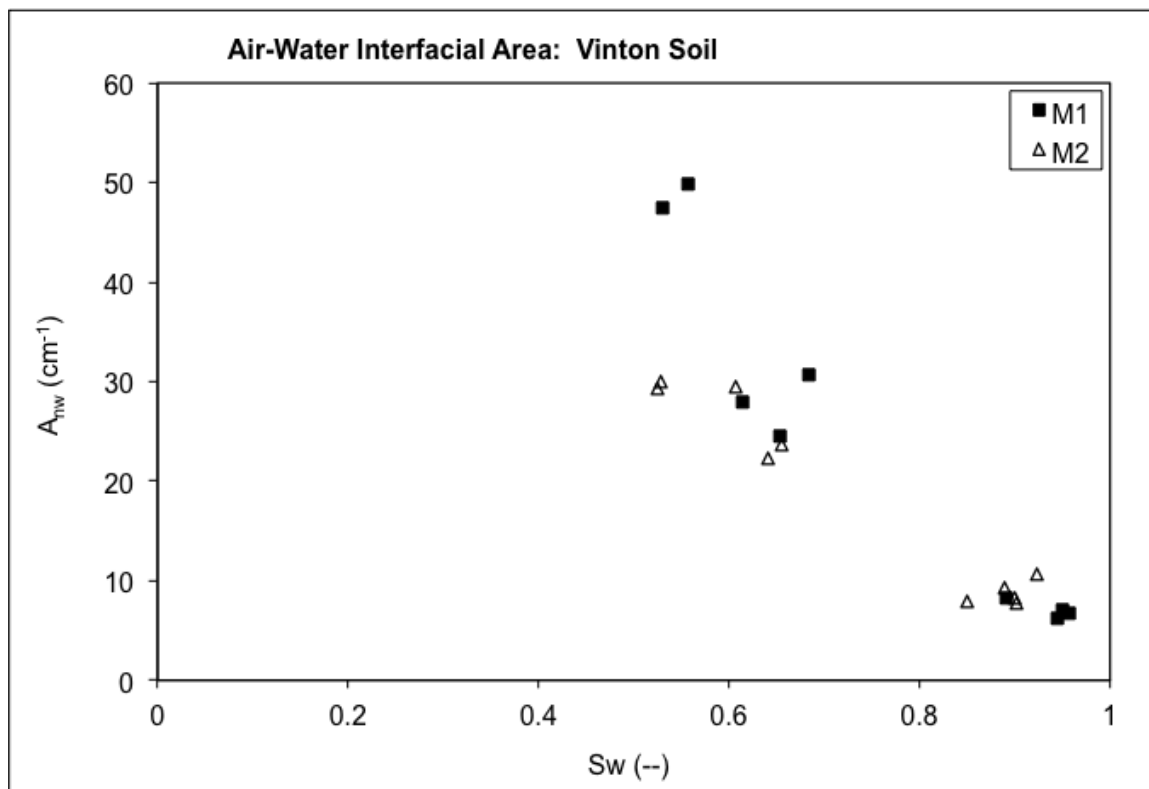


Figure 10: Comparison of C_{aw} between Method 1 (ISSP) and Method 2 (PMIA) for Vinton sand.

APPENDIX B

SEQUENTIAL IMAGE SEGMENTATION APPROACH FOR DETERMINING TOTAL AND CAPILLARY AIR-WATER INTERFACIAL AREAS IN NATURAL POROUS MEDIA

1. Background

The work presented in Appendix A evaluates results obtained using two different approaches, and their suitability for reliably estimating total (A_{aw}) and capillary (C_{aw}) air-water interfacial areas for natural porous media. The primary objective was to test different threshold methods for identifying each phase of interest from a grey-scale X-ray microtomography image.

Preceding the availability of a simultaneous multi-phase segmentation method (Method 2 in Appendix A), sequential independent analysis (Method 1) was used for segmentation of tomographic images. Volumes and surface areas were subsequently extracted for calculation of interfacial areas. When analysis of tomographic image was performed using independent single-phase analysis (SP) (i.e., each phase was processed independently), a main concern is the possible lack of mass balance resulting from individual analysis of all three phases. In other words, there is potential for two (or three) phases to overlap after segmentation and phase-separation because the phases are processed individually. Also, blurriness and noise in the images can also lead to greyscale overlap, thus confusing identification near the boundaries (e.g., Brown et al. 2014). The capillary interfacial area is calculated from the geometrical conceptualization of fluid configuration in the porous media (e.g. Montemagno and Ma, 1997; Dalla et al., 2002). Based on this model all phases in the system, (air, water, and solid) need to be identified.

The robustness of the segmentation procedure will help to establish overall coherency between phases in a unit volume, essential to the determination of capillary interfacial areas.

The objectivity of simplistic segmentation methods is commonly questioned in the search for advanced segmentation methods (e.g. Wang et al., 2011; Kulkarni et al., 2012). Due to the lack of independent parameters in which to benchmark segmentation results (e.g. Wang et al., 2011), it became evident that it was crucial to ground the results to independently measured parameters. In this study, the several stages of Method 1 (ISSP) sequential segmentation of air, water, and solid phases is evaluated. Porosity was used as a measure to evaluate the representativeness of the method for the air-water systems investigated. The robustness of estimated total and capillary air-water interfacial areas is discussed, and the air-solid combination approach is shown for Vinton and 45-50 Accusand.

2. Materials and Methods Overview

Synchrotron X-ray microtomography images were used to measure air-water interfacial area for 45-50 ($d_{50}= 0.35$; bulk density= 1.8 g/cm^3 ; $U=1.1$) and Vinton sands ($d_{50}= 0.41$; bulk density= 1.54 g/cm^3 ; $U=2.4$) as a function of water-phase saturation (S_w). Experimental details pertaining to sample preparation and drainage procedure are discussed in Appendix A.

2.1 Data Collection

X-ray microtomography images were collected at the GeoSoilEnviroCARS (GSECARS) BMD-13 beamline at the Advanced Photon Source, Argonne National Laboratory, IL. The effective resolution for our experiments is $\sim 10 \mu\text{m}$. The field of view encapsulating the porous media is approximately 5 mm. The images were collected from the centers of the columns, to minimize the potential influence of end effects. Sequential images of the columns were collected above and below the iodine edge, at 33.269 KeV and 33.069 KeV. The above-edge image (A-image) is used to enhance the liquid phase, and below-the-edge image (B-image) is used to distinguish the solid phase (e.g. Wildenschild et al., 2002); Schnaar and Brusseau, 2006b; Costanza-Robinson et al., 2008). The images were pre-processed using GSECARS-developed software (Rivers et al., 2010; Rivers 2012). Further details regarding the image acquisition and procedure are described in Appendix A.

2.2 Quantitative Data Processing and Analysis

This procedure is based on a global threshold selection approach for the entire image (ASTM, 1992), and independent sequential phase processing. The quantitative image analysis is achieved using BlobD, a software package designed for processing large three-dimensional data sets obtained by computed tomography. It extracts information within the data volume, such as number of blobs, surface area, and volume (e.g. Ketcham 2005, Blob3D manual). Details on how Blob3D handles each step can be found in Ketcham (2005). Due to its ease of use, and efficiency in handling large, several

megabytes of data, several scientists, have used it to quantify interfacial areas, e.g. Costanza-Robinson et al., 2008; Schnaar and Brusseau, 2005; Schnaar and Brusseau 2006a; Schnaar and Brusseau 2006b; Brusseau et al., 2007; Brusseau et al., 2008; and Narter 2012).

ImageJ (NIH, (Rasband), 1997-2012) was used to crop a circular area to remove the column wall, with a diameter that encompasses a large portion of the sample, while maintaining a reasonable representative volume, REV. The cropped slices were used as the input volume for further processing. Blob3D offers the possibility of several filters to improve and minimize noise in the greyscale image. The median smoothing filter was used to suppress the noise inherent in the original images (e.g. Schnaar 2006; Narter and Brusseau, 2010). Median smoothing filter reduces noise by assigning a voxel with the median greyscale values from closely surrounding greyscale values, with minimal alteration to phase geometry (e.g. Blob3D user manual, Brusseau et al. 2006; Brusseau et al, 2008; Brusseau et al., 2009). It also helps to avoid the creation of pixelation artifacts around the solid grains, which can erroneously increase the calculated surface area (e.g. Costanza-Robinson et al., 2008).

Blob3D provides the user with several options for establishing a grey-scale value for the component of interest. The global threshold was chosen. This approach uses a select subset of images from which to determine the grey-scale of the voxels of the phase of interest. The value is set to fall at the midpoint value between the values of the target phase and other phase in the array (e.g. ASTM 1992; Schnaar and Brusseau 2005; Schnaar and Brusseau 2006a; Schnaar and Brusseau 2006b; Peng et al., 2012). When the

phase of interest is air, the grey-scale value is measured for multiple random sections of clearly discernible air and solid phases. This approach relies solely on the grey-level information, and does not account for spatial variability within the sample.

Once the threshold value has been set, the image segmentation is initiated. The user must then choose to automatically separate all components, or individually accept each blob. The later offers many tools for the user to inspect each blob and decide how the program should handle it. Manual separation is cumbersome and likely to introduce a degree of user bias to segmentation, and in highly heterogeneous media such as Vinton sand. Thus, automatic separation of all components was chosen to minimize user.

The governing principle for Method 1 is to use the best image to represent a particular phase, and is developed with the goal for analysis of natural complex porous media. There are three approaches in the evolution of Method 1 discussed below.

2.3 Independent Single-Phase Processing, (SP)

Both above-the-edge and below-the-edge data are used (Figure 1). For the above-the-edge (A-image) set, the doped-water phase is bright and has marked contrast with air while the solids are blurred. For the below-the-edge (B-images), the solids are in high contrast from the water phase, while the water is faintly distinguishable from air. The A-image is used for analysis of the air, the B-image set is used for solid-phase analysis, and the subtracted image is used to analyze the water phase (Figure 1). The segmented data obtained for each phase is completely independent as the software segments it

individually. The wetting-phase saturation and porosity are calculated using the extracted surface areas and volumes of each phase directly from segmentation software.

2.4 Sequential Single-phase Processing, (SSP)

Determining capillary interfacial area requires characterization of surface areas and volumes for all three phases. It was noticeable that the combined image data compiled from independent analysis (SP) of each phase often contained instances of phase overlap (more than one phase occupying the same voxel). This was observed (data not shown) when wetting-phase saturation (S_w) determined from the air volume ($S_w=1-S_n$) was not compared to S_w determined using the water volume. This similarity was based on mean square error (<0.0001).

The SP method was modified wherein several segmentation iterations are conducted to reduce phase overlap, and minimize the mean square error as much as possible. This was done for the water phase using the comparison of S_w calculated from the wetting phase volume, and the S_w calculated from the air volume data ($S_{w\ air}=1-S_n$) as the metric. The porosity was also included for independent comparison to independent measured bulk density of the column. In this case, the solid phase was segmented and porosity $((1-V_{solid})/V_{total})$ calculated and assessed against the porosity based on volumes of air and water (V_{voids}/V_{total}).

2.5 Method 1—Integrated Sequential Phase Processing, (ISPP)

This revision was employed to simplify the sequential processing approach. This approach uses the mass-balance continuum concept that the sum of the volumes of all segmented phases should equal the total volume analyzed. Hence, the S_w from air ($1-S_n$) should closely match that obtained directly from water analysis as in (SSP). Likewise, the porosity based on the sum of voids (air and water) was evaluated. It should be equal to the porosity obtained from the solid analysis, $(V_{air} + V_{water} + V_{solids}) = V_{total-total}$.

In this case, the air and solid phases, for which segmentation is generally robust compared to the water phase, are processed independently. Using IDL, the two independently segmented binary image sets are combined as shown in Figure 2, and used as input for another round of segmentation. This time, each phase in the combined image (Figure 2) is represented by a distinct, single grey-scale value, and the images are segmented sequentially (air, solid, water) in Blob3D. When all three phases are segmented from one set of images, the software ensures that pixels attributed to one phase cannot be assigned to another phase (eliminating phase overlap). Schnaar and Brusseau (2006) and Costanza-Robinson et al. (2008) used a similar combination technique, employing independent segmentation of air and water. The air-water combination test is also shown in Figure 2.

3. Method Evaluation

3.1 Sequential Single Phase Assessment: Total Air-Water Interfacial Area (A_{aw})

Figure 3 shows the evolution of method 1 for the total interfacial area, A_{aw} based on single-phase analysis for 45-50 sand, and Figure 4 for Vinton sand. The use of individual sequential segmentation corresponds to differences in water content, but not in the volumes or surface areas of the air phase. The results shown in Appendix A (Figure 6) are comparable to those shown in Figure 3 for the 45-50, albeit having analyzed the air-phase independently. Similar values are observed for A_{aw} even when considering changes in the wetting-phase saturations. These changes are attributed to threshold selection variation present in each permutation of Method 1.

The subsequent sequential approaches (Figure 3) reflect a small change in the REV. The cropping region was selected manually, potentially affecting the overall characterization of fluids, due to selection of different domains (REV). Nominally the differences in cropping diameters (5.64-5.67mm) are considered negligible. However, the location and diameter of the crop region may have been biased to certain fluid configurations and to minimize noise prior to segmentation. For example, noise was observed to increase in the greyscale image near the column walls. In general, the heterogeneity of the grains, in terms of size and distribution, and grain density can contribute to uneven attenuation, leading to noise in the original grey-scale image. Noise can also occur during image acquisition procedure (Baveye et al., 2010; Hapca et al., 2011; Hapca et al., 2013; Houston et al., 2013a; Houston et al., 2013b). Evaluation of Figure 3 shows minimal changes to the total A_{aw} for 45-50 sand. For Vinton soil changes

in cropping diameters of (5.8-6.1mm) also reflected minimal changes in A_{aw} values. Thus confirming the robustness of air-phase segmentation and total A_{aw} results. Moreover, A_{aw} results can be used to validate results using other segmentation approaches as discussed in Appendix A. Interestingly, small differences in resulting water saturation are observed, and is speculated to affect the calculation of capillary interfacial areas.

It is important to compare results to independently measured metrics. For the evaluation of total (measurable) interfacial area, (A_{aw}), the maximum interfacial area (A_{max}) is used. This value is an index for a given system, effectively a measure of a theoretical maximum interfacial area in a system (Brusseau et al., 2009; Narter and Brusseau 2010) for a given technique. The A_{max} is estimated based on the linear regression from the relationship between A_{aw} and S_w . The average A_{max} for all 45-50 sand permutations (Figure 3) is 101 cm^{-1} . These values are in range of results reported in the literature. For 45-50 sand the A_{max} is $92 \pm 12 \text{ cm}^{-1}$.

Tomography results are not influenced by microscopic surface roughness (e.g. Schnaar and Brusseau, 2005; Brusseau et al, 2006; Brusseau et al., 2007; Brusseau et al., 2009; Brusseau et al., 2010). Thus, A_{max} values can also be compared to the independent calculation based on geometric smooth sphere assumption ($GSSA=6(1-n)/d_{50}$, where n is porosity, and d_{50} is mean particle diameter). The GSSA for 45-50 is 112 cm^{-1} .

The maximum air-water interfacial area is associated with the assumption of an infinitesimally thin layer of water solvating the solid surface. Under such conditions, it is anticipated that the corresponding maximum interfacial area is also comparable to the

solid surface area. For 45-50 sand the specific solid surface area (SSA) measured is 105 cm^{-1} corresponding to ISSP sample 1d in Figure 3.

Similar analysis was conducted on Vinton sand sample (Figure 4). The average estimated A_{max} is 144 cm^{-1} . The SSA value is $184\text{-}190 \text{ cm}^{-1}$ corresponding to ISSP samples (1d and 1e respectively) in Figure 4. These results are comparable to reported A_{max} values ($142\text{-}149 \text{ cm}^{-1}$) by (Brusseau et al., 2007; Brusseau et al., 2010). The calculated GSSA is 131 cm^{-1} for Vinton sand similar to values reported elsewhere (e.g. Brusseau et al., 2009; Brusseau et al., 2010).

3.2 Sequential Single Phase Assessment: Capillary Air-Water Interfacial Area (C_{aw})

Additional data processing was conducted to determine capillary interfacial area. Figure 5 shows the evolution of method 1 for the capillary-associated interfacial area, C_{aw} for the 45-50 sand. The $C_{\text{aw}}\text{-}S_{\text{w}}$ function (Figure 5) shows that the C_{aw} reaches a maximum and then decreases with increased drainage. The differences of water phase saturation shown by the evolution of method 1 in Figure 5 correspond to changes in capillary-associated interfacial area C_{aw} . The profiles exhibited by the $C_{\text{aw}}\text{-}S_{\text{w}}$ functions in Figure 5 resembles the expected behavior for C_{aw} , wherein the area first increases during drainage and then decreases at lower saturations (e.g., Reeves and Celia 1999; Dalla et al. 2002; Culligan et al., 2004; Culligan et al., 2006; Brusseau et al., 2007; Porter et al., 2009; Schaap and Tuller 2010).

Figure 6 shows the capillary-associated interfacial area for Vinton sand. Here differences in capillary interfacial area calculations are very small compared to the 45-50

sand. For Vinton sand, the lack of low S_w data precludes evaluation in terms capillary behavior at lower saturations (<65%). The variations in REV (5.8-6.1mm) for this soil also correspond to changes in water saturation.

The specific capillary interfacial area (C_{aw}) was calculated from a conceptual model based on a simple phase-balance analysis of surface areas and interfacial contacts in a three-phase (solid, wetting fluid, non-wetting fluid) porous medium system. Determination of capillary interfacial area thus requires characterization of all phases present (Montemagno and Ma 1999; Dalla et al., 2002). The C_{aw} model excludes the presence of film to comply with the tomographic reality, thus representing only the interfaces associated with the menisci of contacts between air and “bulk” water. The solid-water contacts are speculated to significantly affect the contrast at the boundaries, complicating the segmentation of water phase at the boundaries with solid grains.

The water phase is more sensitive to the challenges associated with image processing due to the presence of solid-water contact surfaces. The sample resolution (~10 microns) is not sufficient to resolve water films known to coat the solid grains. The perceived changes in fluid configuration due to resolution can also impact the overall calculated capillary behavior (Appendix A). Accordingly the sequential segmentation approach evolved to help increase the reliability of results obtained from water phase segmentation. The independent metrics used to ground truth results from solid phase analysis were used to establish reliability of air-phase results.

3.3 Porosity and Wetting-phase Saturation (S_w)

Figure 7 illustrates the relationship between porosities obtained from fluid volumes vs. porosities from solid-phase volumes. The correlation between water saturations (S_w) obtained from volume of voids and solid-phase porosities are also illustrated. Results show that the volume of voids estimated from image analysis of the solid phase is very similar to the volume of voids estimated from analysis of air and water phases. Likewise, the water saturation obtained directly from the water phase analysis is comparable to the saturation obtained from the air-phase analysis ($S_w=1-S_n$). These results suggest that a reasonable mass balance was achieved and phase overlap were minimized using the combination approach (air and solid).

At first, the subtraction method appeared attractive for water phase segmentation. It was observed however, that the SP segmentation approach contributed to differences in S_w obtained from each phase, and phase overlap. This was attributed to difficulties in segmenting the water phase. Others in the literature have described segmenting the air and water phase separately (Costanza-Robinson et al., 2008; Schnaar and Brusseau 2006a). In their work, they combined their respective binary representations of air and water into one binary image, for final calculations. The new combined image resulted in the solid phase being implicitly defined. The sequential combination approach (ISSP) used in M1 was chosen due to the uncertainty in measuring the water phase independently, and the overarching interest in the capillary interfacial area calculation. This method also circumvents the assumption that greyscale values are distinct between

two classes of materials. A common assumption of global thresholding methods (e.g. Baveye et al., 2013; Houston et al., 2013a).

4. Summary

The total interfacial area (A_{aw}) results based on the integrated sequential approach (Method 1) were not affected small changes in threshold, cropping regions, or the combination of pre-segmented individual phases. This was attributed to the clear resolution of the air phase in X-ray tomography images. The air is illustrated as the darkest phase in both dual-energy scans (after reconstruction), as it does not absorb X-rays. As a result, air blobs are depicted with reasonably homogenous attenuation coefficients (Werth et al., 2010).

The suitability of each segmentation method for estimating C_{aw} is contingent upon scrutiny of the total A_{aw} , the specific solid surface area (SSA), porosity, and segmented volumes. Tomography measurements are not inclusive of surface roughness due to resolution limitations (e.g. Schnaar and Brusseau 2005; Brusseau et al., 2006; Brusseau et al., 2007; Brusseau et al., 2009; Brusseau et al., 2010). The A_{max} is associated with the assumption of an infinitesimally thin layer of water solvating the solid surface. Thus, allowing for comparison to GSSA values, and is expected to be comparable to specific solid surface areas. Combining the air and solid phases provides more robust data compared to other combinations due to the independent metrics used to ground truth results from solid phase analysis. For example, the porosities obtained from analysis of the solid phase (both separately and as combined data) are similar to the independently

determined gravimetric porosities. Also, the specific solid surface areas are comparable to the calculated theoretical GSSA values. Similar to the air phase analysis, segmentation of the solid phase is not as sensitive to threshold variations. Unfortunately, there is no direct independent parameter to ground truth results for the water phase, and thus to quantify the capillary interfacial area C_{aw} . The integration of two robust individually segmented phases (air and solid) in this approach was shown to minimize phase overlap and provides more consistent determination of the wetting phase (water). Overall, this approach may help highlight possible spatial variability of water phase at the pore scale.

5. References

ASTM (American Society for Testing and Materials), (1992). Standard guide for computed tomography (CT) imaging, ASTM designation E 1441–92a, in 1992 annual book of ASTM standards, section 3 metals test methods and analytical procedures: Philadelphia, ASTM, pp. 690–713.

Baveye, P. C., et al. (2010), Observer-dependent variability of the thresholding step in the quantitative analysis of soil images and X-ray microtomography data, *Geoderma*, 157(1-2), 51-63.

Brown, K., S. Schluter, A. Sheppard, and D. Wildenschild (2014), On the challenges of measuring interfacial characteristics of three-phase fluid flow with x-ray microtomography, *Journal of Microscopy*, 253(3), 171-182.

Brusseau, M. L., S. Peng, G. Schnaar, and M. S. Costanza-Robinson (2006), Relationships among air-water interfacial area, capillary pressure, and water saturation for a sandy porous medium, *Water Resources Research*, 42(3).

Brusseau, M. L., S. Peng, G. Schnaar, and A. Murao (2007), Measuring air-water interfacial areas with X-ray microtomography and interfacial partitioning tracer tests, *Environmental Science & Technology*, 41(6), 1956-1961.

Brusseau, M. L., H. Janousek, A. Murao, and G. Schnaar (2008), Synchrotron X-ray microtomography and interfacial partitioning tracer test measurements of NAPL-water interfacial areas, *Water Resources Research*, 44(1).

Brusseau, M. L., M. Narter, S. Schnaar, and J. Marble (2009), Measurement and Estimation of Organic-Liquid/Water Interfacial Areas for Several Natural Porous Media, *Environmental Science & Technology*, 43(10), 3619-3625.

Brusseau, M. L., M. Narter, and H. Janousek (2010), Interfacial Partitioning Tracer Test Measurements of Organic-Liquid/Water Interfacial Areas: Application to Soils and the Influence of Surface Roughness, *Environmental Science & Technology*, 44(19), 7596-7600.

Costanza-Robinson, M. S., K. H. Harrold, and R. M. Lieb-Lappen (2008), X-ray microtomography determination of air-water interfacial area-water saturation relationships in sandy porous media, *Environmental Science & Technology*, 42(8), 2949-2956.

Culligan, K. A., D. Wildenschild, B. S. B. Christensen, W. G. Gray, M. L. Rivers, and A. F. B. Tompson (2004), Interfacial area measurements for unsaturated flow through a porous medium, *Water Resources Research*, 40(12), n/a-n/a.

Culligan, K. A., D. Wildenschild, B. S. B. Christensen, W. G. Gray, and M. L. Rivers (2006), Pore-scale characteristics of multiphase flow in porous media: A comparison of air-water and oil-water experiments, *Advances in Water Resources*, 29(2), 227-238.

Dalla, E., M. Hilpert, and C. T. Miller (2002), Computation of the interfacial area for two-fluid porous medium systems, *Journal of Contaminant Hydrology*, 56(1-2), 25-48.

Hapca, S. M., A. N. Houston, W. Otten, and P. C. Baveye (2013), New Local Thresholding Method for Soil Images by Minimizing Grayscale Intra-Class Variance, *Vadose Zone Journal*, 0(0), 0.

Hapca, S. M., Z. X. Wang, W. Otten, C. Wilson, and P. C. Baveye (2011), Automated statistical method to align 2D chemical maps with 3D X-ray computed microtomographic images of soils, *Geoderma*, 164(3-4), 146-154.

Houston, A. N., W. Otten, P. C. Baveye, and S. Hapca (2013a), Adaptive-window indicator kriging: A thresholding method for computed tomography images of porous media, *Computers & Geosciences*, 54, 239-248.

Houston, A. N., S. Schmidt, A. M. Tarquis, W. Otten, P. C. Baveye, and S. M. Hapca (2013b), Effect of scanning and image reconstruction settings in X-ray computed microtomography on quality and segmentation of 3D soil images, *Geoderma*, 207-208, 154-165.

Ketcham, R. A. (2005), Computational methods for quantitative analysis of three-dimensional features in geological specimens, *Geosphere*, 1(1), 32.

Kulkarni, R., M. Tuller, W. Fink, and D. Wildenschild (2012), Three-Dimensional Multiphase Segmentation of X-Ray CT Data of Porous Materials Using a Bayesian Markov Random Field Framework, *Vadose Zone Journal*, 11(1).

Montemagno, C. D., and Y. Ma (1999), Measurement of Interfacial Surface Area for Two-Phase Flow in Porous Media from PVI Data, in *Characterization and measurement of the hydraulic properties of unsaturated porous media: proceedings of the International Workshop on Characterization and Measurement of the Hydraulic Properties of Unsaturated Porous Media: Riverside, California, October 22-24, 1997*, edited by M. T. van Genuchten, F. J. Leij and L. Wu, pp. 121-132, U.S. Salinity Laboratory, Agricultural Research Service Dept. of Environmental Sciences, University of California, Riverside, CA.

Narter, M., and M. L. Brusseau (2010), Comparison of interfacial partitioning tracer test and high-resolution microtomography measurements of fluid-fluid interfacial areas for an ideal porous medium, *Water Resources Research*, 46.

Narter, M. (2012), Characterizing Non-Wetting Fluid in Natural Porous Media Using Synchrotron X-Ray Microtomography, edited, p. 172 leaves, University of Arizona, University of Arizona.

Peng, S., Q. H. Hu, S. Dultz, and M. Zhang (2012), Using X-ray computed tomography in pore structure characterization for a Berea sandstone: Resolution effect, *Journal of Hydrology*, 472, 254-261.

Porter, M. L., M. G. Schaap, and D. Wildenschild (2009), Lattice-Boltzmann simulations of the capillary pressure-saturation-interfacial area relationship for porous media, *Advances in Water Resources*, 32(11), 1632-1640.

Porter, M. L., D. Wildenschild, G. Grant, and J. I. Gerhard (2010), Measurement and prediction of the relationship between capillary pressure, saturation, and interfacial area in a NAPL-water-glass bead system, *Water Resources Research*, 46(8).

Rivers, M. L. (2012), tomoRecon: High-speed tomography reconstruction on workstations using multi-threading, *Proc Spie*, 8506.

Rivers, M. L., D. T. Citron, and Y. B. Wang (2010), Recent developments in computed tomography at GSECARS, *Proc Spie*, 7804.

Schaap, M. G., and M. Tuller (2010), Quantitative Pore-Scale Investigations of Multiphase Bio/Geo/Chemical Processes, *Vadose Zone Journal*, 9(3), 573-575.

Schnaar, G. (2006), Pore-Scale Characterization of Organic Immiscible Liquid in Natural Porous Media Using Synchrotron X-ray Microtomography, edited, p. 208 leaves, University of Arizona, Tucson, Arizona.

Schnaar, G., and M. L. Brusseau (2005), Pore-scale characterization of organic immiscible-liquid morphology in natural porous media using synchrotron X-ray microtomography, *Environmental Science & Technology*, 39(21), 8403-8410.

Schnaar, G., and M. L. Brusseau (2006a), Characterizing pore-scale dissolution of organic immiscible liquid in natural porous media using synchrotron X-ray microtomography, *Environmental Science & Technology*, 40(21), 6622-6629.

Schnaar, G., and M. L. Brusseau (2006b), Characterizing pore-scale configuration of organic immiscible liquid in multiphase systems with synchrotron X-ray microtomography, *Vadose Zone Journal*, 5(2), 641-648.

Wang, W., A. N. Kravchenko, A. J. M. Smucker, and M. L. Rivers (2011), Comparison of image segmentation methods in simulated 2D and 3D microtomographic images of soil aggregates, *Geoderma*, 162(3-4), 231-241.

Wildenschild, D., J. W. Hopmans, C. M. P. Vaz, M. L. Rivers, D. Rikard, and B. S. B. Christensen (2002), Using X-ray computed tomography in hydrology: systems, resolutions, and limitations, *Journal of Hydrology*, 267(3-4), 285-297.

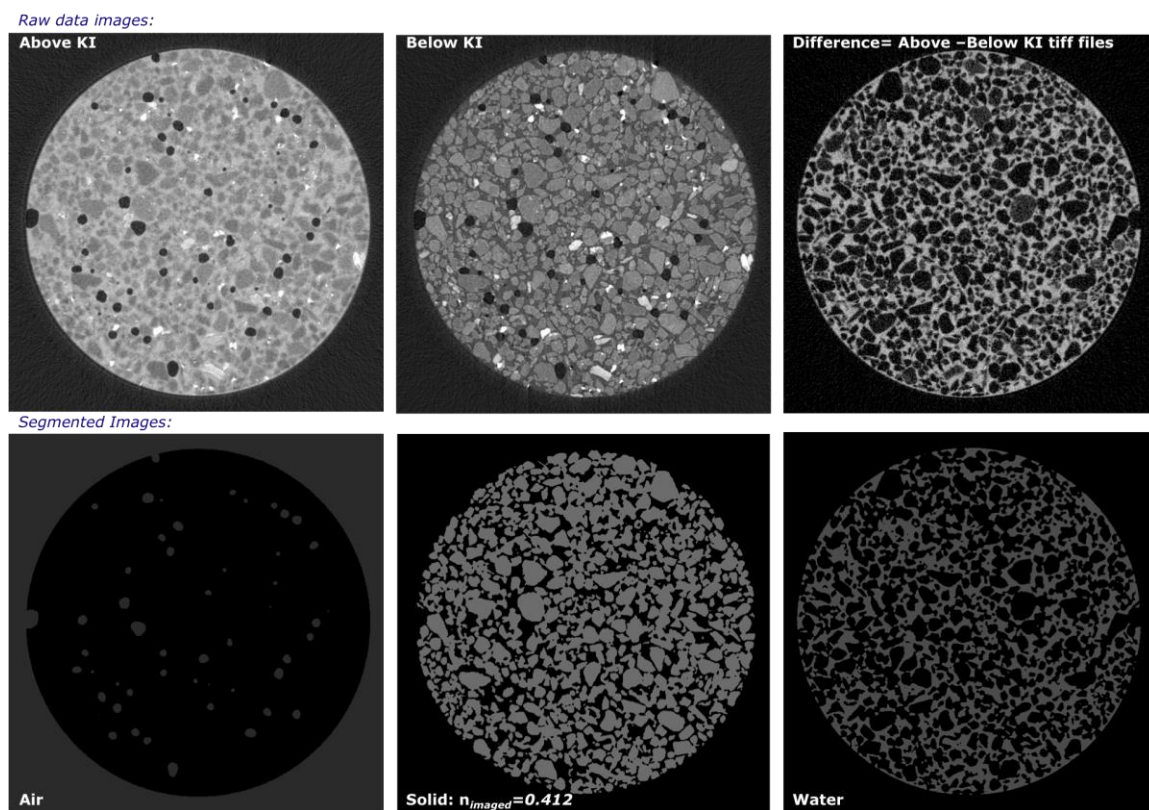
FIGURES:

Figure 1: Segmentation procedure for Vinton Soil. *Top:* A) Above iodine edge, B) Below iodine edge, C) Difference image. *Bottom:* segmented binary data corresponding to raw data above. Gravimetric porosity for this sample is 0.406.

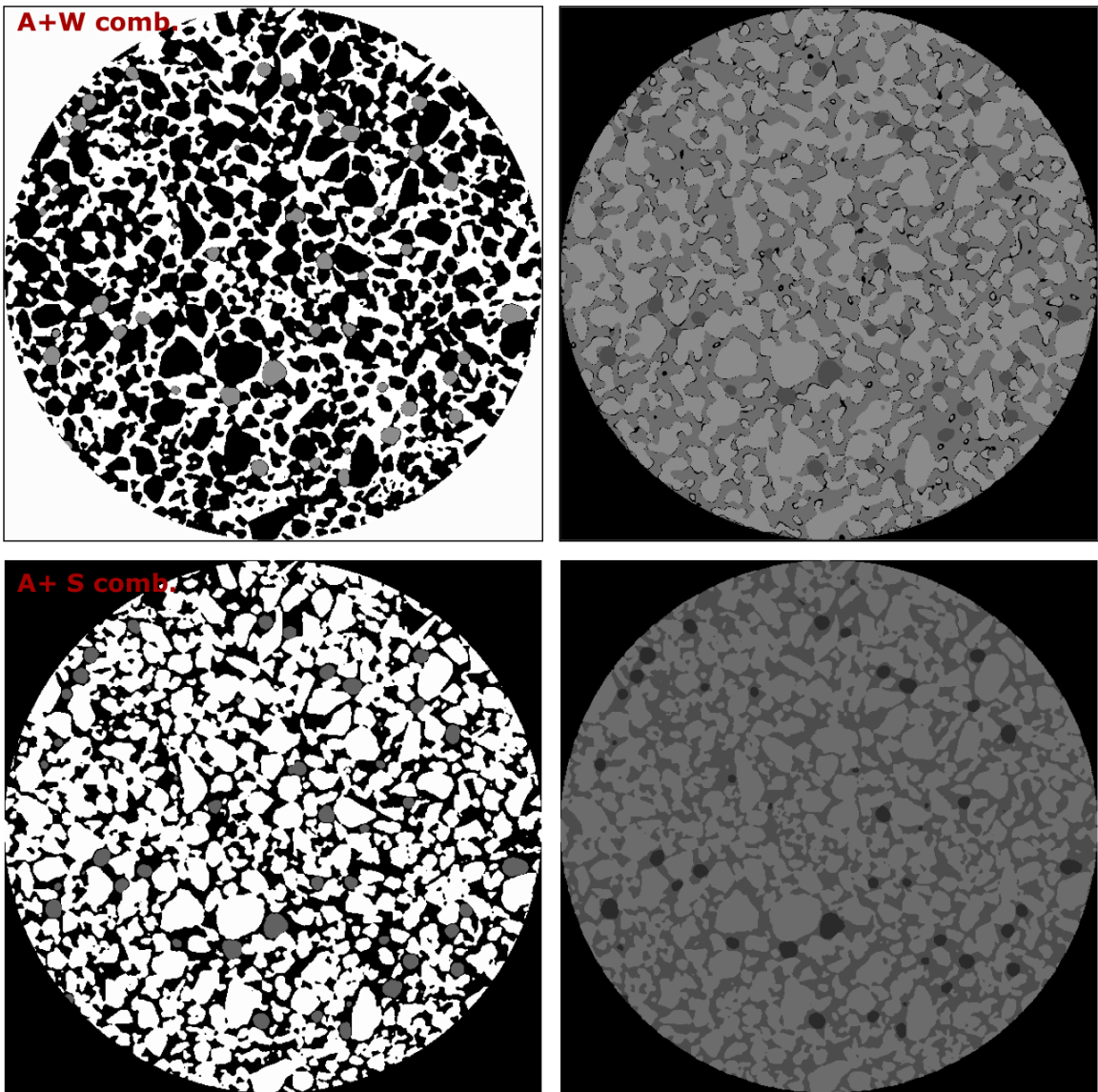


Figure 2: Example for Vinton Soil. Right: combined air-water (top), air-solid (bottom) individual segmented binary images. Left: final segmented images, ready for surface area and volume data extraction.

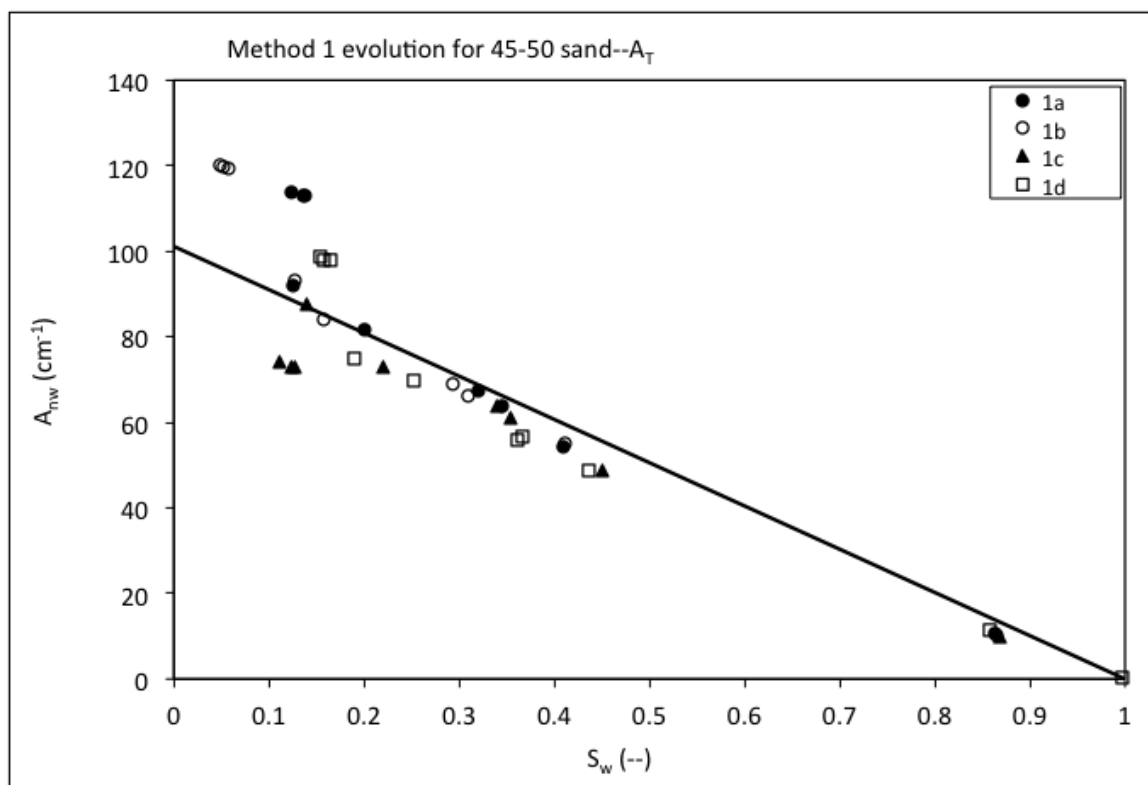


Figure 3: Total air-water interfacial area (A_{aw}) for 45/50 sand. Method 1 evolution. Note the changes in water saturation with each method. 1a) SP-air phase only (564 pixels), 1b) SP air and water phase (564 pixels), 1c) SSP matching the water phase S_w to the air (583 pixels), 1d) ISSP-M1 (567 pixels). Regression line based on average A_{max} is 101.1 cm^{-1} .

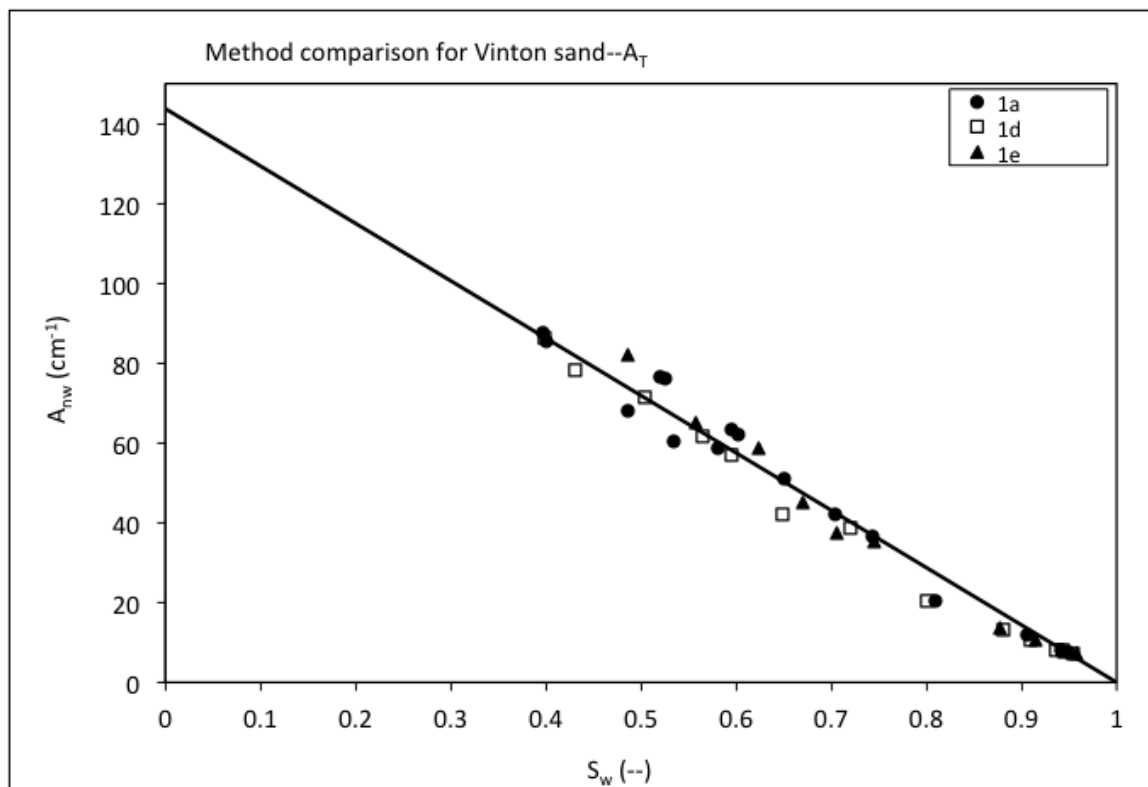


Figure 4: Total air-water interfacial area (A_{aw}) for Vinton sand. Method 1 evolution. Note the changes in water saturation with each method. 1a) SP-air phase only (578 pixels), 1d) ISSP (580 pixels). 1e) ISSP-M1 (611 pixels). Regression line based on average A_{max} is 144 cm^{-1} .

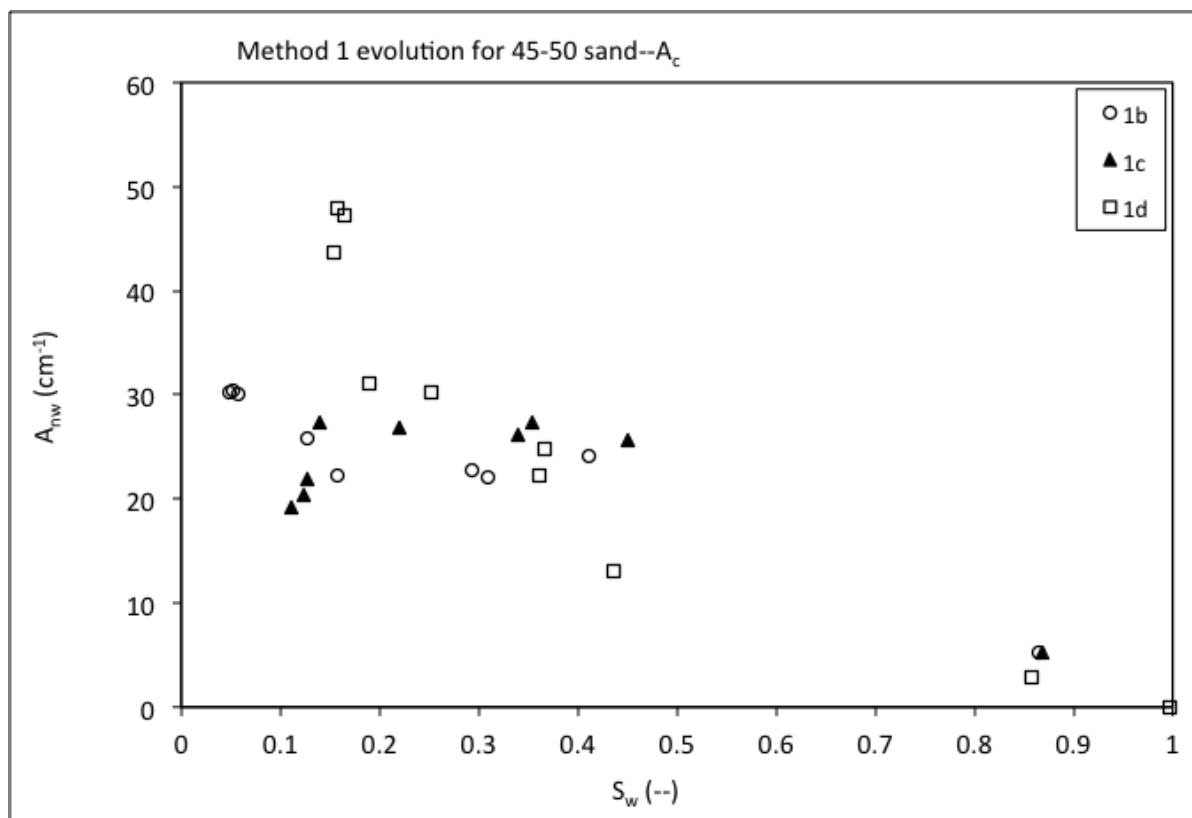


Figure 5: Capillary (C_{aw}) air-water interfacial area for 45/50 sand. Method 1 evolution. Note the changes in water saturation with each method. 1a) SP-air phase only, 1b) SP air and water phase, 1c) SSP matching the water phase S_w to the air, 1d) ISSP-M1.

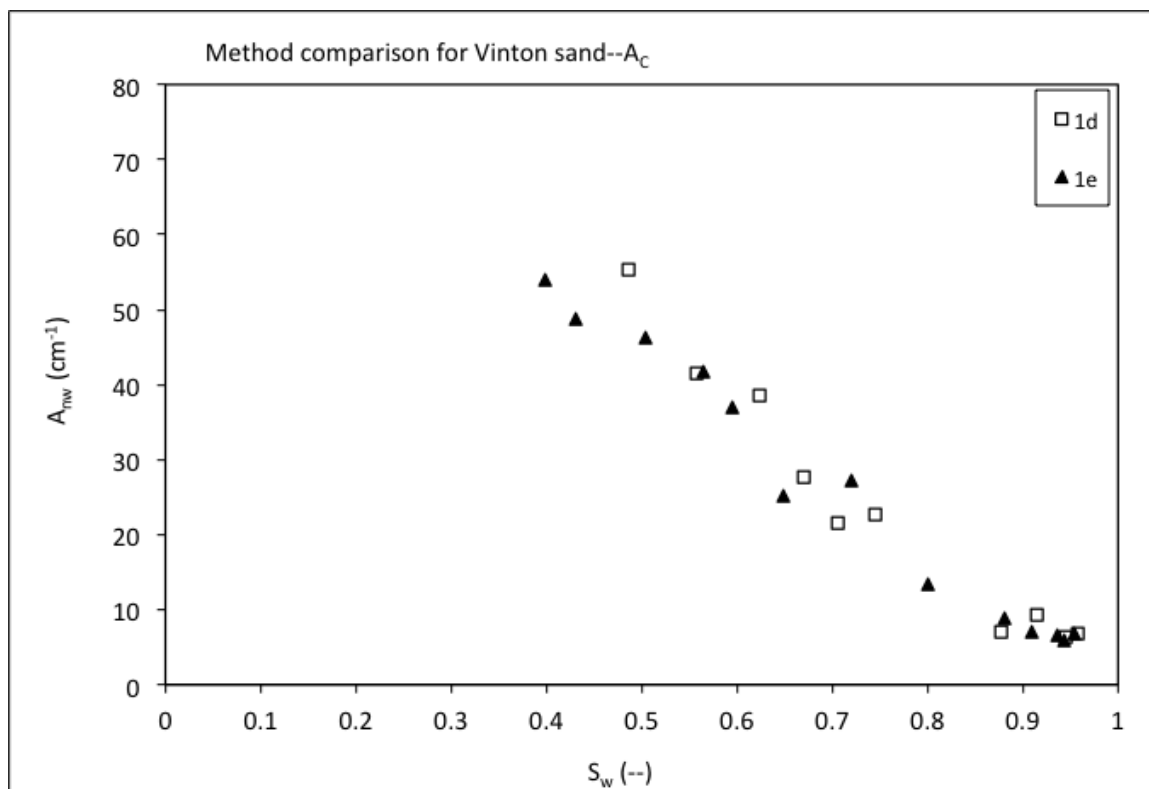


Figure 6: Capillary (C_{aw}) air-water interfacial area for Vinton sand. Method 1 evolution. Note the changes in water saturation with each method. 1d) ISSP original diameter (580 pixels). 1e) ISSP-M1 (611 pixels).

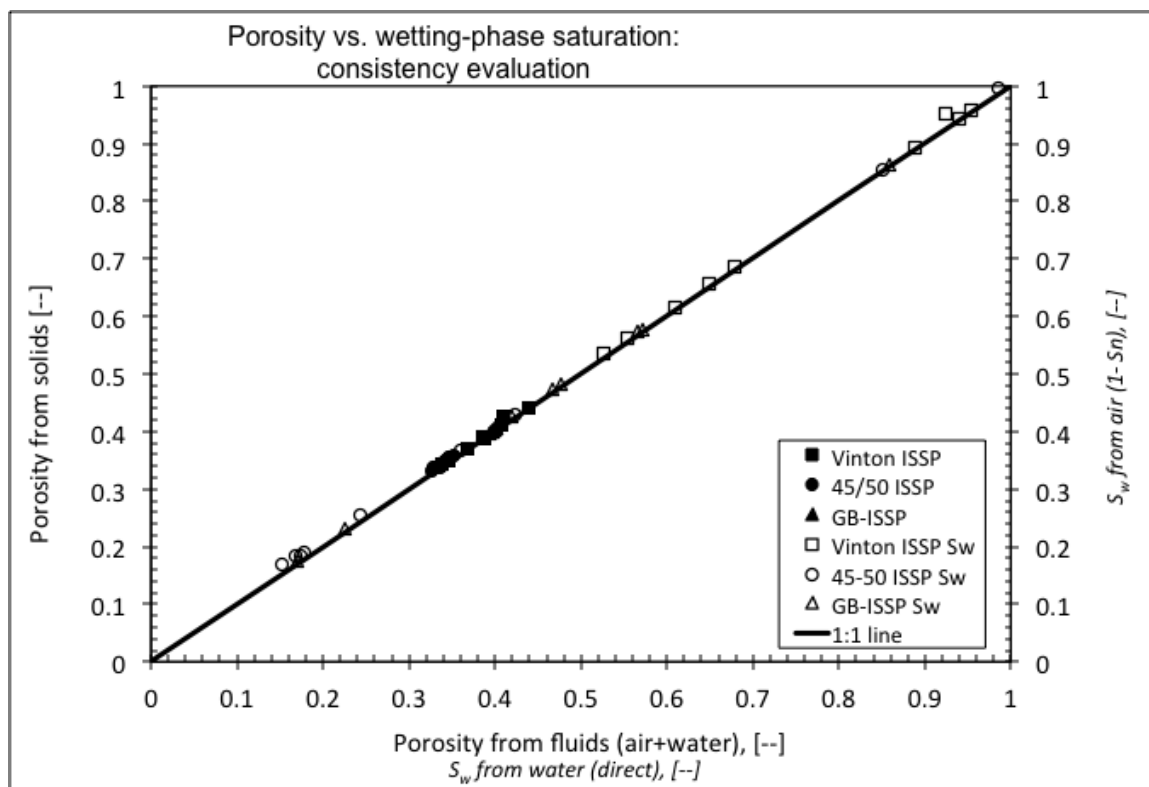


Figure 7: Comparison between porosity and saturation using the ISSP method (M1) for various porous media. Porosity is based on fluid volumes vs. porosities from solid-phase volumes and wetting-phase saturations (S_w) obtained from water-volume and those from air volumes and solid-phase porosities.

6. Additional Information

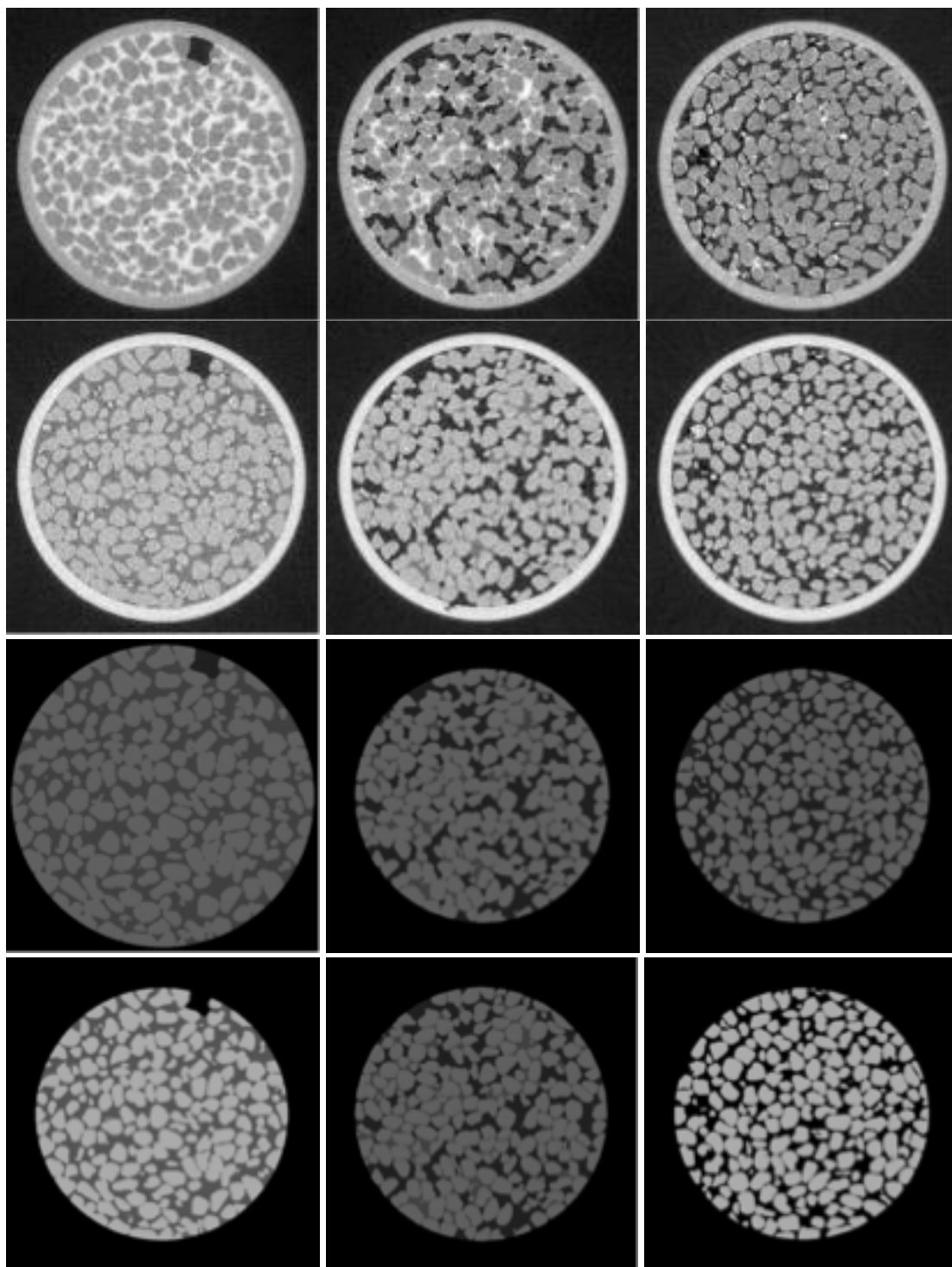
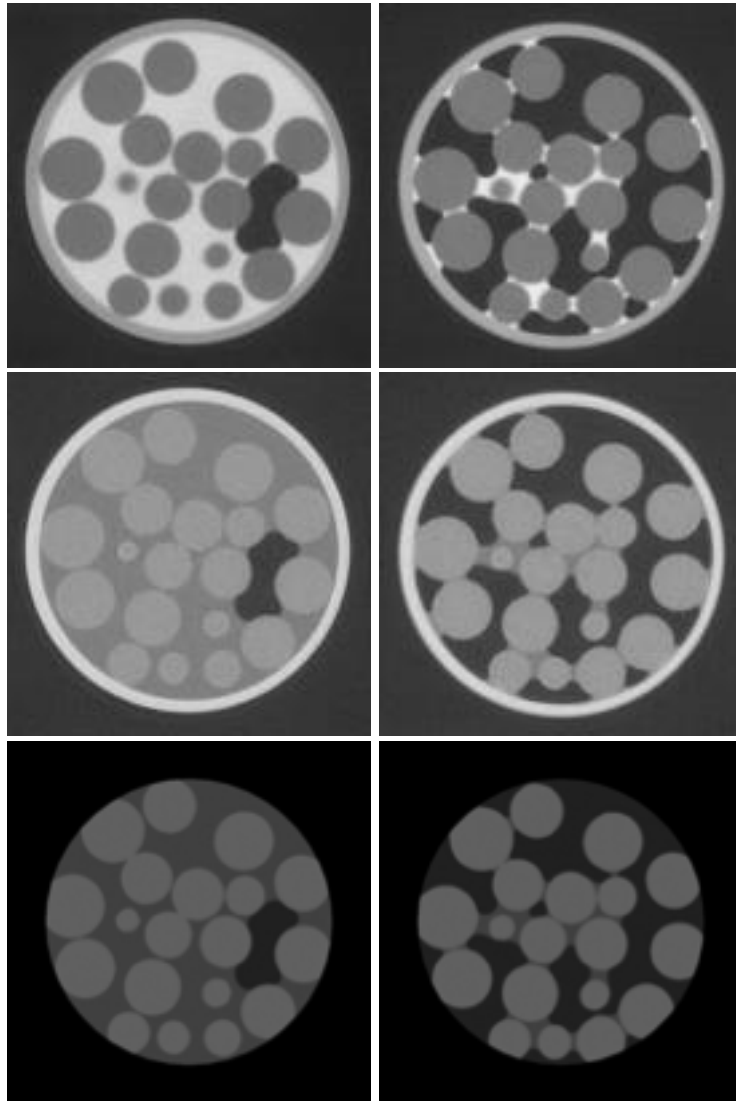
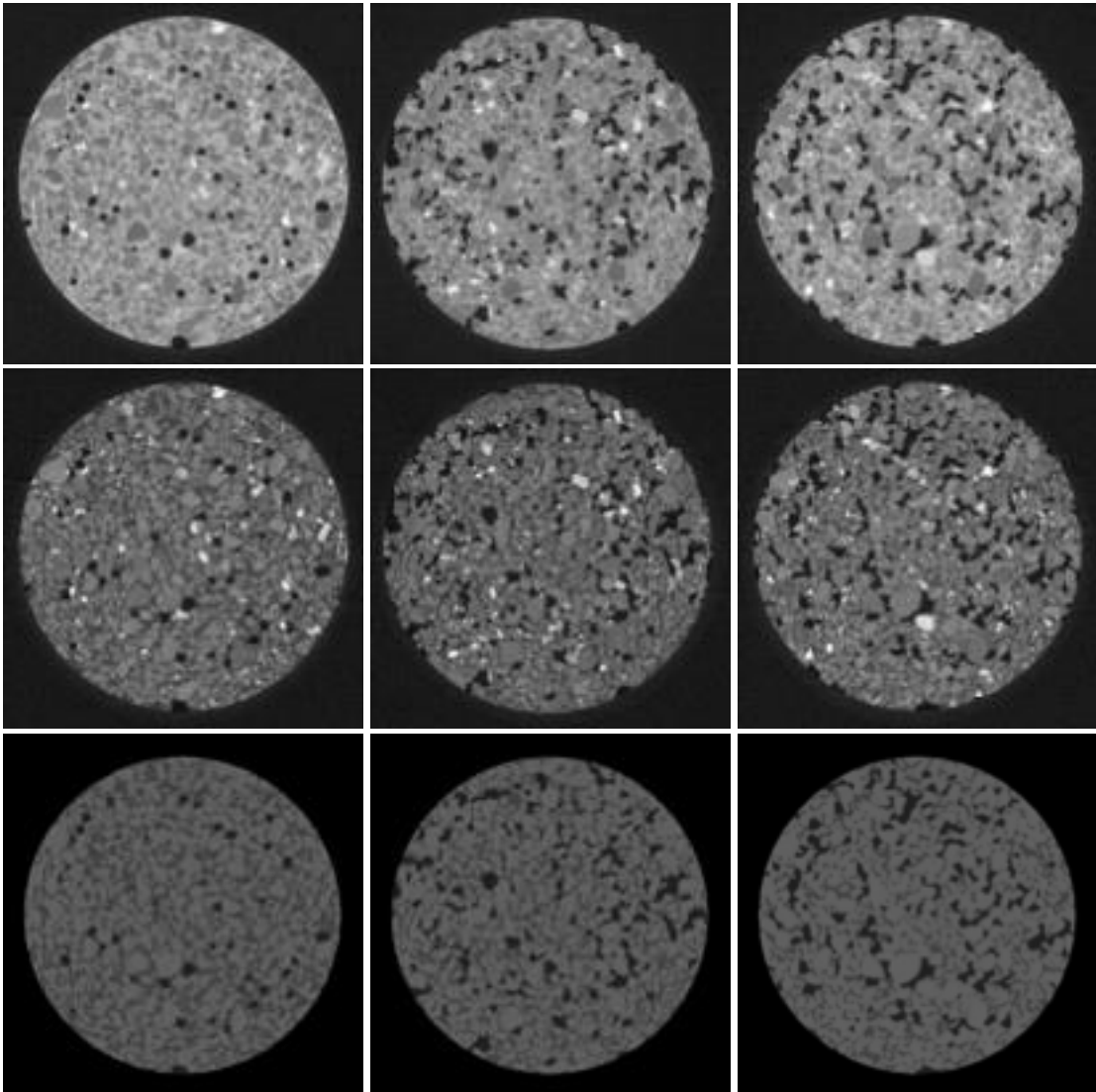


Figure 8: 45-50 sand: *From Top to bottom: Above edge, Below Edge, M1, and M2. Right to left: near saturation, intermediate, and last drainage step (low water content).*



Missing data for M2

Figure 9: Glass Beads Sample: *From Top to bottom:* Above edge, Below Edge, and M1 segmented. *Right to left:* high and low water content sample.



Missing data for M2

Figure 10: Vinton Sand: *Top to bottom*. Above edge, Below Edge, and M1. *Right to left*: near saturation, intermediate, and last drainage step (low water content).

7. Solid Surface Area Comparison to Previous Studies

Table 1: Comparison of Specific Solid Surface Areas using Method 1(ISSP), Method 2 (Appendix A), and previously reported values for Glass Beads, 45-50, and Vinton.

Glass Beads			
Narter and Brusseau (2010)	¹ XMT	30 ± 2	(1/cm)
	² IPTT	28 ± 5	(1/cm)
	³ GSSA	29 ± 10	(1/cm)
	⁴ N ₂ /BET	28 ± 2	(1/cm)
	¹ XMT-M1	29.28	(1/cm)
	³ GSSA -M1	31.09	(1/cm)
	³ GSSA -M2	30.543	(1/cm)
	⁵ A _{max} -Surface Counting ^a	53.43	(1/cm)
	⁵ A _{max} -Lindblad ^b	38.62	(1/cm)
45-50			
Brusseau et al. (2009); Brusseau et al. (2008)	^{1,5} XMT	95, 91±12	(1/cm)
	² IPTT		(1/cm)
	³ GSSA	113	(1/cm)
	⁴ N ₂ /BET	1363 ± 90	(1/cm)
	^{1,5} XMT-M1	102.2	(1/cm)
	³ GSSA-M1	111.77	(1/cm)
	³ GSSA-M2	110.68	(1/cm)
	A _{max} -Lindblad ^b	115.45	(1/cm)
Vinton			
Brusseau et al. (2009); Brusseau et al. (2010)	^{1,5} XMT	142	(1/cm)
	² IPTT		(1/cm)
	³ GSSA	149	(1/cm)
	⁴ N ₂ /BET	53454	(1/cm)
	^{1,5} XMT-M1	144.3	(1/cm)
	³ GSSA-M1	131.27	(1/cm)
	³ GSSA-M2	137.27	(1/cm)
	⁵ A _{max} -Lindblad ^b	169.76	(1/cm)

¹XMT=X-ray microtomography, ⁵A_{max}.

²IPTT=Interfacial Partitioning Tracer Test.

³GSSA=Surface Area based on smooth-sphere geometric calculations.

⁴N₂/BET=Specific Solid Surface Area based on N₂/BET measurement.

⁵A_{max}=A_{nw}/S_n. Specific maximum total interfacial area. Based on regression of A_{aw}-S_w function.

APPENDIX C
SIMULATION ON THE EFFECTS OF SURFACE AREAS ON CAPILLARY
INTERFACIAL AREA BEHAVIOUR

Due to the extensive evaluation of surface areas required for threshold method comparison (Appendix A, B), a simple spreadsheet was developed to evaluate the effects of surface area compartment on the behavior of the calculated capillary interfacial area (C_{aw}) function.

The specific total air-water interfacial area (A_{aw}) is measured based on the assumption that all solid surfaces are solvated by water. Consequently, the air surface area will approximate the solid surface area under dry conditions, and can be used as a proxy for total interfacial area. The C_{aw} was calculated as one half of the difference between the combined sum of the water phase (a_w) and air phase (a_a) surface areas and the solid phase (a_s) surface area (e.g. Montemagno and Ma, 1999; Dalla et al., 2002) respectively per equation 1.

$$C_{nw} = \frac{1}{2}(a_a + a_w - a_s) \quad (1)$$

The capillary interfacial area calculated from equation (1) refers to interfaces associated with the menisci of contacts between air and “bulk” water (partially filled capillaries, pendular rings, and wedges). This equation is developed from a simple phase-balance analysis of surface areas and interfacial contacts in a three-phase (solid, wetting

fluid, non-wetting fluid) porous medium, and includes the assumption that wetting films are not present on solid surfaces.

Figure 1 shows the volume-normalized (specific) total (A_{aw} , capillary and film) and the capillary (C_{aw}) air-water interfacial areas measured for 45-50 sand as a function of water saturation. This data was extracted from X-ray microtomography images (resolution $\sim 10 \mu\text{m}/\text{pixel}$) as the porous media was drained sequentially. Each point on the curve represents a drainage step. The images were segmented using a local threshold approach, with the application of smoothing filters to reduce noise and sharpen the boundaries between water and solid phases. The experiments, image acquisition procedure, and image analysis techniques are described extensively in Appendices A, B.

For the simulation purposes, the surface areas (cm^2) of air, water, and solid phase were used to simulate the capillary behavior as a function of changes to the air and water surface areas in this system. The changes in surface areas are attributed to changes in fluid interfaces during the drainage procedure, whereby an initially water-saturated pore is drained, and the entering air-phase will form a meniscus with the water phase. The solid phase however is set to remain constant, to reflect the static nature of solid grains throughout the drainage sequence. The shape and behavior of air and water phases were initially calibrated for the data in Figure 1.

The boundary conditions were set to accommodate for tomography-based results. At full water saturation, the air phase is not present ($a_a = 0$ at $S_w = 1$), and consequently the water surface area should be similar to the solid surface area ($a_w = a_s$). Based on experimental data, the water surface area is slightly less, presumably due to grain-grain

contacts. Likewise, the air surface area should approximate the solid surface area at $S_w=0$ ($a_a = a_s$ and $a_w = 0$). Initially, sets of two combinations were simulated based on a standard function that can reasonably fit the measured data presented in Figure 2(A).

The simulations began with a simple best fit of the measured data. A linear fit was applied for the air phase, in conjunction with a non-linear fit (log-normal) of the water phase as shown in Figure 3. This simulation resulted in a capillary surface area that is comparable to the measured data shown in Figure 1. The simulated capillary surface area increases with drainage. Then after reaching a critical saturation ($S_w \sim 0.25$), the capillary surface area decreases to 0 at $S_w=0$. The increase in C_{aw} represents the formation of menisci between the air and water phases as the air-phase enters the porous media during drainage. The subsequent decrease in C_{aw} signifies the continued drainage of smaller pore space at low S_w . Thus, this scenario represents the reality for tomography methods, where water films are not resolved. The surface area of water is also 0 at $S_w=0$.

In the next set of simulations, Figure 3(D), a linear decrease in air surface area is applied, with a constant water surface area. A constant water surface area represents the actual behavior expected for drainage of a porous medium that is water wetting. The calculated capillary surface area is shown to increase linearly with drainage in Figure 3(D). Also, the maximum calculated capillary surface area is approximately half of the total air-water interfacial area of air at $S_w=0$, as is expected from equation 1. The “capillary” area in this case is mimicking the total interfacial area due to the assumed constant water surface area (which equates to the presence of a water film solvating the solid surface).

Figure 4 shows the next set of simulations. Figure 4(E) shows results of capillary simulation for non-linear changes in surface areas of both the air and water phases. The resulting capillary behavior is similar to the initial best-fit approach (Figure 3C), as well as the measured data (Figure 2A), but with a significantly smaller magnitude. It is observed that when both fluids follow a similar trend, where both are linear or non-linear, the capillary surface area is drastically decreased. The maximum capillary is affected, occurring at 0.15-3 S_w (Figure 4E). Non-linear changes in water surface area have been observed for other 45-50 sand data processed using the M2-filt approach described in Appendix A.

Figure 4(F) shows the corresponding capillary surface area behavior as a function of linear changes in surface areas of the fluids. For Figure 4F the maximum capillary occurs at approximately 0.90 S_w , a trend that is considerably different from the measured data (Figures 1 and 2A). The simulated C_{aw} in this case is analogous to the C_{aw} behavior measured in a single wedge-shaped pore throat by Liu et al. (2011).

In this study a simple spreadsheet was put forth to evaluate the effects of surface area behavior on the shape of the calculated capillary interfacial area (C_{aw}). Results show that the behavior of fluid surface areas will affect the theoretical shape of the capillary curve. The results support the understanding of the capillary interfacial area behavior in response to changes in the configuration of fluid surface areas during a drainage cycle.

REFERENCES:

Dalla, E., M. Hilpert, and C. T. Miller (2002), Computation of the interfacial area for two-fluid porous medium systems, *Journal of Contaminant Hydrology*, 56(1-2), 25-48.

Liu, Y., D. D. Nolte, and L. J. Pyrak-Nolte (2011), Hysteresis and interfacial energies in smooth-walled microfluidic channels, *Water Resources Research*, 47.

Montemagno, C. D., and Y. Ma (1999), Measurement of Interfacial Surface Area for Two-Phase Flow in Porous Media from PVI Data, in *Characterization and measurement of the hydraulic properties of unsaturated porous media: proceedings of the International Workshop on Characterization and Measurement of the Hydraulic Properties of Unsaturated Porous Media: Riverside, California, October 22-24, 1997*, edited by M. T. van Genuchten, F. J. Leij and L. Wu, pp. 121-132, U.S. Salinity Laboratory, Agricultural Research Service Dept. of Environmental Sciences, University of California, Riverside, CA.

FIGURES:

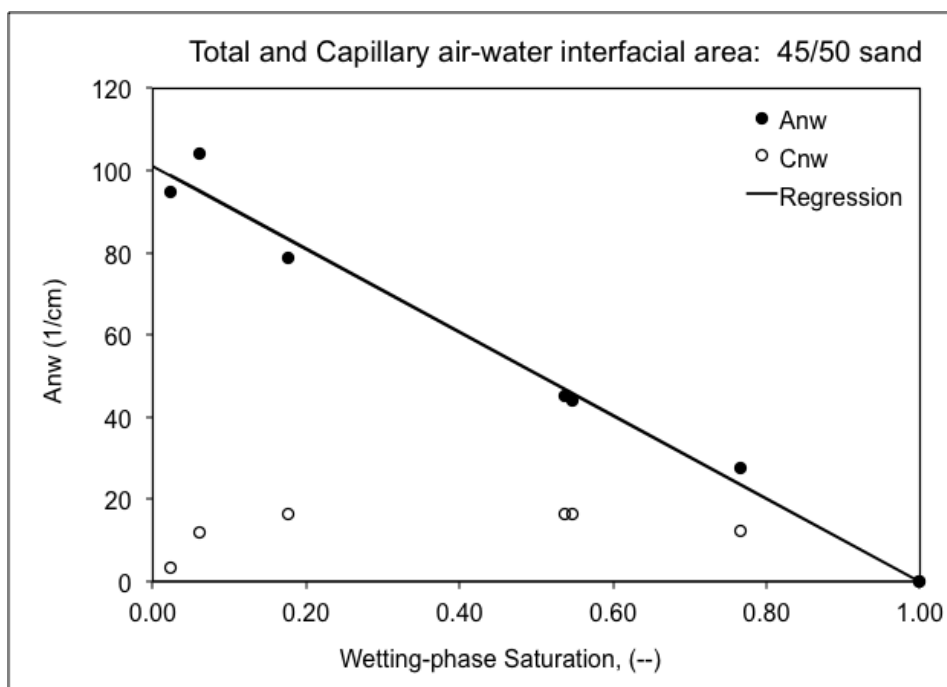


Figure 1: Total A_{nw} and C_{nw} for 45-50 sand. The maximum interfacial area ($A_{max}=(A_{nw}/(1-S_w))$) estimated from regression of A_{nw} at $S_w=0$ is 101 cm^{-1} . *Sample characteristics:* porosity=0.35, bulk density= 1.72 g/cm^3 mean particle diameter 0.35 mm.

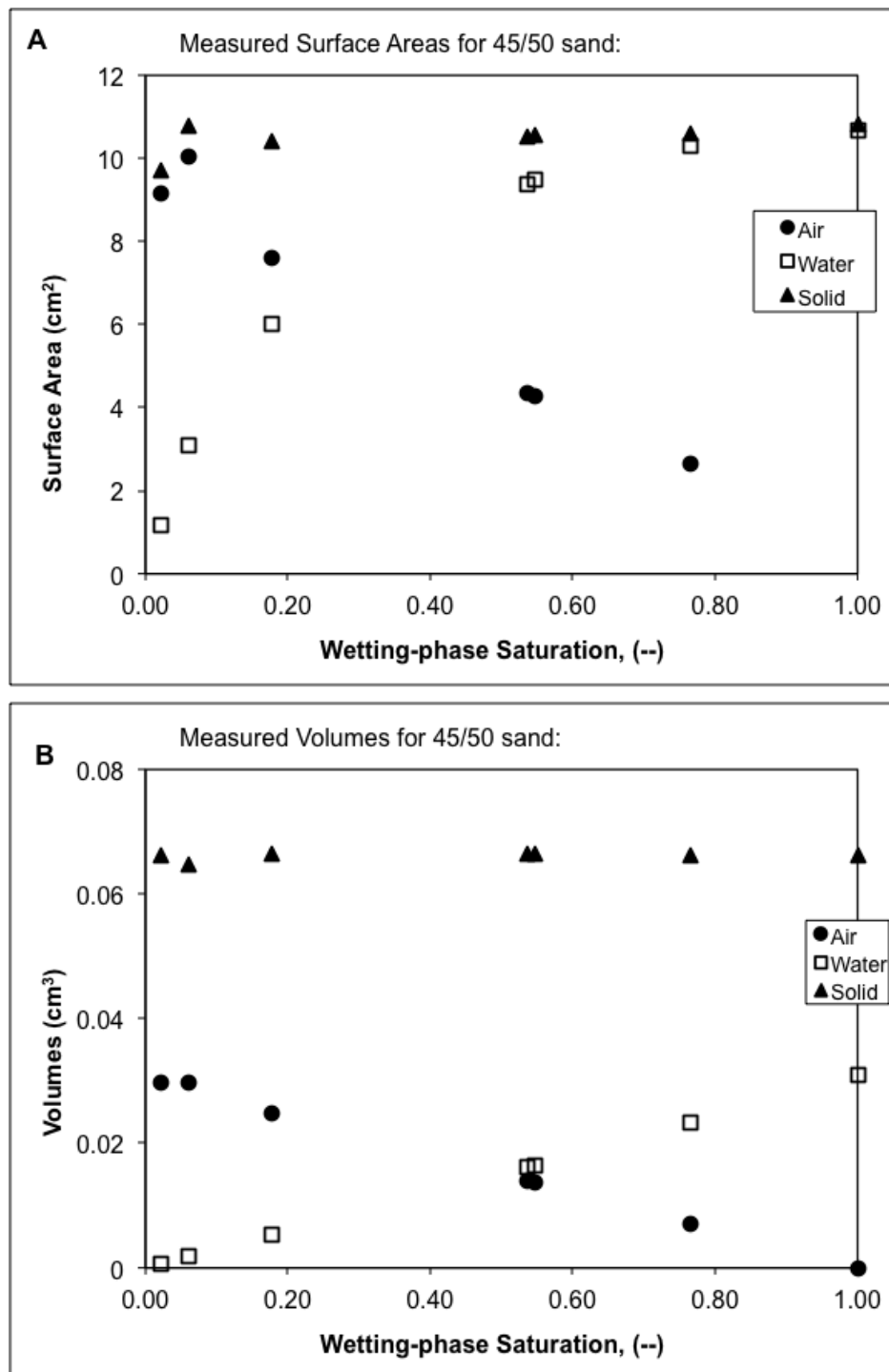


Figure 2: **A.** Surface Areas for air, water, solids, and capillary interfacial areas obtained for 45-50 sand using M2-filt. Segmentation. Capillary surface area is calculated from equation 1. **B.** The corresponding volume of each phase measured from segmentation M2-filt.

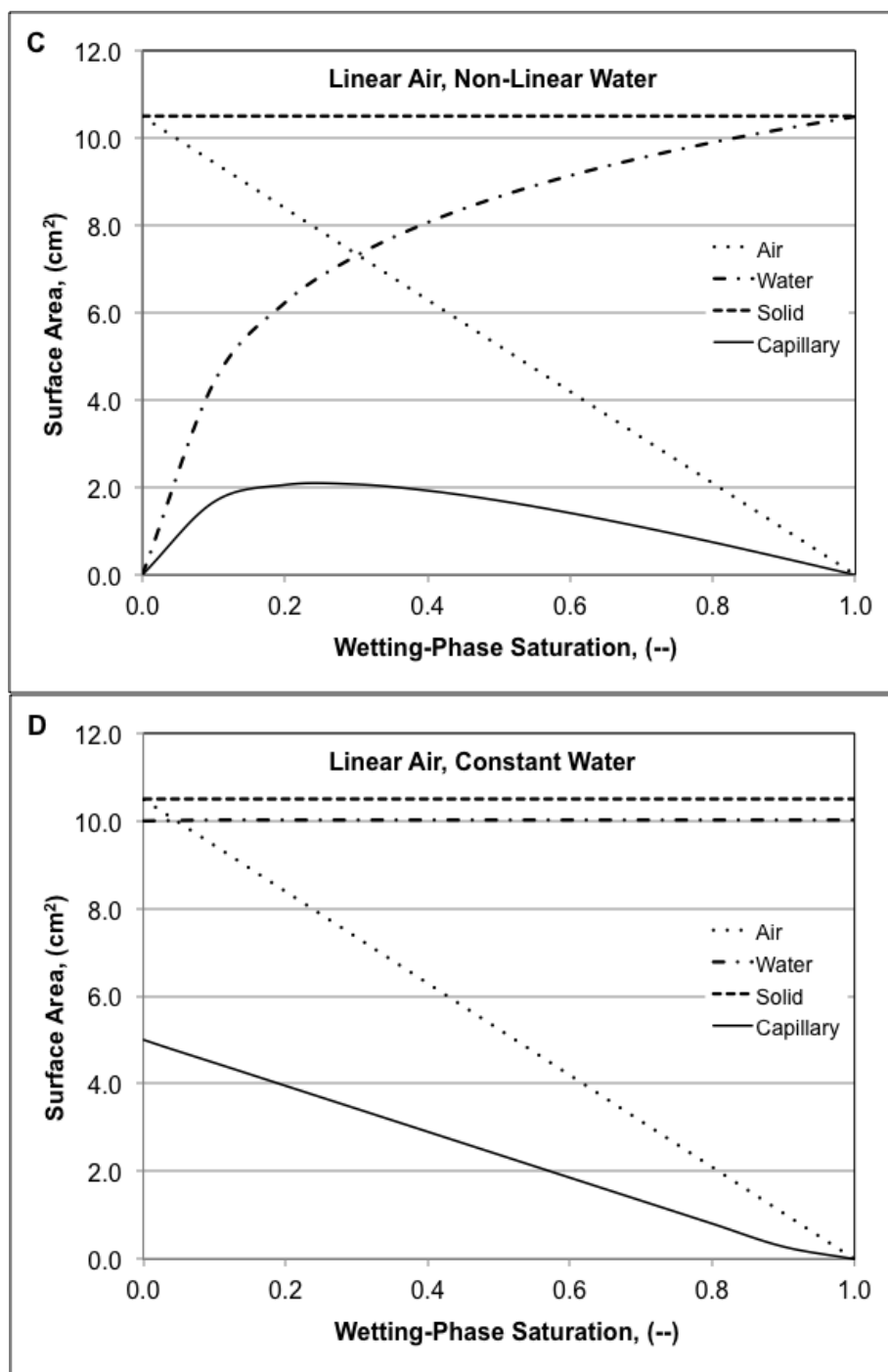


Figure 3: Simulated surface areas and corresponding Capillary surface areas for 45-50 sand. *C.* linear increase of air-phase and non-linear decrease of water with corresponding decrease in wetting-phase saturation. *D.* Linear increase in air surface area and constant water surface area.

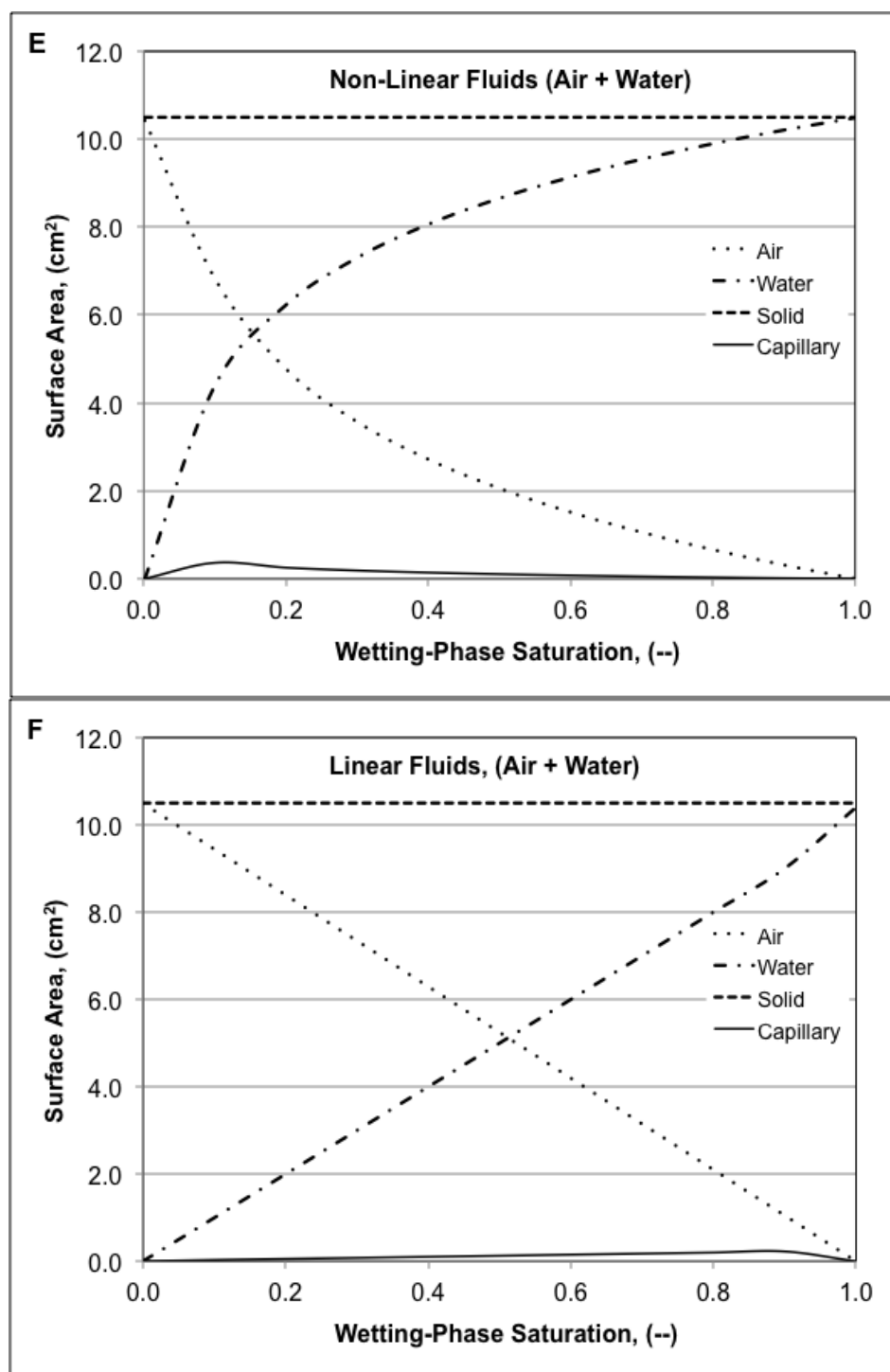


Figure 4: Simulated non-linear (*E*) and linear (*F*) fluid surface areas, and corresponding Capillary surface areas for 45-50 sand.

Additional Information

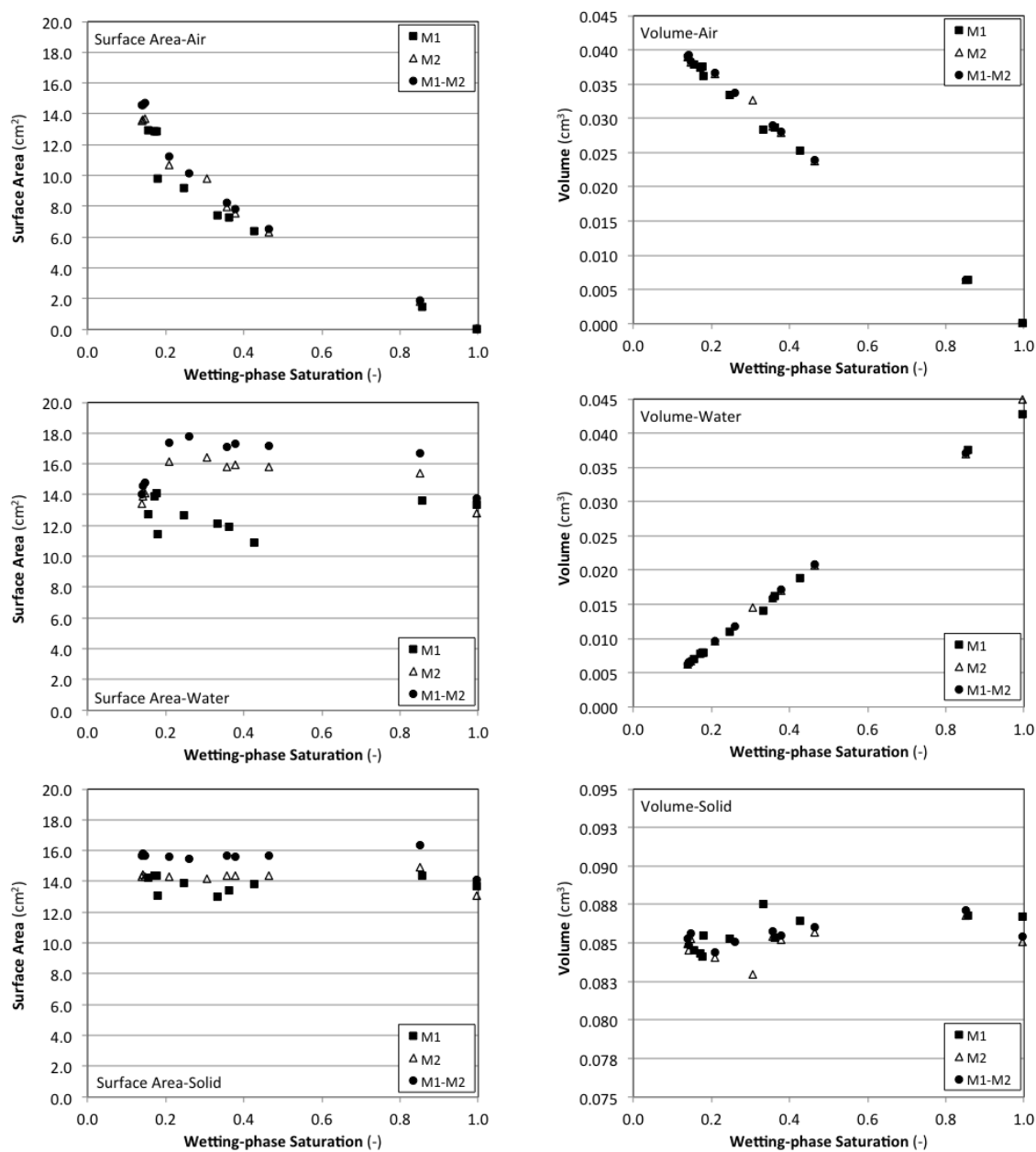


Figure 5: Volume (left) and Surface Area (right) of Air, Water and Solids per drainage step for 45-50 sand.

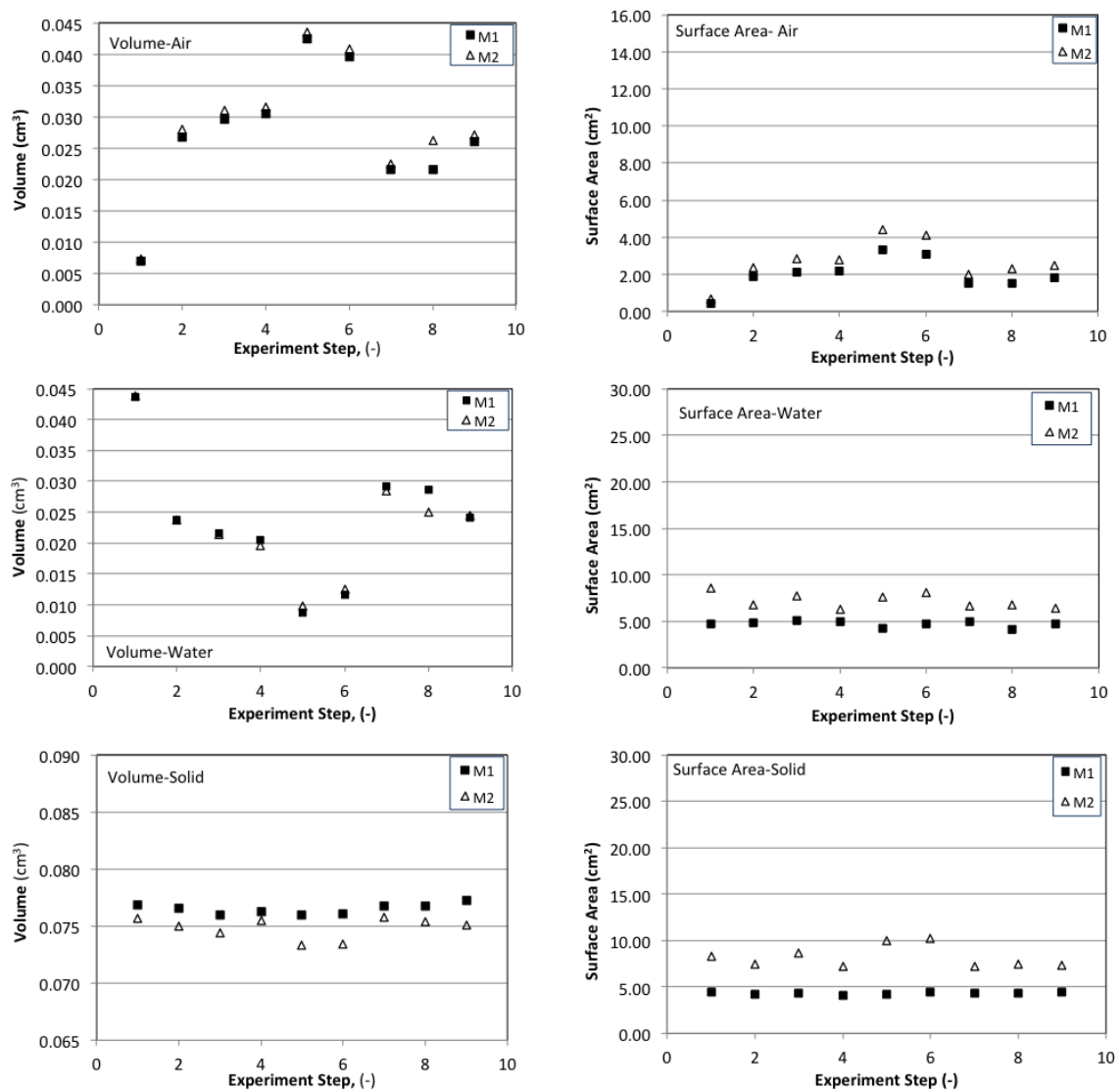


Figure 6: Volume (left) and Surface Area (right) of Air, Water and Solids per drainage step for Glass Beads.

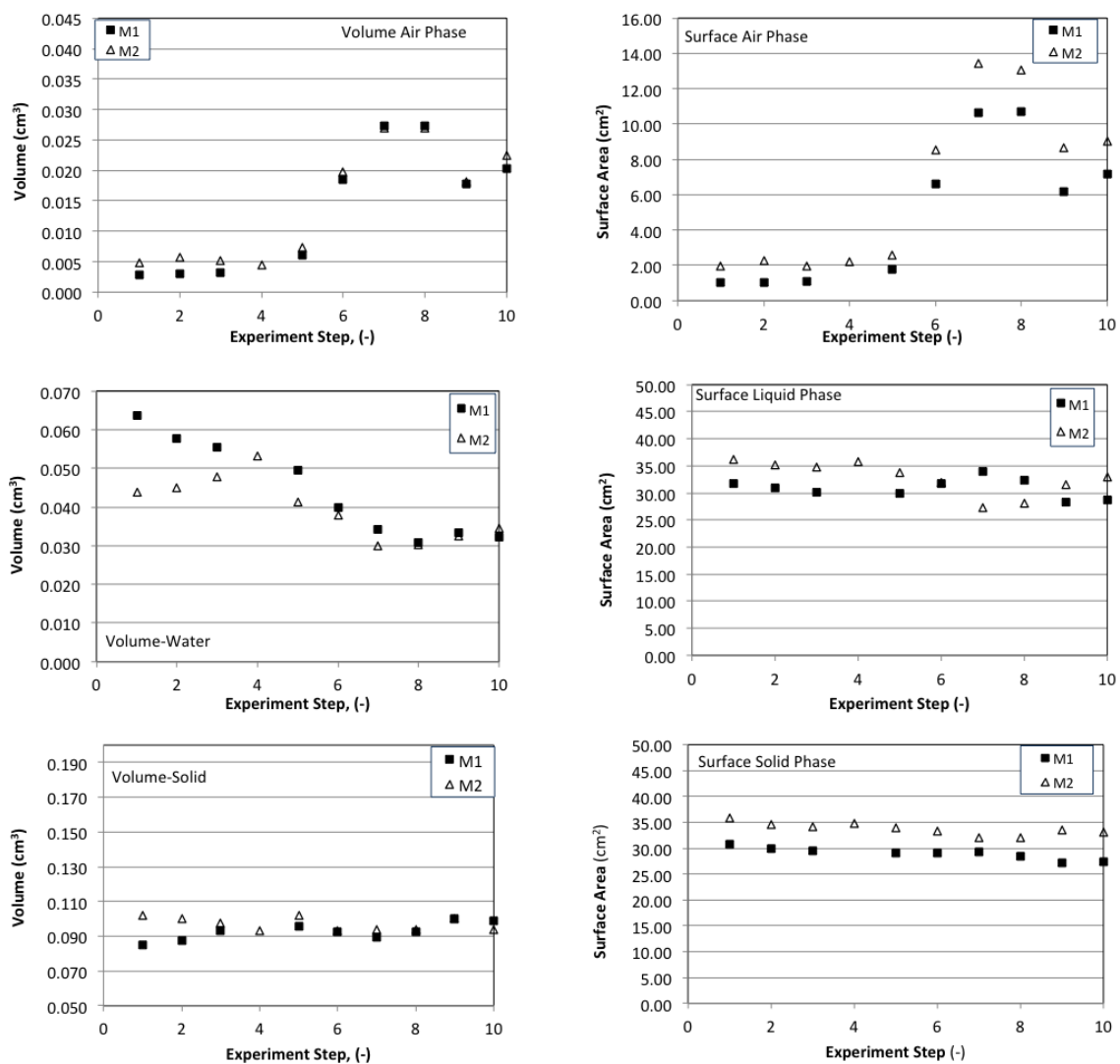


Figure 7: Volume (left) and Surface Area (right) of Air, Water and Solids per drainage step for Vinton sand.

APPENDIX D

DETERMINATION OF FILM, CAPILLARY, AND TOTAL AIR-WATER INTERFACIAL AREA USING X-RAY MICROTOMOGRAPHY

1. ABSTRACT

The air-water interface in variably saturated porous media is recognized to influence interfacial retention of organic and inorganic contaminants, and mediate various mass-transfer processes. The distribution and configuration of water in porous media under unsaturated conditions, as well as their impact on flow and retention processes, have been of sustained interest for many years. X-ray microtomography was used to measure air-water interfacial area at multiple wetting-phase saturations for natural sand. Specifically, the relationship between film interfacial area, capillary domains (menisci), and the total-measurable interfacial area was investigated. For the first time, air-water interfacial area for porous media is presented as a result of direct measurement of air-water contact surfaces. This is in contrast to previously reported data, which were derived indirectly from calculations based on measured phase surface areas and assumed conceptualizations of fluid distributions. This study provides an imaging-based approach at evaluation of water configuration, and a measurement-based framework for further understanding of air-water interfaces in natural porous media.

Keywords: X-ray Microtomography, image analysis air-water interfacial area, capillary, direct measurement of capillary, film.

2. INTRODUCTION

The distribution and configuration of water in porous media under unsaturated conditions, as well as their impact on flow and retention processes, have been of sustained interest for many years. A critical aspect of fluid configuration in unsaturated systems is the air-water interface. The air-water interface in variably saturated porous media is recognized to influence interfacial retention of organic and inorganic contaminants, and mediate various mass-transfer processes.

There are only two primary methods available to measure fluid-fluid interfacial areas for porous media systems: imaging methods involving microtomography and partitioning interfacial tracer tests. Interfacial partitioning tracer tests (IPTT) are useful for applications where knowledge of retention, mass transfer, and transformation processes are needed. This category of measurements involves tests whereby a fluid containing a tracer that partitions to the non-wetting/wetting fluid interface is injected into the porous medium. The retention behavior of the tracer is measured and used to determine the interfacial area present in the system. The interfacial areas estimated in this manner are considered to represent the effective total air-water interfacial area (A_{aw}). The total air-water interface includes the capillary and film-associated interfacial areas at target saturation (e.g. Saripalli et al., 1997; Brusseau et al., 2003; Peng and Brusseau, 2005b; Brusseau et al., 2007; Narter and Brusseau, 2010; Sung and Chen, 2011; Chen and Kibbey, 2006; Kibbey and Chen, 2012; and El Ouni, 2013).

Recent advances in X-ray microtomography technology have allowed for direct measurements of interfacial areas in porous media. Advancement in segmentation

techniques has also improved quantitative analysis, as well as the quality of results extracted from tomographic images in recent years. For example, Montemagno and Gray, (1995); Celia et al., (1998) used Photoluminescent Volumetric Imaging (PVI) which uses fluids doped with fluorophores to allow the internal structure of the system to be seen directly without optical limitations. The latter is possible due to larger sample volume, and high resolution less than 1 μm . The phase interfaces can be directly visualized, and quantitatively extracted at the sub-pore and system scale resolution. Chen et al. (2004) used photolithography cells to visualize fluid displacement in a microcell to study the relationship between capillary pressure, water saturation and interfacial areas for drainage and imbibition cycles. Similarly, Cheng et al. (2004) also report on observations between fluid-fluid interfaces, and capillary behavior using a photograph micromodel. They confirmed the presence of thin films and its contributions to porous media flow.

Direct measurements of air-water interfacial area using microtomography have been reported for either total (Brusseau et al., 2006; Schnaar and Brusseau, 2006; Brusseau et al., 2008; Brusseau et al., 2009; Narter and Brusseau, 2010) or capillary (e.g. Cheng et al., 2004; Culligan et al., 2004; Culligan et al., 2006; Wildenschild et al., 2005; Armstrong et al., 2012; Brusseau et al., 2006; Schnaar and Brusseau, 2006; Brusseau et al., 2008; Brusseau et al., 2009; Narter and Brusseau, 2010) and very seldom together in one study as presented by Brusseau et al., (2007) for a natural complex geomedia. To date, interfacial areas have been determined indirectly from microtomographic data using calculations based on measured phase surface areas and assumed conceptualizations of fluid distributions. For determining the total air-water interfacial area, the governing

assumption is that all porous medium grains are solvated by water. Specifically, the air surface area and the air-water interfacial area are equivalent if the surface area of air is in contact solely with water. Thus, the total air-water interfacial area (A_{aw}) is obtained by measuring the surface area of the air phase. The total air-water interfacial area (A_{aw}) includes thin films of which are not resolved by the microtomography method. Brusseau et al. (2010); Narter and Brusseau (2010), Appendix A, B have shown that for microtomography, the total interfacial areas are comparable to calculated geometric specific solid surface areas. These studies confirm that structural features such as surface roughness are well below the boundaries of microtomography detection limits.

The capillary interfacial area is calculated based on a conceptualization of fluid configuration in a sphere pack (e.g., Montemagno and Ma, 1999; Dalla et al., 2002). This approach is developed from a simple phase-balance analysis of surface areas and interfacial contacts in a three-phase (solid, wetting fluid, non-wetting fluid) porous medium system. The capillary interfacial area (C_{aw}) refers to interfaces associated with the menisci of contacts between air and “bulk” water (partially filled capillaries, pendular rings, and wedges). Water films are assumed to be absent. It is widely known that thin films are persistent in geomedia, unless it is oven dried (e.g. Tokunaga and Wan, 1997; Tokunaga, 2009; 2011; Baveye, 2012; Kim et al., 2012; Tokunaga, 2012). Therefore, the assumption of no films is an artifice to allow calculation of capillary interfacial area from measurement of phase surface areas. This approach has been the standard method used to determine capillary interfacial area using microtomography measurements.

The availability of synchrotron-based environmental imaging led to advances for detection of the water phase. Many studies have developed methodologies to extract features from tomography applications with the focus on mineral distribution in rocks (e.g. Nakashima and Kamiya, 2007 Ketcham et al. 2005a, 2005b; Vaz et al. 2002; Vaz et al. 2011; Gualda and Rivers 2006; Baker et al. 2012). Iassonov et al. 2009b. Iassonov and Tuller (2010); Kulkarni et al., (2012); Schlüter et al., (2010) for example, have discussed the robustness of specific segmentation methods for phase separation or grey-scale threshold selection. Brown et al., (2014) reports on challenges in measuring interfacial characteristics using x-ray microtomography.

In this work, the primary interest is in the direct measurement of air-water interfaces and the delineation between the total and capillary interfacial area. For the first time, air-water interfacial area is presented as a result of direct measurement of the air-water contact surfaces. This is in contrast to all previously reported data, which were derived indirectly from calculations using measured phase surface areas and conceptualizations of fluid distributions. This study provides an integrated imaging-based evaluation of water configuration, and a measurement-based framework for further understanding of air-water interfaces in natural porous media.

MATERIALS AND METHODS

3.1 Experiment Set-Up

Thin-walled acrylic columns, $L=3$ cm, $d_{in}=0.5$ cm, or aluminum columns, $L=3.22$ cm, $d_{in}=0.63$ cm, were packed with a 45-50 mesh quartz sand (porosity \approx 0.35, bulk

density $\approx 1.72 \text{ g/cm}^3$, $d_{50}=0.35 \text{ mm}$, and $U=1.1$), with reasonably uniform bulk densities under slurry conditions. A ($10 \text{ }\mu\text{m}$) hydrophilic capillary membrane was placed on the bottom of the column. A mesh was used at the top of the soil pack and in some cases a porous polypropylene frit was added to hold the membrane in place while packing. The saturated column was sealed and stored for imaging.

The columns were imaged prior to drainage. Drainage was induced by removing small increments of water from the column at a low flow rate, 0.05 ml/min , and allowing the fluid to equilibrate for at least 15 minutes prior to imaging. An electronic programmable syringe pump (KD Scientific) with a 2.5 mL gas-tight syringe was connected to a pressure transducer and to the bottom of the column. The top was open to the atmosphere. After the final drainage step, the column was sealed for transport back to the lab, where contents of the column were used to measure the final water content. In some instances, this also served as a second measurement of bulk density. The saturating solution contained 12% potassium iodine (KI) (Fisher Scientific) to enhance contrast between the phases in the system.

3.2 Image Acquisition

X-ray microtomography images were collected at the GeoSoilEnviroCARS (GSECARS) BM-13D beamline at the Advanced Photon Source, Argonne National Laboratory, IL. The effective resolution for our experiments is $\sim 10 \text{ }\mu\text{m}$. The field of view encapsulating the porous media is approximately 5 mm . The images were collected from the centers of the columns, to minimize the potential influence of end effects. Analysis of

the data sets indicated that representative elementary volume (REV) requirements were met for the imaged volumes employed (Brusseau et al., 2006; Narter, 2012; Culligan et al., 2004; Costanza-Robinson et al., 2008; Costanza-Robinson et al., 2011).

Sequential images of the columns were collected above and below the iodine edge, at 33.269 KeV and 33.069 KeV. The above-edge image (A-image) is used to enhance the liquid phase, and below-the-edge image (B-image) is used to distinguish the solid phase (e.g. Wildenschild et al., 2002, Schnaar and Brusseau, 2006, Costanza-Robinson et al., 2008). The images were pre-processed using GSECARS-developed software (Rivers et al., 2010; Rivers, 2012). The program is a set of IDL© (ITT, Visual Information Solutions) routines that were designed to view the CCD camera data, remove artifacts, correct for dark currents, and white field correction. Furthermore, it builds a sinogram, aligns the rotation axis, removes ring artifacts, and filters noise. Finally, the program writes the reconstructed data as a single three-dimensional volume file, which can be exported into a series of individual slices or imported into a 3D viewer such as ImageJ (Rasband, 1997-2012). Further details regarding the facility are available at the GSECars webpage.

3.3 Image Processing

The original grey-scale images were cropped using MatLab (The MathWorks Inc.). The circular crop area was chosen based on a diameter that removes the column wall while encompassing a large portion of the sample to maintain a reasonable

representative volume, REV. The cropped slices were used as the input grey-scale volume for further processing.

The quantitative image analysis is achieved using MatLab based code designed for processing large three-dimensional computed tomography data sets. The software offers the ability to distinguish several components of interest simultaneously, and uses an interactive user interface, with the possibility of semi-automated batch processing. This approach is centered on grey-scale clustering and simultaneous multiple-phase segmentation, and also accounts for intra-phase spatial variations of grey scale. The several stages of processing are combined into a MatLab program, PMIA (Kulkarni et al., 2012). The algorithm used for segmentation is a semi-automated code based on Markov-Random Field image model with ICM optimization and k-means seeding. It is a three-dimensional multiphase code that uses only one dataset, either above or below the iodine edge, for simultaneous segmentation of all 3-phases. Thus, there are no error-prone alignment and subtraction analysis required. Further information regarding the algorithm and its routines is discussed in detail in Iassonov et al., (2009); Iassonov and Tuller, (2010); Kulkarni et al., (2012); Appendix A.

For the analysis of the data presented here, the images were subjected to pre-processing (filtering) prior to segmentation. The quality of the original greyscale images, dictated the type of noise-reduction filters (e.g. median smoothing, anisotropic diffusion) used to help sharpen the boundaries between solid and water phases in the system. The application of filters was based on several subsample test sequences, and optimized for the majority. An applied connected component-labeling (CCM) post-processing filter was

used after segmentation to remove small unrealistic voxel clusters, and optimize the post-processing component. For example, voxels enclosed by another phase due to noise, or presence of bright oxides in the grain. Using the final segmented binary images, the porosity and volumetric water contents were calculated by means of simple voxel counting. The next step was to extract surface areas and volumes for all phases and to quantify contact areas between air and water phase. The method described in Lindblad, (2005) was chosen in this work for the calculation of surface area, and fluid-fluid contact areas. Details are presented in Appendix A. This method, equivalent to binary Marching Cubes, was deemed to be the most accurate method among several tested (Porter and Wildenschild, 2010).

3.4 Air-Water Interfacial Area Data Analysis

The interfacial areas reported in this work represent the specific interfacial area, unless otherwise noted, with units of cm^2/cm^3 or cm^{-1} . The surface areas are normalized by the imaged domain volume, for comparison of multiple samples and interfacial areas at different water contents, acknowledging differences in packing structure and heterogeneity. The total surface area of air, the nonwetting phase, was used to determine total air-water interfacial area (A_{aw}). This is derived from all porous medium grains being solvated by water, and thus is inclusive of thin films, which are not resolved by the microtomography method. A conceptual description of this domain is shown in Figure 1.

The capillary interfacial area (C_{aw}) was calculated as one half of the difference between the combined sum of the water phase and air phase surface areas and the solid

phase surface area (e.g., Montemagno and Ma, 1999; Dalla et al., 2002); where a_a , a_s , a_w , indicates the specific total surface areas of air, solid, and water phases respectively (equation 1):

$$C_{aw} = \frac{1}{2}(a_a + a_w - a_s) \quad (1)$$

The capillary interfacial area calculated from equation (1) refers to interfaces associated with the menisci of contacts between air and “bulk” water (partially filled capillaries, pendular rings, and wedges). These interfaces are illustrated in Figure 1. This equation is developed from a simple phase-balance analysis of surface areas and interfacial contacts in a three-phase (solid, wetting fluid, non-wetting fluid) porous medium. Water films are absent for this conceptualization.

The image-processing program provides a direct measure of the contact area between air and resolved water. The result is the surface area that exists between air and resolved water, better described as the direct measurement of the interfacial contact area, (I_{aw}).

4. RESULTS AND DISCUSSION

4.1 Total Air-Water Interfacial Area (A_{aw})

Figure 2 shows the total A_{aw} based on the surface area of air for six 45-50 data sets. The A_{aw} increases as water is removed from the column. It represents the total measurable specific surface area for this sand via tomography, which includes the capillary-associated and film-associated interfacial area. Since all solids are solvated by

water, the air phase should always be in contact with water, and does not contact the solid phase. This allows for the use of surface area of air as a proxy of the total identifiable interfacial area in the system (Figure 1).

The regression based on A_{aw} versus non-wetting phase saturation (S_n) determined the maximum air-water interfacial area (A_{max}) as $94 (\pm 7) \text{ cm}^{-1}$. For comparison, the specific-smooth sphere area (GSSA) is calculated as $113 (\pm 3) \text{ cm}^{-1}$. These results are comparable to specific solid surface area values previously reported ($92 \pm 12 \text{ cm}^{-1}$) for 45-50 Accusand, and A_{max} of 113 cm^{-1} for NAPL-water system (e.g. Brusseau et al., 2008; Brusseau et al 2009; (Appendix A, B). The measured A_{aw} values are consistent with the ~ 10 micron image resolution, which limits the detection of wetting films associated with microfeatures such as surface roughness (e.g. Brusseau et al, 2008; Narter and Brusseau 2010; Bohr et al., 2010).

4.2. Calculated Capillary Interfacial Area, (C_{aw})

Figure 2 shows the calculated capillary interfacial area results for six samples. The capillary-associated interfacial area increases with initial decrease in water saturation (S_w), reaching a maximum ($\sim 20 \text{ cm}^{-1}$) between $S_w \sim 0.30-0.35$, and then decreases with continued decrease in S_w . The C_{aw} results shown in Figure 2 are consistent with the nature of the C_{aw} - S_w function that has been reported in the literature from capillary-based models (e.g. Reeves and Celia, 1996; Dalla et al., 2002; Porter et al., 2009; Schaap and Tuller, 2010), and experimental data (e.g. Culligan et al., 2004; Culligan et al., 2006; Brusseau et al., 2007).

Measured capillary interfacial areas for natural porous media is limited. Dalla et al. (2002) produced simulated capillary and total non-wetting/wetting interfacial areas using a computational model. In this model, they created a synthetic sphere pack based on a given porosity (0.36), 1.72 g/cm^3 bulk density, and grain size distribution ($d_{50} \approx 0.33 \text{ mm}$, $U \approx 2.2$). The porous medium was designed to resemble the porous media described by Kim et al. (1997). The synthetic medium was used to generate drainage simulations and associated interfacial area computations. Due to their discretization approach applied to the isosurface of the spheres, interfacial values do not account for surface roughness. For the synthetic medium, the maximum total interfacial area (A_{max}) is approximately 120 cm^{-1} . The corresponding capillary interfacial area (C_{aw}) is approximately 25 cm^{-1} at its peak with the corresponding $S_w = 0.25$. The synthetic medium is comparable to the porous medium used in our study in terms of porosity, bulk density, and median grain size. The A_{max} value of 97 cm^{-1} obtained herein is somewhat smaller than the A_{max} reported by Dalla et al. (2002) for the synthetic medium. The C_{aw} of 20 cm^{-1} is also somewhat smaller than the maximum C_{aw} of 25 cm^{-1} occurring at $\sim 0.22 S_w$ reported by Dalla.

4.3 Fluid Surface Areas and Measured Air-Water Contact Surface Areas (I_{aw})

The impact of the surface areas of fluids on the calculated capillary-associated area was investigated in Appendix C. Figure 3 shows an example of surface areas (cm^2) and volumes (cm^3) measured for a single drainage experiment. Both the volume and the surface area of solids are shown to remain fairly constant throughout. Each surface area measurement represents a replicate measurement of the solid surface area in the system.

The small range of variability obtained amongst the replicates (2%) confirms the robustness of the image analysis method used, and serve as a benchmark to evaluate segmentation outputs.

The surface area of air in Figure (3) is shown to increase linearly with decreasing water content. At $S_w=0$ ($S_n=1$), the air surface area approximates the solid surface area ($a_a = a_s$). At full saturation, the air phase is not present ($a_a = 0$ at $S_w=1$), thus the water surface area approximates the surface area of solids ($a_w = a_s$). The water surface area is observed to decrease non-linearly with a decrease in water saturation reaching zero, consistent with the no-film assumption for tomographic data.

Figure 4 shows the results of the measured contact surface area between the air and water (I_{aw}) as a function of wetting-phase saturation. The I_{aw} values are lower than the total A_{aw} obtained from the surface area of air, and significantly larger than the calculated C_{aw} . The maximum difference occurs at the curvature portion of both I_{aw} and C_{aw} . The I_{aw} increases initially with drainage, reaching a maximum at $\sim 0.30 S_w$, and decreases again approaching a C_{aw} value of 0 when dry. The measured I_{aw} exhibits the same behavior as the C_{aw} curve.

The I_{aw} values are consistently higher than the calculated capillary values. However, it is critical to evaluate the uncertainty associated with the measurements. One way to assess data uncertainty is to examine variability among the data presented in Figure 4. Inspection of the data reveals that there is minimal variability for both I_{aw} and C_{aw} . For the data set presented herein, the mean SSA obtained directly from image analysis is $107 \pm 2 \text{ cm}^{-1}$, which is very close to the GSSA of $113 \pm 3 \text{ cm}^{-1}$ based on an

overall imaged porosity of 0.33 ± 0.002 . The A_{\max} is $94 \pm 3 \text{ cm}^{-1}$ and is comparable to the SSA for 45-50 reported in the literature. Another way to assess uncertainty is based on evaluating error associated with the imaging processing procedures. As mentioned above, the solid surface area obtained from processing the image data for each experiment step should be the same. As noted, there was minimal variability (2%) amongst the replicates. Porter and Wildenschild (2010) investigated the errors associated with several methods for calculating surface areas from microtomographic data, and the binary Marching Cubes approach was shown to have the lowest associated error ($\sim 4\%$). The various measures indicate a relatively small degree of uncertainty for the measurements, thus it is concluded that the observed difference between C_{aw} and I_{aw} is real and significant.

4.4 Interfacial Domains Comprising the Total Interfacial Area (A_{aw})

The capillary air-water interfacial area C_{aw} is the contribution of “bulk fluid” including menisci formed between air-water in partially filled capillaries, which form a meniscus between air-water phases. The geometrical representation of the C_{aw} by Montemagno and Ma (1999) and Dalla et al. (2002) is shown in Figure 1A. This conceptualization explicitly excludes films known to coat the surface of solids based on theoretical considerations employed for their numerical analyses. The presence of wetting films (F_{w}) (Figure 1B) has been implicitly incorporated in the total interfacial area domain. As discussed earlier, the total interfacial area (A_{aw}) represents the total measurable air (nonwetting) surface area in the system, which includes capillary (menisci between air-water phases) and films. The premise that all grains are solvated by water is

instrumental in the definition of A_{aw} , since this measurement incorporates all contact points between the air-phase and the thin wetting-films (F_w) that coat grain surfaces. The implication (Figure 1B) is the air-phase appears to have direct contact with the solid phase when films are neglected (Figure 1A).

Figure 4 shows larger I_{aw} results when compared to C_{aw} . Thus, the direct measurement of actual contact surfaces between air and water produced additional air-water interface not captured by the capillary calculation (eqn 1). This entity will be referred to as “additionally resolved” interfacial area. The measured air-water interfacial area (I_{a-w}) is thus defined as:

$$I_{aw}=C_{aw}+R_{aw} \quad (2)$$

where R_{aw} is additionally resolved air-water interface.

Based on these differences in results for measured air-water I_{aw} (Figure 4) and calculated C_{aw} , an operational definition is developed for interfacial area (such as wetting films) that cannot be resolved, denoted as F_w , using computed tomography. Features that are approximately 10 μm or larger is considered measurable using a robust image-processing program. Wetting films are calculated from equation (3) and additionally resolved air-water interface (R_{aw}) are quantified from equation (4). Note that the capillary (C_{aw}) remains the same, as previously discussed (Figure 2).

$$F_w=A_{aw}-I_{aw} \quad (3)$$

$$R_{aw}=I_{aw}-C_{aw} \quad (4)$$

4.5. Contributions of Additionally Resolved interfacial area (R_{aw}) and Films (F_w) to Total Interfacial Area (A_{aw})

Figure 5 shows the different domains as a result of the directly measured interfacial area I_{aw} . Results are shown as wetting (thin) films and additionally resolved air-water interfacial area (R_{aw}). The surface area of thin films (F_w) increases as the porous medium becomes drier. The resolved air-water interface (R_{aw}) however, reaches a maximum, and then tapper off as the column is further drained. This behavior mimics the C_{aw} and I_{aw} results observed from Figure 4.

Figure 6 shows the relative contribution of capillary (C_{aw}), R_{aw} , and (F_w) films to the measurable total (A_{aw}) with respect to water saturation. Here, the C_{aw} contribution decreases linearly as saturation in the sand decreases, as would be expected. These results are also consistent with previous observed behavior in Figure 5, and Figure 6. Conversely, thin films (F_w) show an inverse relationship, increasing its contribution as the column becomes less saturated such that $a_s \approx a_a$ as S_w approaches zero.

Figure 7 shows an example of a drainage sequence experiment using 1-mm glass beads. At low saturation, it is possible to observe diminished conductivity between the pores, and an increase presence of pendular rings and wedges. As the additionally resolved fluid interfaces disappear, thin films become prevalent and thinning sufficiently until it only covers the sand grains. This process is analogous to the three saturation types described in other studies for unsaturated columns (e.g. *Gvirtzman and Roberts, 1991; Haines, 1930; Bear, 1988*).

The measurement of fluid-fluid contact (I_{aw}) areas includes interfacial area associated with additional water configurations in which the menisci-forming contact area thickness is similar or larger than the image resolution, and thus can be resolved by the method. This additional interfacial area is excluded from the calculated C_{aw} . This would for example, entail features associated with surfaces of the solid, such as water held by pits and crevices in the grain. These topological features are larger than microscopic surface roughness. Figure 8 shows a slice sequence (A-F) perpendicular to the z-axis for a 1- μm resolution image of 45-50 sand. In Figure 8A, three distinct air bodies are present in separate pores. Farther into the column (towards the center), an apparent increase in connectivity of air bodies is observed, together with the shadow of a partial solid grain. The air phase now (Figure 8C) is connected. An indentation appears on right-most middle grain. The indentation is shown in the series with a red arrow. In figure 8E this indentation is clearer, and shows that it is now filled with water. For better visualization, Figure 8E is also shown in a false color overlay on the right. Several slices further, it is noticeable that as the air phase invades the pore space, and different configuration is noted, such that other grain indentations are visible. An image of an independent Scanning-Electron Microscopy (SEM) image, (200 μm) for an Accusand is included for visualization of topological heterogeneity that can be detected at higher resolutions. Figure 9 shows a 3D image for 45-50 sand at 1 μm resolution, imaged at the end of a full drainage sequence, $S_w \sim 0.2$. This is the full volume for the data presented in Figure 8. In Figure 9, it is possible to observe pit locations in the longitudinal axis of the grains, where water can accumulate. Further evaluation of 3D configurations at this

resolution may help in quantifying the areas associated with the measured I_{aw} , and the additional resolved interfaces (R_{aw}).

Water films occur naturally in unsaturated soils in the environment. The thickness of films has been shown to influence sorption processes of contaminants (e.g. Lee et al., 1988; Brusseau and Rao, 1989; Brusseau et al., 1990; Brusseau and Rao, 1990) despite negligible contributions to advective flow (e.g. Dullien et al., 1986; Dalla et al., 2002). There remains some uncertainty on the thickness at which films can affect mobilization of colloids and nanoparticles in the environment (e.g. Baveye, 2012). Capillary forces and adsorption of water onto solid grains retain the water occurring in geomedia. The permanent water film on the surfaces of water-wetting porous media is partially attributed to water molecule-solid interactions, as well as to microscopic surface roughness (e.g. Brusseau et al., 2007; Brusseau et al., 2010; Narter and Brusseau, 2010; Kibbey and Chen, 2012; Kibbey, 2013). Adsorption of water in this study is defined as the interactions between water molecules and water-wetting solid grains (e.g. Brusseau 1991; Orchiston 1953).

Gvirtzman et al. (1987) used a cold stage SEM technique to investigate the water phase in unsaturated natural porous media. The rapid freezing allowed for observation of water menisci configurations in the system, with sufficient resolution to calculate capillary pressure (based on curvature) and observe surface roughness. Cheng et al. 2004 observed the presence of thin films in the small micromodel gas-wetting fluid system. They concluded that even though they confirmed the presence of thin films the lateral optical resolution of 0.6 μm limited further quantification. Water films coating the grain

surfaces have been reported in the literature (e.g., Haines, 1930; Orchiston, 1953; Gvirtzman and Roberts, 1991; Vazquez et al., 2005; Baveye, 2012; to exist in the range of 1-100 nm in thickness. Bohr et al. (2010) measured the thickness of water film adsorbed to the surface of calcite using synchrotron x-ray reflectivity technique. Overall they report film thicknesses between 0.3 and 1.6 nm depending on experimental conditions. Others cited in (Bohr et al.) determined films ranging between 0.13-5.7 nm (Bohr et al. 2010). Tokunaga (2011) reports water film thicknesses between 1-20 nm in drained pores and in fractures. More interestingly, they presented predicted film thickness on mineral surfaces as a function of matric potential, and grain size. The predicted film thickness would range between 1 nm- 1 μ m. At this scale, these films are well below the image resolution 10 μ m, and can be compared to surface roughness features, well below the detection limit of microtomography method (e.g. Peng and Brusseau, 2005b, 2005a; Brusseau et al., 2007; Brusseau et al., 2010; Narter and Brusseau, 2010).

4.6 Implications (Comparison to Gas-phase Tracer Tests, GPTT)

The contributions of film and capillary have been established. The data is compared to the gas-phase interfacial partitioning tracer test data (*Peng and Brusseau, 2005b, 2005a*), to further compare the practical measured A_{ia} to the maximum possible A_{GPTT} . Figure 10a shown the GPTT data measured for 40/50 sand by Peng and Brusseau (2005) The predicted model is adapted to 45/50 sand characteristics. Note that 45-50 sand is obtained by sieving the 40/50 sand with a finer mesh. Therefore, both sands are assumed to be very similar in terms of grain surface roughness and chemical properties.

Figure 10b shows the significant difference in magnitude between GPTT (A_{GTPP}) and total measured A_{aw} . Likewise, this is observed between the capillary and fluid-fluid interfacial areas in Figure 10b. The gas-phase interfacial partitioning tracer test yields results that are similar to the surface area measured by N_2 BET. These values represent the maximum measurable surface area for this porous medium. It accounts for surface heterogeneities as well as other micro-properties of the sand, which are only accessible to gas tracer molecules.

In the past there has been several discussions regarding the different interfacial domains accessible to different measurement techniques (i.e. Costanza-Robinson and Brusseau, 2003). These results suggest that direct measurements of interfacial areas using microtomography is limited by the resolution of the system. Similar conclusions have been made with respect to aqueous-phase tracer tests compared to microtomography results (e.g. Brusseau et al., 2006; Brusseau et al., 2007; Brusseau et al., 2008; Brusseau et al., 2010; Narter and Brusseau, 2010). Concisely, these observations highlight the importance of discernment and further characterization of interfacial domains measured directly using microtomography.

5. CONCLUSIONS

X-ray microtomography was used to measure air-water interfacial area at multiple wetting-phase saturations for natural sand. Specifically, the relationship between film interfacial area, capillary domains (menisci), and the total-measurable interfacial area was investigated. For the first time, air-water interfacial area is presented as a result of direct

measurement of contact surfaces between air and water. This is in contrast to previously reported data, which were derived indirectly from calculations based on measured phase surface areas and assumed conceptualizations of fluid distributions.

Hydraulic processes such as drainage and imbibition are highly dependent on interfacial areas present. This domain in particular has been incorporated in several models (e.g. Chen and Doolen, 1998; Cheng et al., 2004; Hassanizadeh and Gray, 1990; 1993; Porter et al., 2009; Tuller and Or, 2000) for characterizing and prediction of flow and transport in the porous media. This work clarifies interfacial areas defined by segmentation ability to resolve wetting films at a given resolution. The information regarding the contribution of films and capillary interfaces maybe helpful for more accurate mechanistic predictions in future work.

Acknowledgments

The authors would like to thank Dr. Tuller, Ramaprasad Kulkarni, for providing us with the PMIA code; Dr. Marcel Schaap (The University of Arizona), Dr. Mark Rivers (APS), and the UA Contaminant Transport Group for their assistance in data collection. This research was supported by the NIEHS-Superfund Research Program (Grant ES 04940). Use of the Advanced Photon Source, an Office of Science User Facility operated for the U.S. Department of Energy (DOE) Office of Science by Argonne National Laboratory, was supported by the U.S. DOE under Contract No. DE-AC02-06CH11357. We acknowledge the support of GeoSoilEnviroCARS (Sector 13), which is supported by

the National Science Foundation—Earth Sciences (EAR-1128799), and the Department of Energy, Geosciences (DE-FG02-94ER14466).

7. REFERENCES

- Armstrong, R. T., M. L. Porter, and D. Wildenschild (2012), Linking pore-scale interfacial curvature to column-scale capillary pressure, *Advances in Water Resources*, 46, 55-62.
- Baveye, P. C. (2012), Comment on “Physicochemical controls on adsorbed water film thickness in unsaturated geological media” by Tetsu K. Tokunaga, *Water Resources Research*, 48(11), n/a-n/a.
- Bear, J. (1988), *Dynamics of fluids in porous media*, Dover, New York.
- Brown, K., S. Schluter, A. Sheppard, and D. Wildenschild (2014), On the challenges of measuring interfacial characteristics of three-phase fluid flow with x-ray microtomography, *Journal of Microscopy*, 253(3), 171-182.
- Brusseau, M. L., and P. S. C. Rao (1989), Sorption Nonideality during Organic Contaminant Transport in Porous-Media, *Crit Rev Env Contr*, 19(1), 33-99.
- Brusseau, M. L., and P. S. C. Rao (1990), Modeling Solute Transport in Structured Soils - a Review, *Geoderma*, 46(1-3), 169-192.
- Brusseau, M. L., R. E. Jessup, and P. S. C. Rao (1990), Sorption Kinetics of Organic-Chemicals - Evaluation of Gas-Purge and Miscible-Displacement Techniques, *Environmental Science & Technology*, 24(5), 727-735.
- Brusseau, M. L., N. T. Nelson, and M. S. Costanza-Robinson (2003), Partitioning Tracer Tests for Characterizing Immiscible-Fluid Saturations and Interfacial Areas in the Vadose Zone, *Vadose Zone Journal*, 2(2), 138-147.
- Brusseau, M. L., M. Narter, and H. Janousek (2010), Interfacial Partitioning Tracer Test Measurements of Organic-Liquid/Water Interfacial Areas: Application to Soils and the Influence of Surface Roughness, *Environmental Science & Technology*, 44(19), 7596-7600.
- Brusseau, M. L., S. Peng, G. Schnaar, and M. S. Costanza-Robinson (2006), Relationships among air-water interfacial area, capillary pressure, and water saturation for a sandy porous medium, *Water Resources Research*, 42(3).
- Brusseau, M. L., S. Peng, G. Schnaar, and A. Murao (2007), Measuring air-water interfacial areas with X-ray microtomography and interfacial partitioning tracer tests, *Environmental Science & Technology*, 41(6), 1956-1961.

Brusseau, M. L., H. Janousek, A. Murao, and G. Schnaar (2008), Synchrotron X-ray microtomography and interfacial partitioning tracer test measurements of NAPL-water interfacial areas, *Water Resources Research*, 44(1).

Brusseau, M. L., M. Narter, S. Schnaar, and J. Marble (2009), Measurement and Estimation of Organic-Liquid/Water Interfacial Areas for Several Natural Porous Media, *Environmental Science & Technology*, 43(10), 3619-3625.

Celia, M. A., W. G. Gray, C. D. Montemagno, and P. C. Reeves (1998), On the inclusion of interfacial area in models of two-phase flow in porous media, in *Iahs-Aish P*, edited by M. Herbert and K. Kovar, pp. 81-87.

Chen, L., and T. C. G. Kibbey (2006), Measurement of air-water interfacial area for multiple hysteretic drainage curves in an unsaturated fine sand, *Langmuir*, 22(16), 6874-6880.

Chen, S., and G. D. Doolen (1998), Lattice Boltzmann method for fluid flows, *Annual Review of Fluid Mechanics*, 30, 329-364.

Cheng, J. T., L. J. Pyrak-Nolte, D. D. Nolte, and N. J. Giordano (2004), Linking pressure and saturation through interfacial areas in porous media, *Geophysical Research Letters*, 31(8).

Costanza-Robinson, M. S., and M. L. Brusseau (2003), Air-water interfacial areas in unsaturated soils: Evaluation of interfacial domains (vol 37, art no 1195, 2002), *Water Resources Research*, 39(4).

Costanza-Robinson, M. S., K. H. Harrold, and R. M. Lieb-Lappen (2008), X-ray microtomography determination of air-water interfacial area-water saturation relationships in sandy porous media, *Environmental Science & Technology*, 42(8), 2949-2956.

Costanza-Robinson, M. S., B. D. Estabrook, and D. F. Fouhey (2011), Representative elementary volume estimation for porosity, moisture saturation, and air-water interfacial areas in unsaturated porous media: Data quality implications, *Water Resources Research*, 47(7), n/a-n/a.

Culligan, K. A., D. Wildenschild, B. S. B. Christensen, W. G. Gray, and M. L. Rivers (2006), Pore-scale characteristics of multiphase flow in porous media: A comparison of air-water and oil-water experiments, *Advances in Water Resources*, 29(2), 227-238.

Culligan, K. A., D. Wildenschild, B. S. B. Christensen, W. G. Gray, M. L. Rivers, and A. F. B. Tompson (2004), Interfacial area measurements for unsaturated flow through a porous medium, *Water Resources Research*, 40(12), n/a-n/a.

Dalla, E., M. Hilpert, and C. T. Miller (2002), Computation of the interfacial area for two-fluid porous medium systems, *Journal of Contaminant Hydrology*, 56(1-2), 25-48.

Dullien, F. A. L., F. S. Y. Lai, and I. F. Macdonald (1986), Hydraulic Continuity of Residual Wetting Phase in Porous-Media, *Journal of Colloid and Interface Science*, 109(1), 201-218.

El Ouni, A. (2013), Measuring Air-Water Interfacial Area in Unsaturated Porous Media Using the Interfacial Partitioning Tracer Test Method, edited, p. 62 leaves, University of Arizona, University of Arizona.

Gvirtsman, H., and P. V. Roberts (1991), Pore Scale Spatial-Analysis of 2 Immiscible Fluids in Porous-Media, *Water Resources Research*, 27(6), 1165-1176.

Haines, W. B. (1930), Studies in the physical properties of soil V The hysteresis effect in capillary properties, and the modes of moisture distribution associated therewith, *Journal of Agricultural Science*, 20, 97-116.

Hassanizadeh, S. M., and W. G. Gray (1990), Mechanics And Thermodynamics Of Multiphase Flow In Porous-Media Including Interphase Boundaries, *Advances in Water Resources*, 13(4), 169-186.

Hassanizadeh, S. M., and W. G. Gray (1993), Thermodynamic Basis Of Capillary-Pressure In Porous-Media, *Water Resources Research*, 29(10), 3389-3405.

Iassonov, P., and M. Tuller (2010), Application of Segmentation for Correction of Intensity Bias in X-Ray Computed Tomography Images, *Vadose Zone Journal*, 9(1), 187.

Iassonov, P., T. Gebrenegus, and M. Tuller (2009), Segmentation of X-ray computed tomography images of porous materials: A crucial step for characterization and quantitative analysis of pore structures, *Water Resources Research*, 45(9), n/a-n/a.

Kibbey, T. C. G. (2013), The configuration of water on rough natural surfaces: Implications for understanding air-water interfacial area, film thickness, and imaging resolution, *Water Resources Research*, 49(8), 4765-4774.

Kibbey, T. C. G., and L. X. Chen (2012), A pore network model study of the fluid-fluid interfacial areas measured by dynamic-interface tracer depletion and miscible displacement water phase advective tracer methods, *Water Resources Research*, 48.

Kim, T. W., T. K. Tokunaga, D. B. Shuman, S. R. Sutton, M. Newville, and A. Lanzirotti (2012), Thickness measurements of nanoscale brine films on silica surfaces under geologic CO₂ sequestration conditions using synchrotron X-ray fluorescence, *Water Resources Research*, 48.

Kulkarni, R., M. Tuller, W. Fink, and D. Wildenschild (2012), Three-Dimensional Multiphase Segmentation of X-Ray CT Data of Porous Materials Using a Bayesian Markov Random Field Framework, *Vadose Zone Journal*, 11(1).

Lee, L. S., P. S. C. Rao, M. L. Brusseau, and R. A. Ogwada (1988), Nonequilibrium Sorption of Organic Contaminants during Flow through Columns of Aquifer Materials, *Environmental Toxicology and Chemistry*, 7(10), 779-793.

Lindblad, J. (2005), Surface area estimation of digitized 3D objects using weighted local configurations, *Image and Vision Computing*, 23(2), 111-122.

Montemagno, C. D., and W. G. Gray (1995), Photoluminescent Volumetric Imaging - A Technique For The Exploration Of Multiphase Flow And Transport In Porous-Media, *Geophysical Research Letters*, 22(4), 425-428.

Narter, M. (2012), Characterizing Non-Wetting Fluid in Natural Porous Media Using Synchrotron X-Ray Microtomography, edited, p. 172 leaves, University of Arizona, University of Arizona.

Narter, M., and M. L. Brusseau (2010), Comparison of interfacial partitioning tracer test and high-resolution microtomography measurements of fluid-fluid interfacial areas for an ideal porous medium, *Water Resources Research*, 46.

Orchiston, H. D. (1953), Adsorption Of Water Vapor .1. Soils At 25-Degrees-C, *Soil Science*, 76(6), 453-465.

Peng, S., and M. L. Brusseau (2005a), Impact of soil texture on air-water interfacial areas in unsaturated sandy porous media, *Water Resources Research*, 41(3).

Peng, S., and M. L. Brusseau (2005b), Gas-phase partitioning tracer test method for water content measurement: Evaluating efficacy for a range of porous-medium textures, *Vadose Zone Journal*, 4(3), 881-884.

Porter, M. L., M. G. Schaap, and D. Wildenschild (2009), Lattice-Boltzmann simulations of the capillary pressure-saturation-interfacial area relationship for porous media, *Advances in Water Resources*, 32(11), 1632-1640.

Reeves, P. C., and M. A. Celia (1996), A functional relationship between capillary pressure, saturation, and interfacial area as revealed by a pore-scale network model, *Water Resources Research*, 32(8), 2345-2358.

Rivers, M. L. (2012), tomoRecon: High-speed tomography reconstruction on workstations using multi-threading, *Proc Spie*, 8506.

- Rivers, M. L., D. T. Citron, and Y. B. Wang (2010), Recent developments in computed tomography at GSECARS, *Proc Spie*, 7804.
- Saripalli, K. P., H. Kim, P. S. C. Rao, and M. D. Annable (1997), Measurement of specific fluid - Fluid interfacial areas of immiscible fluids in porous media, *Environmental Science & Technology*, 31(3), 932-936.
- Schaap, M. G., and M. Tuller (2010), Quantitative Pore-Scale Investigations of Multiphase Bio/Geo/Chemical Processes, *Vadose Zone Journal*, 9(3), 573-575.
- Schlüter, S., U. Weller, and H.-J. Vogel (2010), Segmentation of X-ray microtomography images of soil using gradient masks, *Computers & Geosciences*, 36(10), 1246-1251.
- Schnaar, G., and M. L. Brusseau (2006), Characterizing pore-scale configuration of organic immiscible liquid in multiphase systems with synchrotron X-ray microtomography, *Vadose Zone Journal*, 5(2), 641-648.
- Sung, M., and B. H. Chen (2011), Using aliphatic alcohols as gaseous tracers in determination of water contents and air-water interfacial areas in unsaturated sands, *J Contam Hydrol*, 126(3-4), 226-234.
- Tokunaga, T. K. (2009), Hydraulic properties of adsorbed water films in unsaturated porous media, *Water Resources Research*, 45(6), n/a-n/a.
- Tokunaga, T. K. (2011), Physicochemical controls on adsorbed water film thickness in unsaturated geological media, *Water Resources Research*, 47(8), n/a-n/a.
- Tokunaga, T. K. (2012), DLVO-Based Estimates of Adsorbed Water Film Thicknesses in Geologic CO₂ Reservoirs, *Langmuir*, 28(21), 8001-8009.
- Tokunaga, T. K., and J. Wan (1997), Water film flow along fracture surfaces of porous rock, *Water Resources Research*, 33(6), 1287-1295.
- Tuller, M., and D. Or (2000), Hydraulic functions for macroporous soils, *Preferential Flow: Water Movement and Chemical Transport in the Environment*, 37-40.
- Vazquez, R., R. Nogueira, S. Busquets, J. L. Mata, and B. Saramago (2005), Wetting films of polar and nonpolar liquids, *J Colloid Interface Sci*, 284(2), 652-657.
- Wildenschild, D., J. W. Hopmans, M. L. Rivers, and A. J. R. Kent (2005), Quantitative analysis of flow processes in a sand using synchrotron-based X-ray microtomography, *Vadose Zone Journal*, 4(1), 112-126.
- Wildenschild, D., J. W. Hopmans, C. M. P. Vaz, M. L. Rivers, D. Rikard, and B. S. B. Christensen (2002), Using X-ray computed tomography in hydrology: systems, resolutions, and limitations, *Journal of Hydrology*, 267(3-4), 285-297.

FIGURES

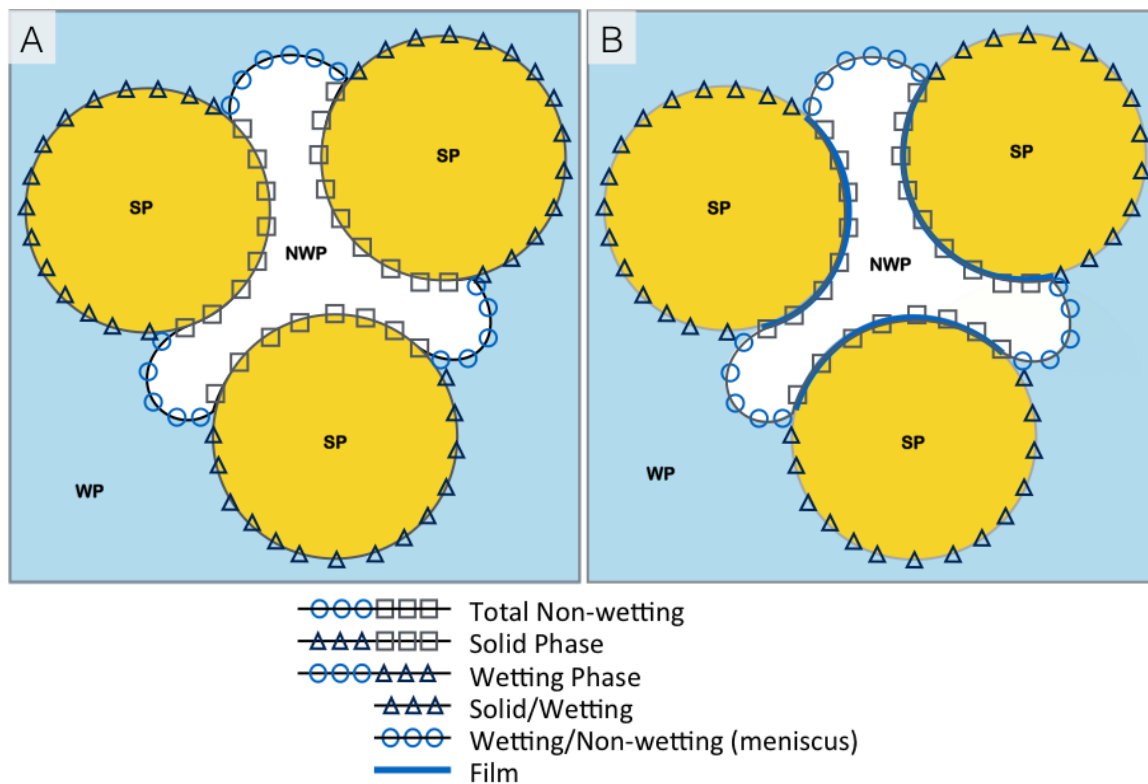


Figure 1: Conceptual representation of surface areas in a pore, adapted from Dalla et al. (2002). **A.** Fluid-fluid configuration in microtomography samples. **B.** Representation of films not resolved by tomography methods.

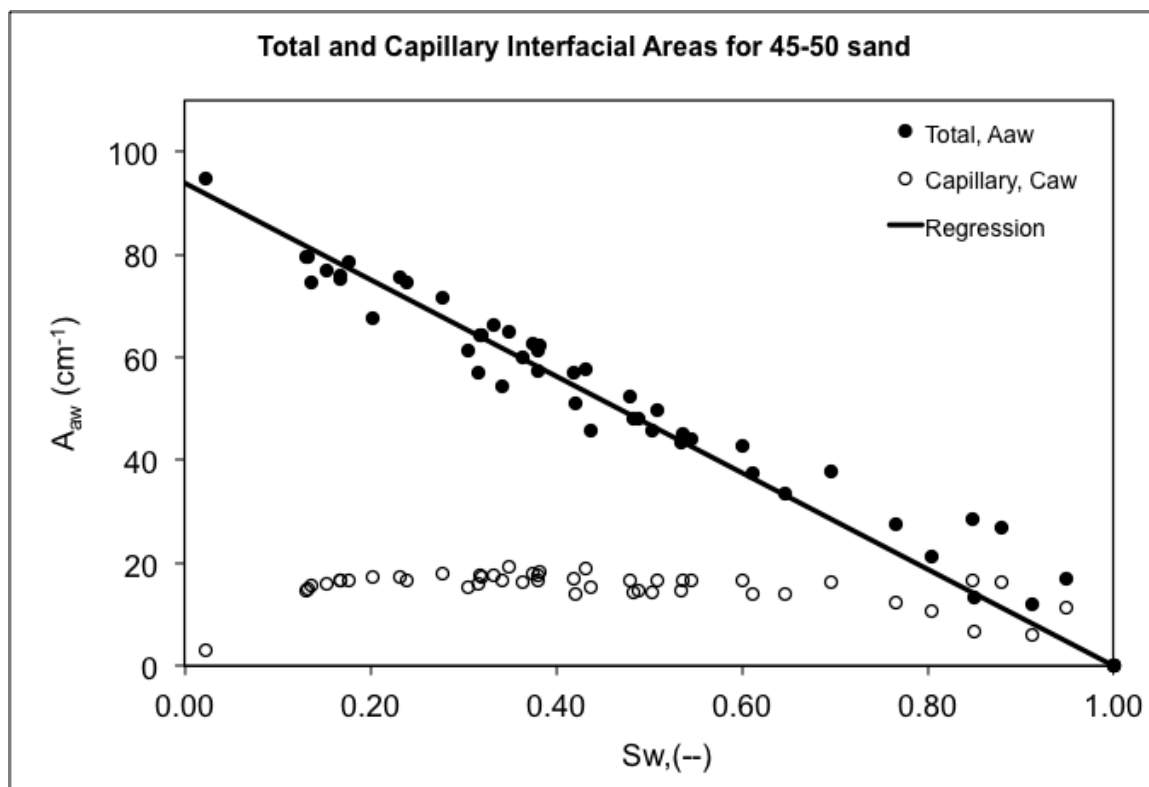


Figure 2: Specific total interfacial area (A_{aw}) and specific Capillary interfacial area (C_{aw}), as a function of water saturation (S_w). Regression obtained for the total surface area, $A_{max}=94 \text{ cm}^{-1}$.

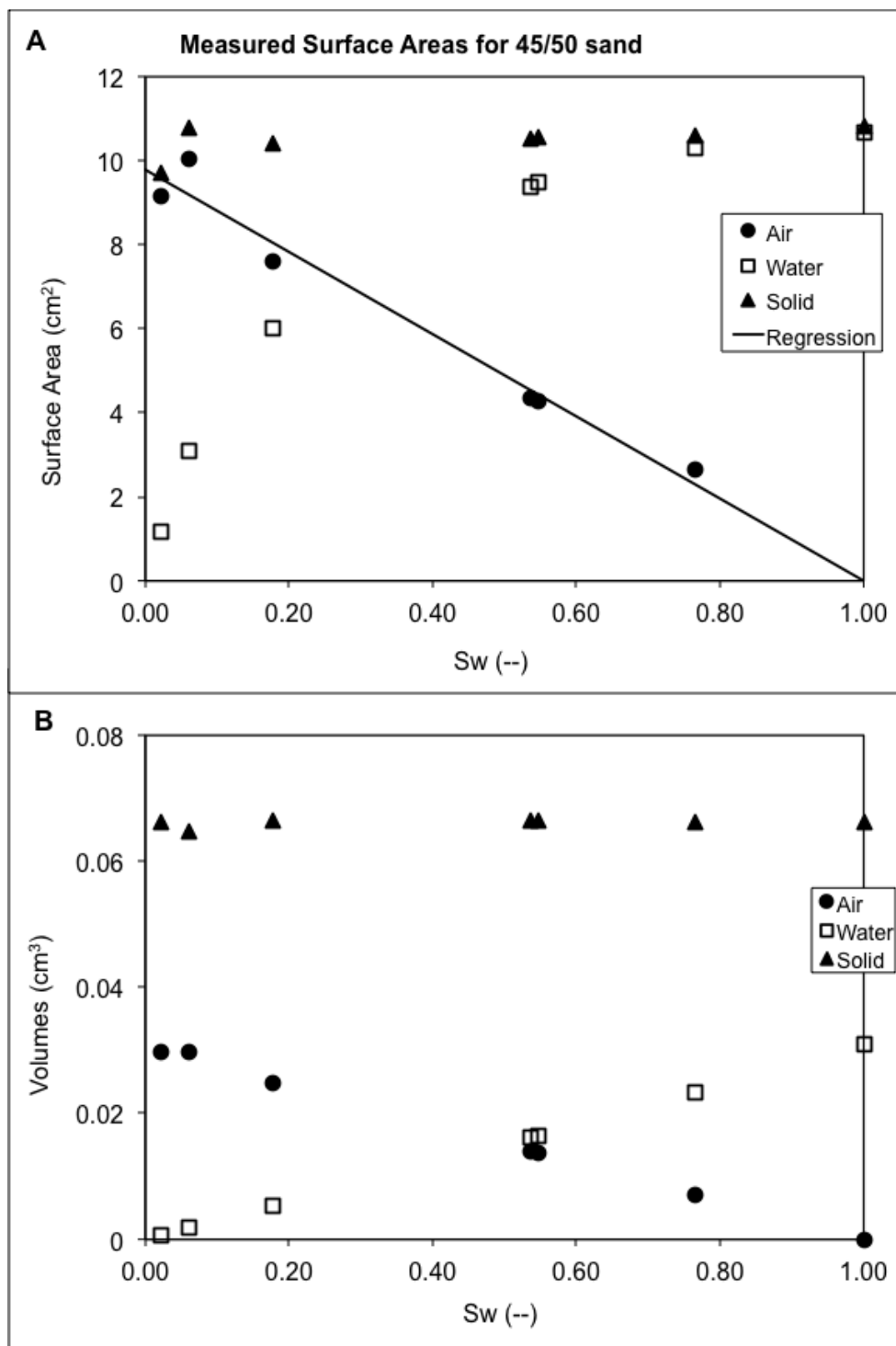


Figure 3: A. Example of surface areas of air, water, solid, Capillary (C_{aw}), and measured fluid-fluid (I_{a-w}) surface areas as a function of water saturation for 45-50 sand. Regression obtained for the total surface area, $A_{max}=101 \text{ cm}^{-1}$. B. Corresponding phase volumes.

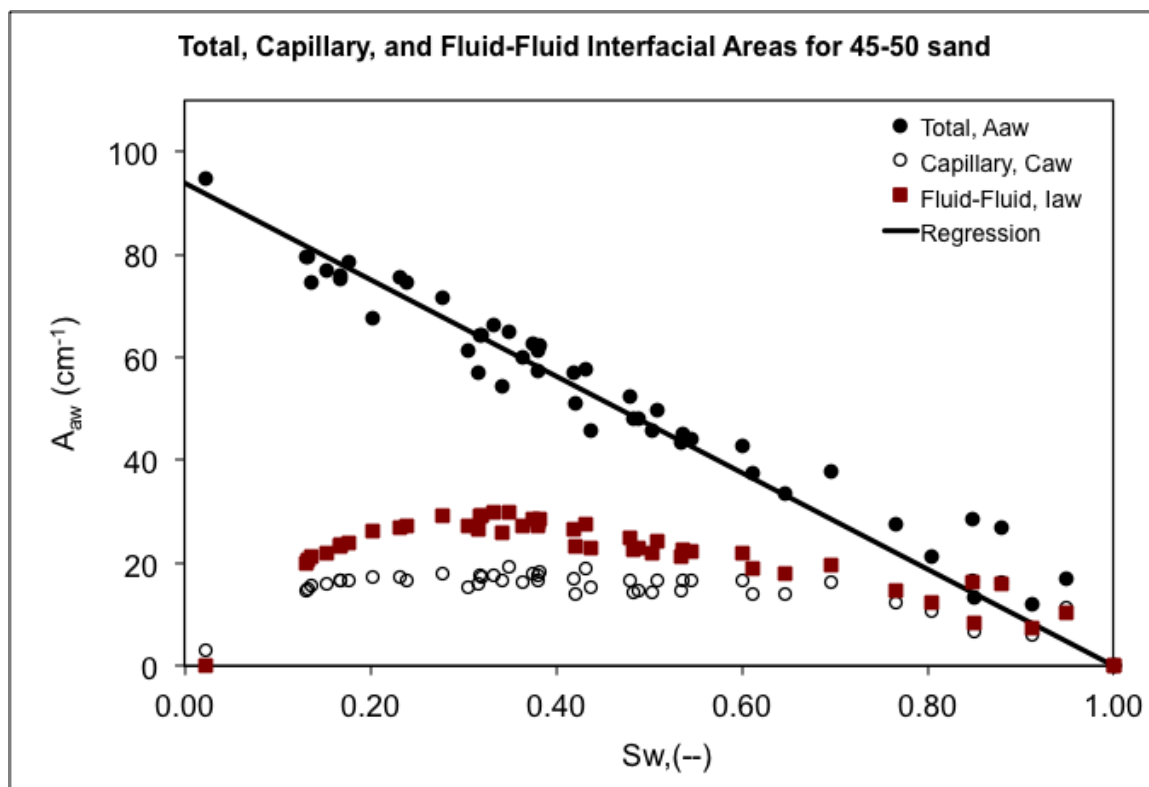


Figure 4: Total (A_{aw}), Capillary (C_{aw}), and fluid-fluid (I_{a-w}) interfacial areas as a function of water saturation. Regression obtained for the total specific surface area for all data sets.

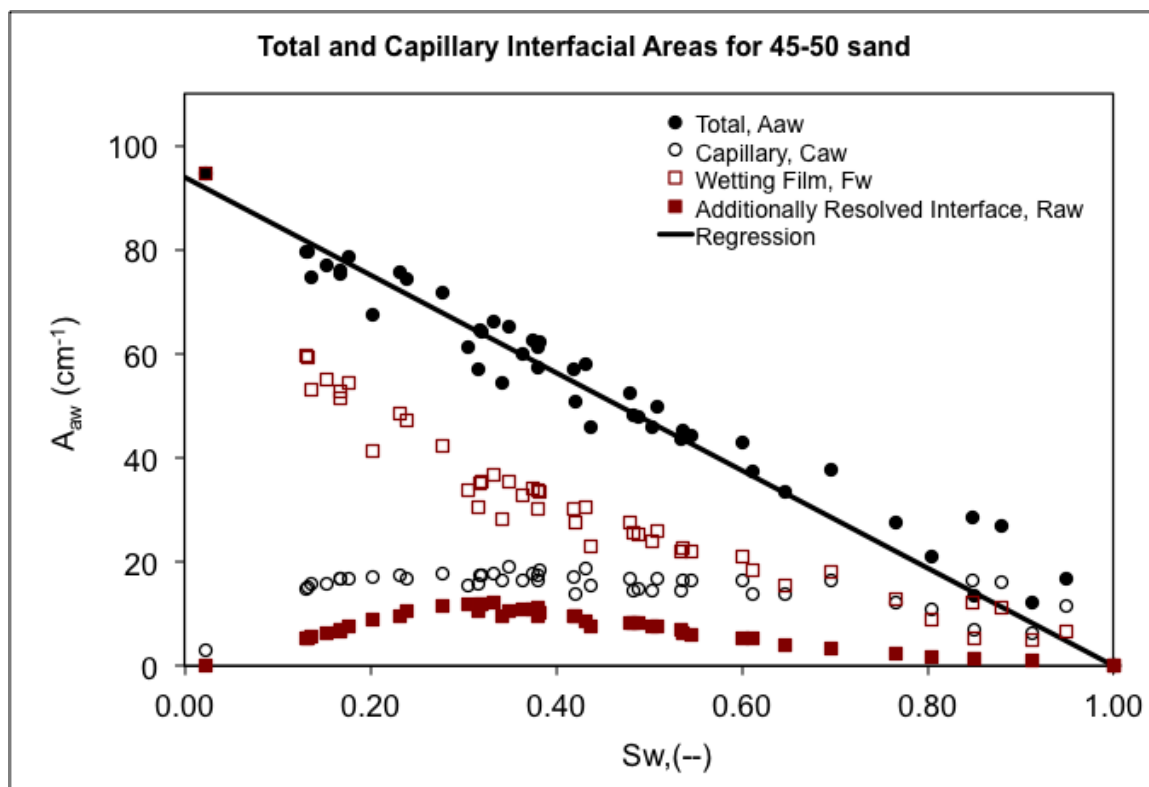


Figure 5: Defined interfacial areas as a function of water saturation. Regression obtained for the total specific interfacial area for all data sets.

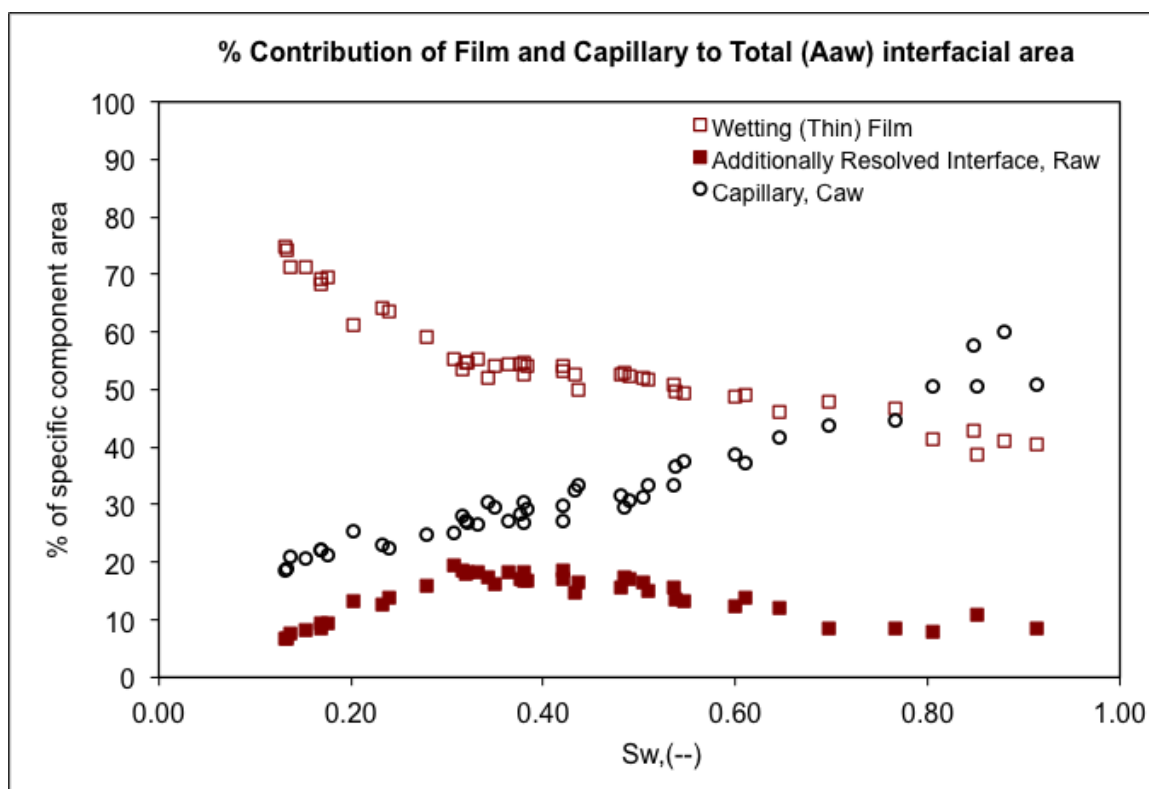


Figure 6: Percentage contribution of each capillary (C_{aw}), thin wetting films (F_w) and additionally resolved interfacial domains, (R_{aw}) to the total air-water interfacial area (A_{aw}).

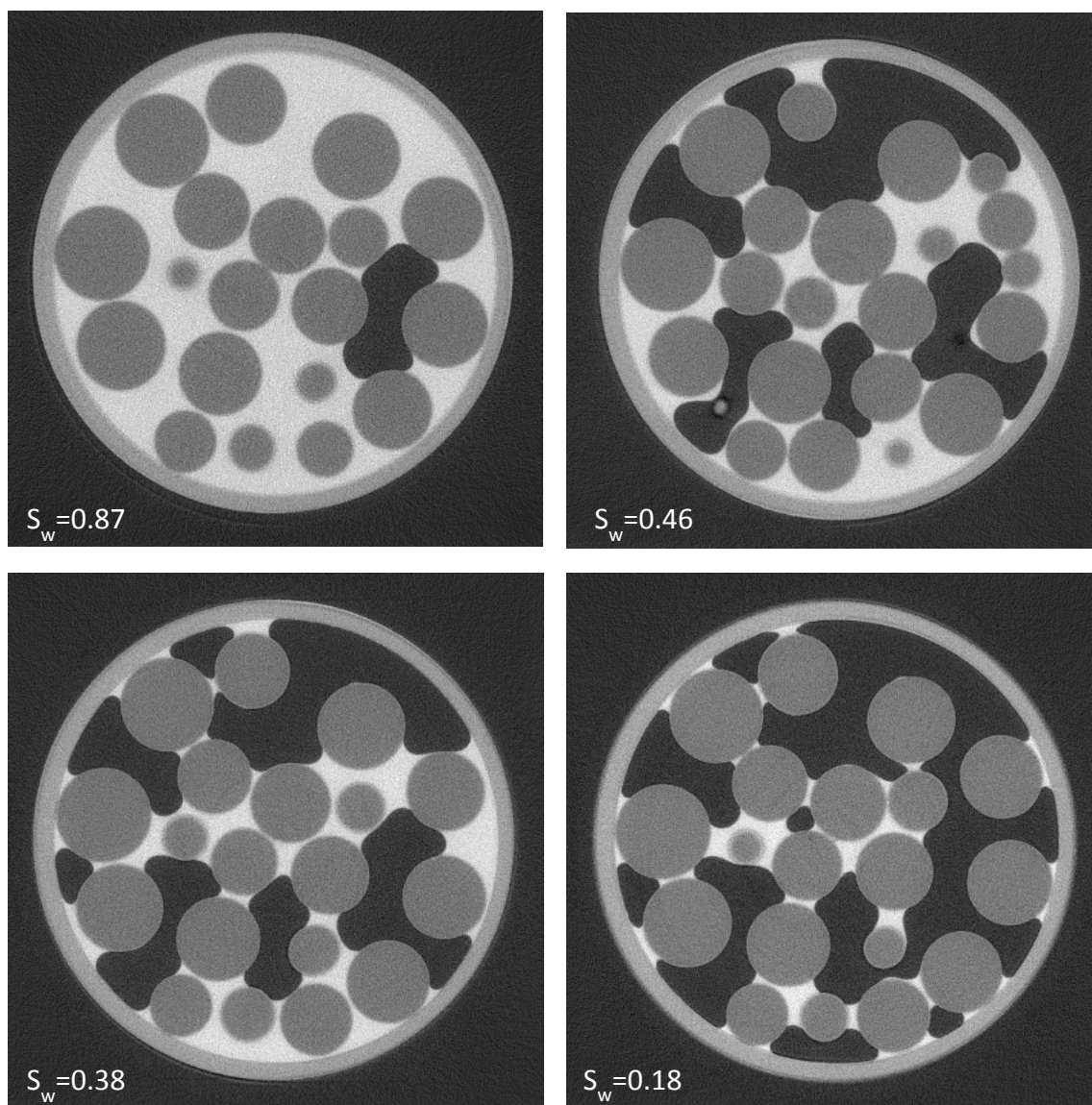


Figure 7: Glass Beads sample images. Imaged at GSECars (BMD 13) at 33.369 KeV (above iodine edge). Air is black, water is white, and solids are grey.

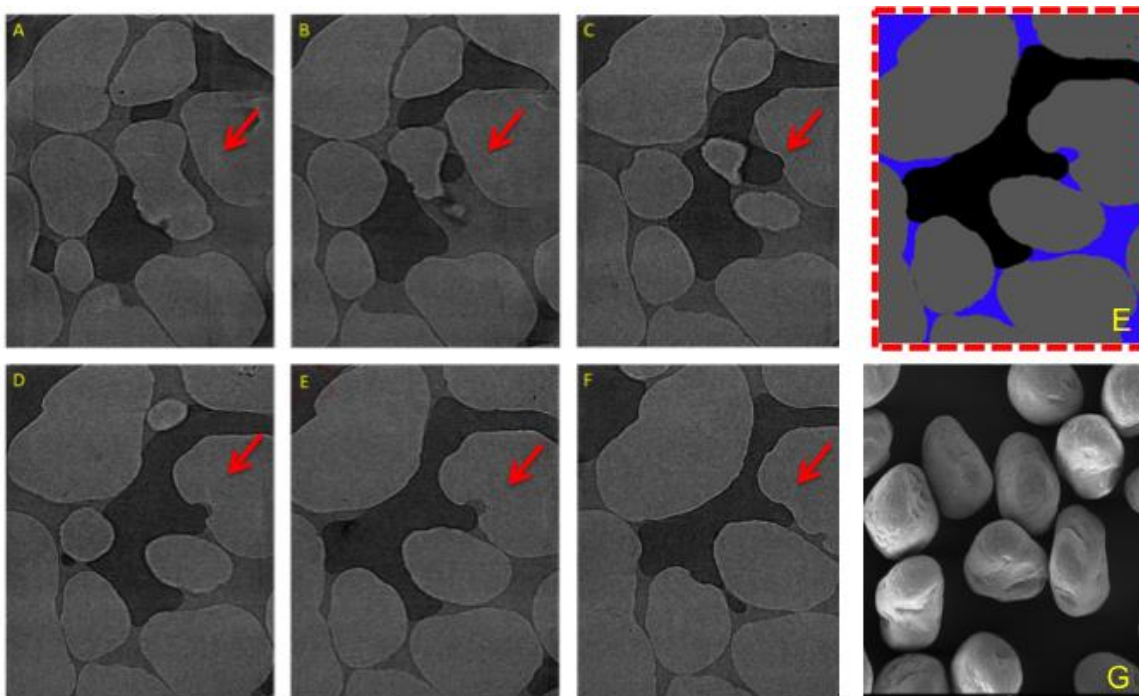


Figure 8: 45-50 sand. Greyscale $1\mu\text{m}$ image (GSECars) taken after complete drainage set, $S_w \approx 0.2$. **A-F** sequence entering the column from z-y plane, perpendicular to the column wall. **A.** Disconnected air bodies. **B.** Increased connectivity of air bodies, and partial hidden solid grain. **C.** The air phase residing in separate pores are now connected. Note an indentation appears on right-most middle grain. **D.** Indentation is now filled with water forming a pond on the surface of the grain. **E.** Grain crevice “pit”, false color overlay. **F.** Air phase further invades the pore space, and new solid configuration appears. **G.** Independent Scanning-Electron Microscopy (SEM) image, ($200\ \mu\text{m}$) for n Accusand.

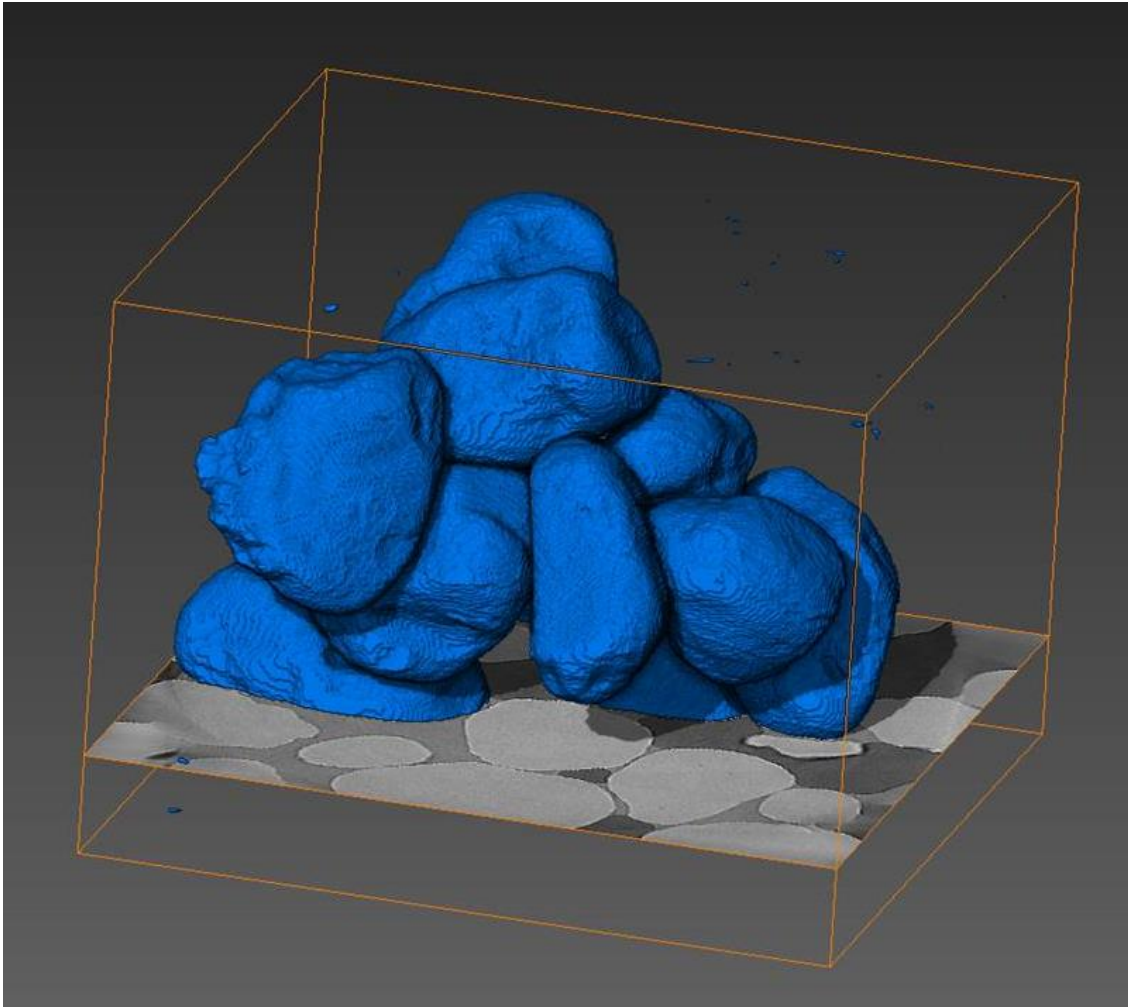


Figure 9: 3D representation of 1- μm image (GSECARS) taken after completed drainage experiment, $S_w \approx 0.2$. Visualization courtesy of Dr. Ming Lei (FEI Visualization Sciences Group).

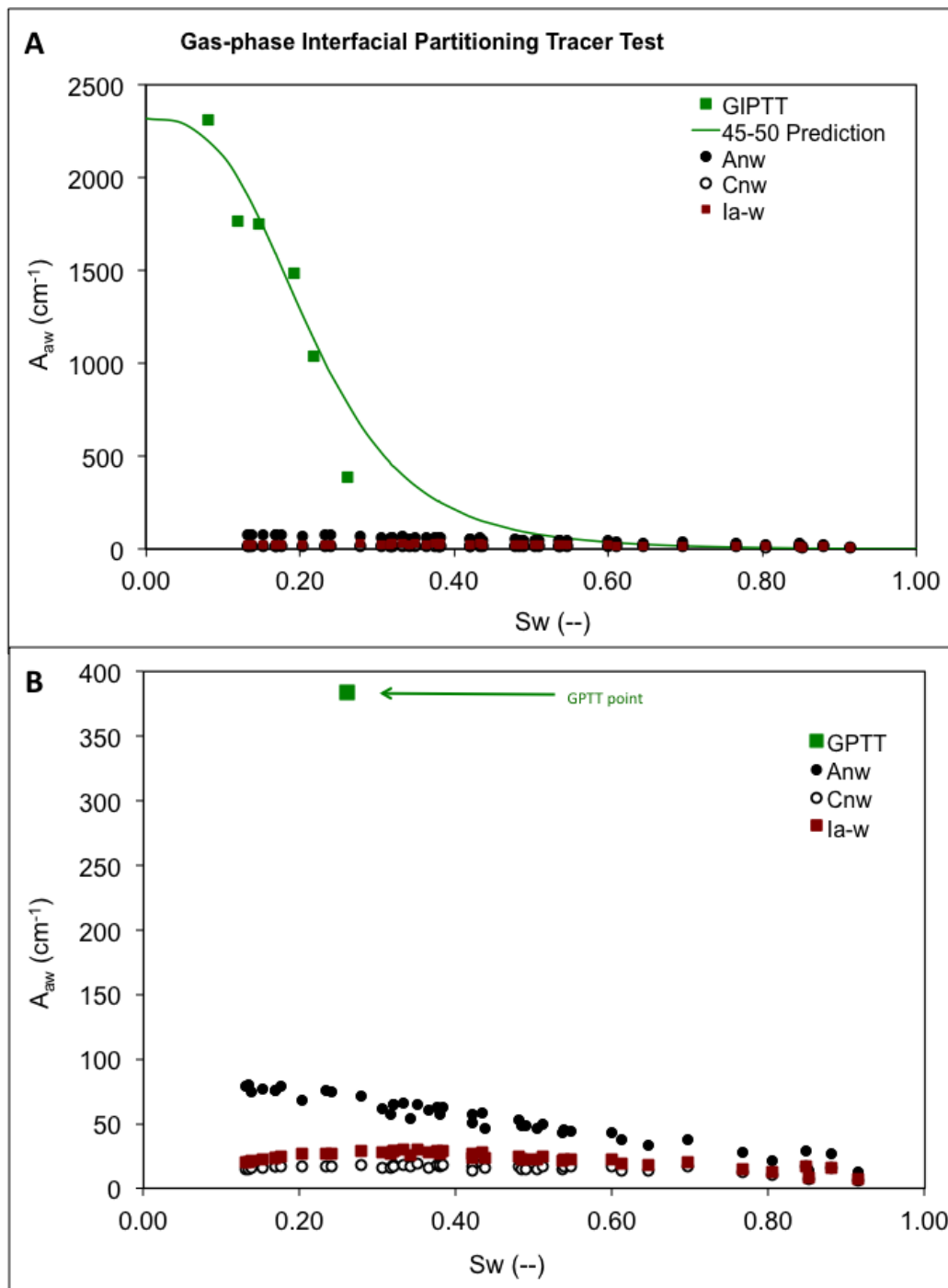


Figure 10: Comparison between microtomography and gas-phase maximum measured interfacial area. **A.** Full scale GPTT data. **B.** Total air-water interfacial area (A_{aw}), capillary (C_{aw}), and fluid-fluid (I_{a-w}) shown to illustrate difference in magnitude. *note prediction adjusted for 45-50 sand characteristics. GPTT data and predicted model based on 40-50 sand from Peng and Brusseau (2005).

APPENDIX E

COMPARISON OF TRACER-BASED METHODS FOR MEASURING AIR-WATER INTERFACIAL AREA IN POROUS MEDIA

1. INTRODUCTION

There are multiple disciplines that necessitate the understanding of fluid flow in multiphase systems. In some instances, measurements of hydraulic parameters at the laboratory scale are needed either as model inputs or to further predict fluid flow through geological material. There have been several publications highlighting the need for including the fluid-fluid interfacial areas to models to date, specifically to those which seek to characterize fluid flow and mechanisms occurring at the pore scale, (e.g. Skop 1985; Hassanizadeh and Gray, 1993; Gvirtzman and Roberts 1991; Reeves and Celia 1996; Celia et al., 1998; Kawanishi et al., 1998). These fluid-fluid interfacial areas are manifestations of pore-scale distribution of fluids in the porous medium (e.g., Brusseau et al., 2007). The distribution of fluids occurs naturally in the ecosystem, in the vadoze zone. This region is of key importance for contaminant transport, as it serves as, in effect, a filter between the surface, the first point of entry of environmental pollutants, and the saturated zone where fresh drinking water is commonly located.

There are only two primary methods available to measure fluid-fluid interfacial areas for porous media systems: imaging methods involving microtomography and partitioning interfacial tracer tests. This chapter is focused on the latter method. Interfacial partitioning tracer tests (IPTT) are useful for applications where knowledge of retention, mass transfer, and transformation processes are needed. This category of

measurements involves tests whereby a fluid containing a tracer that partitions to the non-wetting/wetting fluid interface is injected into the porous medium. The retention behavior of the tracer is measured and used to determine the interfacial area present in the system. The interfacial areas estimated in this manner are considered to represent the effective total air-water interfacial area (A_{aw}). The total air-water interface includes the capillary and film-associated interfacial areas at target saturation. Measurements obtained with tracer-based methods may be influenced by accessibility of some interfaces to the tracers of choice, sorption by the solid phase, and impact of the tracer on fluid configuration (e.g. Kim et al., 1997, 1999, 2006; Anwar et al., 2000; Schaefer et al. 2000; Brusseau and Srivastava, 1997; Costanza-Robinson and Brusseau, 2003; Brusseau et al., 2007).

There are several ways by which to implement an interfacial partitioning tracer test. Karkare and Fort (1996) proposed a method for experimentally determining the air-water interface in unsaturated porous media. Their method was based on establishing a critical surfactant concentration necessary to induce water movement. Soon after, Silverstein and Fort (1997) performed similar experiments and developed a simple model to investigate behavior in air-water systems. Anwar et al. (2000) and Schaefer et al. (2000) reported on a mass balance method to measure interfacial areas in simple porous media using surfactant sorption properties at different interfaces in the system. Kim et al. (1997, 1999, 2006), Saripalli et al., (1997), Brusseau et al. (2007), and El Ouni (2013) among others report on methodology using an aqueous interfacial tracer solution in miscible-displacement experiments to correlate retardation obtained from a breakthrough curve to interfacial areas. This technique can also be used with gas-phase interfacial

tracers (e.g. Brusseau et al., 1997, 2006; Peng and Brusseau, 2005a, 2005b; Costanza-Robinson and Brusseau, 2002a, 2002b, 2006; Sung and Chen, 2011).

The miscible-displacement method is based on the injection of a partitioning tracer solution into a column packed with a partially saturated porous medium to displace the existing wetting phase in the pores. The tracer will accumulate at the fluid-fluid and fluid-solid interfaces, thus retarding the transport of the surfactant solution through the porous media. This method relies on the correlation between the retardation factor obtained from breakthrough curves and the air-water interfacial area. Henry and Smith (2002), Karkare et al. (1993); Karkare and Fort (1994, 1996) reported on induced drainage caused by surface-active solutes. Costanza et al. (2012) conducted miscible-displacement surfactant tracer tests and concluded that changes in surface tension caused by the injection of surfactant induced drainage and thus complicated the determination of water contents. Similar conclusions were also observed by (Kibbey and Chen, 2012; Kibbey, 2013). Changes in interfacial tension are speculated to change configuration of fluid-fluid interfaces thereby affecting interfacial area measurements. However, Brusseau et al. (2007) conducted surfactant tracer tests using the miscible-displacement method and did not observe significant drainage effects. This was accomplished through the use of a strong vacuum system to maintain constant flow.

The mass balance method (MB) is based on the concentration gradient that forms when two fluids are in contact with each other. When these two phases are liquid, the concentration profile is postulated to span many molecular diameters (e.g. Anwar et al., 2000). In general interfacial tracers will partition to the air-water interface, solid-water

interface, while some will remain in the aqueous phase. This method is posited to provide a direct measurement of total surfactant mass in the system directly for a range of saturations. Schaefer et al. (2000), Anwar et al. (2000), Chen and Kibbey (2006) have reported on experiments using this mass balance approach. The governing principle to the mass balance approach is to allow the column sufficient time for the interfacial tracer (surfactant) solution to achieve concentration equilibrium through recirculation (e.g. Anwar et al., 2000) or through diffusive mass transfer (e.g. Schaefer et al., 2000). These measurements should not be subjected to surfactant-induced drainage effects.

Measurements using aqueous tracers are considered to underrepresent the interfacial area, due to limited accessibility of the surfactant solution to pore regions that are not contributing to advective flow. These regions may to some extent be accessed through diffusive processes. Conversely, when this technique is used with gas-phase tracers, almost all available interfaces are accessible. Although much research has been conducted to measure the air-water interface, there is still no clear evidence that the methods yield consistent information. Brusseau and colleagues (i.e. Brusseau et al., 2007; Costanza-Robinson and Brusseau 2002a, 2002b) evaluated the various interfacial partitioning tracer test methods and proposed that different methods measure different domains. Kibbey and Chen (2012) more recently similarly suggested that the vast majority of studies vary fundamentally in terms of types of tracers used and how various tracers interacts with the interfaces. These factors complicate comparisons between each method, particularly at different water saturations. Sung et al. (2010) tested aliphatic alcohol as a potential gaseous interfacial tracer. They concluded that the gas-phase

miscible displacement test yields results closest to the true interfacial area at low saturations, consistent with the prior results reported by Brusseau and colleagues (Brusseau et al., 1997, 2006, 2007; Costanza-Robinson and Brusseau 2002; Peng and Brusseau, 2005).

In this study we will focus on aqueous-phase interfacial tracer tests. The air-water interfacial area is measured as a function of water saturation for a natural porous medium using (a) modified aqueous-phase interfacial partitioning tracer tests (IPTT), and (b) surfactant mass balance method (MB). The objective is to evaluate the features inherent in each method, and their overall measurements of air-water interfacial area in the system. Results are compared to interfacial partitioning tracer test measurements from the literature. Gas-phase tracer tests are presented here for reference, because it is the closest measurement to the true total surface area in a system.

2. MATERIALS AND METHODS

2.1 Sodium Dodecylbenzene Sulfonate (SDBS) Surfactant

A surfactant is an organic compound that lowers the interfacial tension between two fluids, or that between a fluid and a solid phase. The surface-active agent was chosen to be sodium dodecylbenzene sulfonate (SDBS) (>95% purity, Tokyo Kasei Kogyo, Japan). The SDBS molecule is depicted in Figure 1 is comprised of a hydrophilic head, and a hydrophobic tail. The hydrophilic portion may ionize in aqueous solutions (cations, anionic) or remain un-ionized (non-ionic). The hydrophobic part of a surfactant is

generally the hydrocarbon moiety containing several carbon chains (e.g. Tanford, 1974)

When present in solution at a sufficient concentration the individual surfactant molecules will form micelles. The concentration at which molecules begin to aggregate is known as the Critical Micelle Concentration (CMC). The micelles form in such a way that the hydrophobic portion (lipophilic) is inside, and the hydrophilic groups outside, protecting the hydrophobic core. This allows for the micelles to be soluble in water. The shape of the micelles is dependent on the nature of the surfactant, and the ratio between the hydrophilic–lipophilic balance (HLB). The higher the HLB the more water-soluble is the micelle (i.e. Tanford, 1974; Brusseau 1999). The CMC of SDBS is ~414 mg/l (e.g. Anwar et al., 2000).

2.1.1 SDBS Concentration Measurement

The SDBS solution used was approximately 35 mg/L in 0.01M NaCl, following the protocol described in Brusseau et al. (1997) for all experiments. This concentration is well below the 414 mg/l CMC value. A calibration curve was measured using a UV-Vis Spectrophotometer (Shimadzu model 1601) measured at wavelength of 223 nm for various concentrations of SDBS prepared in 0.01 M NaCl (Figure 2). Additional SDBS solutions were prepared using water and 2-d propanol. The propanol is added to soil samples during the SDBS extraction procedure for Mass Balance (MB) experiments. These solutions were tested to confirm that the propanol does not significantly alter the absorption spectrum previously used. At such low electrolyte concentrations, the slope of the standard curve was not significantly altered.

2.2 Interfacial Partitioning Tracer Test (IPTT)

Breakthrough curves for SDBS are obtained using miscible displacement experiments and key parameters are obtained using statistical moment analysis. The transport of solutes is described by equation 1. This equation is derived from advection-dispersion equation (e.g. Freeze and Cheery 1979; Bear 1988) to account for the change in total solute mass of the system.

$$\frac{\partial M_T}{\partial t} = -q \cdot \frac{\partial C}{\partial x} + D \cdot \theta \cdot \frac{\partial^2 C}{\partial x^2} \quad (1)$$

$$M_T = (C \cdot \theta) + (\rho_b \cdot S) + (A_{a-w} \cdot \Gamma) \quad (2)$$

where D is the coefficient of dispersion (L^2/T), θ is volumetric water content (vol./vol.), S is the mass of contaminant per mass of solid, and C is the aqueous-phase concentration (mass/volume), ρ_b is bulk density (mass/volume), and q is Darcy's velocity (L/time). The total mass in the system (M_T) is the contribution of solute residing in solution, or bulk fluid ($C \cdot \theta$), the mass of tracer sorbed per volume of porous media ($\rho_b \cdot S$), and the mass of tracer which accumulated at the air-water interface, ($A_{a-w} \cdot \Gamma$), where (A_{a-w}) is the specific area of the interface, and Γ represents the surface excess of molecules at the interface, (or adsorption density).

2.2.1. Sorption Coefficient, K_d

The distribution of solutes between the solid and aqueous-phase concentration is quantified by a linear isotherm (equation 3), where K_d represents the sorption coefficient (cm^3/g):

$$S=K_D \cdot C \quad (3)$$

2.2.2 Surface Excess Concentration (Γ) and K_i Isotherm

The surface excess concentration Γ (m/L^2) is related to aqueous phase concentration (C) using the adsorption isotherm (equation 4), where K_i represents the partitioning interfacial coefficient (units).

$$\Gamma = -\frac{1}{RT} \cdot \frac{\partial \gamma}{\partial C} = K_i \cdot C \quad (4)$$

Note that this definition is established by measurements of the surface tension (γ) to establish the interfacial partitioning coefficient (K_i). Values estimated in this manner vary throughout surfactant concentrations, and it is non-linear. However, a linear relationship is assumed within a narrow concentration range.

2.2.3 Retardation Factor, (R)

Extensive research have shown that when a contaminant adheres to the solid phase, the transport behavior will change because of the added retention to the porous media. In most cases, this will cause the solute to traverse slower than water would

through the porous media. The retention of contaminants also occurs at the air-water interface when surface-active compounds accumulate at the fluid-fluid interface. Equation 5 is re-written in non-dimensional terms, for 1 dimensional, steady state fluid flow with the incorporation of sorption onto solid phase (K_d) and at air-water interface (K_i).

$$\frac{\partial C}{\partial t} \cdot \left(1 + \frac{\rho_{\text{bulk}} \cdot K_D}{\theta} + \frac{K_i \cdot A_{\text{aw}}}{\theta} \right) = -v \cdot \frac{\partial C}{\partial x} + D \cdot \frac{\partial^2 C}{\partial x^2} \quad (5)$$

The retardation factor, R is defined by equation 6. From this equation, we are able to calculate the air-water interfacial area (A_{aw}) from miscible-displacement experiments. It is the governing equation for the aqueous-phase tracer tests (IPTT) presented in this study.

$$R = 1 + \frac{\rho_{\text{bulk}} \cdot K_d}{\theta} + \frac{A_{\text{aw}} \cdot K_i}{\theta} \quad (6)$$

2.3 Surfactant Mass Balance

The basis of this method is in establishing an equilibrium concentration within the porous media. Equilibrium is achieved by recirculating the interfacial tracer solution through the porous medium while simultaneously creating a water content profile. The total mass of surfactant is extracted from each ring of the column. Thus, the mass of surfactant adsorbed to the different available surfaces (i.e. fluid-fluid interface, fluid-solid) and present in solution is determined, and the air-water interfacial area is calculated from equation (7). In theory, equilibrium concentrations in the bulk fluid will be a direct representation of the concentrations within the column. This method is meant to alleviate

the possibility of induced drainage that occurs when a surfactant solution is first injected into the system (e.g. Anwar et al., 2000); Schaefer et al., 2000).

The total mass in the system (M_T) is the sum of the mass of tracer in solution (M_w), the mass of tracer sorbed by the porous media (M_{s-w}), and the mass of tracer accumulated at the air-water interface (M_{a-w}). Under equilibrium conditions, (M_T) is defined by equation (7).

$$M_T = M_w + M_{a-w} + M_{s-w} = CV_w + \Gamma_{a-w} a_{a-w} + \Gamma_{s-w} a_{s-w} \quad (7)$$

where subscripts w , a , s denote water, air, and solid phase respectively; C represents the aqueous phase concentration (mol/cm³); R is the gas constant (erg/mol °K); Γ surface excess (mol/cm²); γ is the surface tension (dyn/cm). In the Gibbs adsorption model the interfacial area is calculated using surfactants, which will adhere to the air-water interface, after equilibrium is established. It is assumed that the surfactant does not partition into the non-wetting phase (e.g. Adamson, 1982; Saripalli et al., 1997; Schaefer et al., 2000).

2.4 Surface Tension Measurement (γ)

A series of SDBS solutions were prepared in 0.01 M of NaCl, ranging between 15-105 mg/L. This concentration range was chosen based on the concentrations used in the tracer experiments presented herein. The surface tension (for soluble substances) or interfacial tension (between insoluble substances such as oil-water systems) was

measured by a Surface Tensionmat (Fisher Scientific, model 21) using the ring method. The ring method determines the force required to detach the wire loop (i.e. ring) from the surface of a liquid (Adamson 1982).

The surface Tensionmat is comprised of a torsion wire balance with a manual dial, attached to a platinum-iridium ring, and a mobile sample stage. Each sample was transferred into a 50 ml beaker. Once the sample is placed inside, onto the mobile stage, the knob controlling the torsion arm is loosened to bring the vernier scale to a point well below the expected reading. This process aligns the reading dial with a reference point in the mirror located inside the instrument. Slowly, the platinum-iridium loop is lifted out of solution, until the surface or interface film ruptures. As the critical point of detachment nears, it is vital to ensure that there are no disturbances to the surface. When the surface or interface film ruptures, the tension value (dynes/cm) is read and recorded (Adamson 1982). More details can be found in Zuidema and Waters (1941) and Tensionmat instruction manual.

The surface tension of Nanopure water was measured prior to each set of surfactant reading to ensure that the instrument was calibrated. Three replicate readings were recorded and averaged for each concentration sample. After each sample, the ring was washed with distilled water and then dipped in acetone. A Bunsen burner was also used after each few samples to clear any salt impurities that may have accumulated onto the ring. Table 1 lists the recorded values.

The absolute surface tension value from the scale requires a correction factor (F). This correction is determined by the size of the ring, the size of the wire used to hold the

ring, and fluid densities. Adapted from the Tensionmat Manual, the correction factor is described by equation 8. P is the recorded dial reading (dyn/cm), D is the density of the lower phase, d the density of the upper phase in (g/cm^3), C is the circumference of the ring (cm), R is the radius of the ring loop, and r is the radius of the wire holding the loop (cm). Table 1 shows the values of recorded tension readings, correction factors and final absolute surface tension (γ) values.

$$F = 0.7250 + \sqrt{\frac{0.01452P}{C^2 * (D - d)} + 0.04534 - \frac{1.679r}{R}} \quad (8)$$

The total adsorbed amount of surfactant per unit volume of porous media is a function of surface excess, (Γ), and interfacial tension (γ). This non-linear relationship is defined by Gibbs surface adsorption equation (4) (e.g. Adamson 1982). The interfacial partitioning coefficient, K_i , is a function of surfactant concentration, and surface tension (γ). The relationship between bulk surfactant concentration (C , mg/L) and surface tension (γ , dyn/cm) is converted to a surface adsorption isotherm using Gibbs surface adsorption equation (9) (e.g. Adamson 1982).

$$\partial\gamma = -RT \cdot \Gamma \cdot \partial \ln C \quad (9)$$

2.5. Aqueous-Phase Interfacial Tracer Experiments

The standard IPTT test is conducted under unsaturated conditions, thus requiring constant pressure head to maintain steady state flow and uniform water content (e.g. Brusseau et al., 2007; El Ouni, 2013). The standard aqueous IPTT approach is modified such that the tests are conducted using saturated flow conditions. The modified tracer test (IPTT) procedure in this work is a variation of the standard method, whereby creating a residual air content allows for, in effect, saturated flow conditions for the experiment. By definition the air phase is immobile and connected to bulk water phase, where surfactant movement can occur. This approach is the standard method used for non-aqueous phase liquid (NAPL) experiments (e.g. Brusseau et al., 2008, 2010; Narter and Brusseau, 2010). Results from these studies suggest that this approach does not alter fluid configuration in the system (Brusseau et al., 2008). In all of these methods however, there is still a possibility that the initial surfactant injection can still alter the fluid configuration due to changes in interfacial tension.

2.5.1 Miscible-Displacement Experiment Preparation

Vinton soil was chosen as the porous medium for this set of experiments. Its characteristics are listed in Table 2. A glass chromatography column $L=15$ cm, $d_{in}=2.5$ cm, packed with the porous medium and conditioned with 0.01 M NaCl background solution for approximately 72 hours to ensure full saturation at $Q=0.01$ ml/min. Once saturation was achieved, the column was drained from the bottom, and the top open to the atmosphere. It was then imbibed with 0.01 NaCl to trap air bubbles at $Q=1$ ml/min. The

column was again allowed to condition for at least 48 hours to ensure homogeneous condition.

A non-reactive tracer experiment was conducted once a steady-state flow condition was established. Approximately 1 pore volume of PFBA (pentafluorobenzoic acid) (10mM) is injected and subsequently flushed with background solution. Next, several pore volumes of SDBS solution (~35 mg/L) is injected at $Q=0.65$ ml/min into the column, and flushed with the background solution to obtain a full breakthrough curve. The experimental flow rate was chosen to ensure similar flux conditions as reported by (Brusseau et al., 2007). After the experiment, the column was segmented into five sections. The weight of each soil sample was recorded before and after they were placed in the oven for at least 48 hours. These measurements were used to determine the water content variability in the column. The water content represents the water volume present in the entire column. It is also another measurement of pore volume, an important parameter in our calculations.

The next set of experiments was conducted to measure only the arrival portion of the breakthrough curve (BTC). In these experiments (SDBS 4-9), the glass column was dry-packed and saturated at a high flow rate, $Q=1.00$ ml/min. In this case, the outlet is in the bottom of the column, and connected directly to the fraction collector. Once the air bubbles have been trapped, the column was conditioned. The column weight was measured periodically to ensure stable water content. The effective flow rate used in our calculations was measured by weighing the volumes of sample collected. The saturated pore volume, or volume of liquid-filled pores used in the calculations are based on the

bulk density of the soil pack, since we did not completely saturate the column. The values are consistent with those from previous experiments where the *effective* pore volume is dependent of water content.

An additional two sets of experiments (SDBS 8-9) were conducted in fully saturated conditions, to measure the sorption coefficient (K_d). In this particular experiment (SDBS 8-9), the columns were wet-packed and conditioned with background electrolyte solution (0.01M NaCl) to eliminate possible air bubbles at $Q=0.65$ ml/min. All experimental conditions were kept the same to ensure consistency. The saturated column was weighted periodically during conditioning period. The mean value for Vinton soil used for all calculations reported herein is $0.5 \text{ cm}^3/\text{g}$. Similar values for Vinton soil were reported by Brusseau et al. (2007), El Ouni (2013).

2.5.2 Miscible-Displacement Experiment—Data Extraction and Moment Analysis

Moment analysis is a statistical descriptor for solute breakthrough curve (BTC) at a given location (e.g. outlet). The basic temporal moment is described by equation 10;

$$M_n = \int_0^n C t^n dt = \sum C t^n \Delta t \quad (10)$$

where C is the aqueous-phase concentration. The zeroth moment ($n=0$) represents the total mass in the system. It is the integrated area under the curve. The first moment describes the mean location of center of the solute mass. By normalizing the first moment, $M'_1 = M_1/M_0$ one obtains the arrival time of the solute.

Particular to the context of this work, retardation of surfactant tracer occurs due to sorption to the air-water interfacial area. The total fluid-fluid interfacial area (A_{aw}) present in the system (equation 2), is calculated using the retardation factor (R) obtained from the breakthrough curve data from the IPTT experiments. The retardation factor is calculated using equation 11, where M'_1 is the normalized first moment, M_0 is the zeroth moment, and T_0 is the injection time or input length.

$$R = \frac{M'_1}{M_0} - \frac{1}{2} \cdot T_0 \quad (11)$$

In the case of experiments 5-9, where only the arrival wave (half breakthrough curve) was measured, R is estimated by integrating the area to the left of the tracer test instead. In such cases, R is equivalent to the volume of tracer left in the chromatography column, or area above the tracer curve.

2.5.3 Mass-Balance Experiments (MB)

Experiments were conducted using 45-50 Accusand and Vinton soil (Table 2), for comparison to the interfacial partitioning tracer test (IPTT) results. The column is composed of several rings, 1.5 cm in length and 2.8 cm in diameter, with a special 5 cm in length bottom ring. A total of 20 rings were used with the exception of MB1, which comprised of only 12 rings. Figure 3 shows a picture of the ring column after an experiment with Vinton soil.

The column was packed with sand, saturated with a SDBS solution of ~35 mg/L with a recirculation system based on Anwar et al. (2000). A flow rate of 0.5 ml/min was initially used to equilibrate the column. The flow rate was lowered decreasing the flow rate every 2 hours by 0.5 ml/min. The flow rate change interval was switched to smaller intervals until a final flow rate of 2 ml/min was achieved. The top of the column was open to the air. The bottom two rings were intended to serve as the control rings, the saturated rings from which a working sorption coefficient K_d could be measured. The first bottom ring served to support the rest of the column. It connects to a plate containing the capillary filter, which also holds the soil in the column. A solution tube is attached at the bottom of the plate and connected to the reservoir for drainage and recirculation of surfactant solution throughout the column. The column was allowed to rest for 7 days after drainage, to ensure equilibrium. The drainage procedure is adapted from a combination of procedures described by Kim et al. (1997); Anwar et al. (2000), Schaefer et al. (2000). For the poorly sorted Vinton soil, the drainage procedure was lengthier, and required greater pressure gradient and equilibrium time (approximately 14 days).

After the experiment, each ring was carefully taken from the column, in a quick slicing manner and placed into a pre-weighed beaker. The beaker and its contents were weighed. For the surfactant extraction, approximately 20 ml of 2-d Propanol was added to the beaker, and the weight of beaker and its contents were measured again. The amount of propanol used was sufficient to cover the sample and generate adequate supernatant volume for UV-analysis. Quickly, the sample was stirred, and the supernatant drained into 50 ml falcon tubes. These tubes were sealed and placed on a shaker table for

3-4 hours. Prior to the surfactant analysis, the sample was allowed settling (resting) time to ensure that a clear fluid was available for the UV-vis Spectrophotometer analysis (section 2.1), with the soil particles settling on the bottom. Meanwhile, the rings were removed from the beakers, and the weight with soil sample was recorded before and after they were placed in the oven for at least 48 hours. These measurements were used to determine the water content for each ring throughout the column.

2.5.4 Mass Balance Method Data Analysis

The total mass of surfactant (M_T) is the mass of SDBS extracted from each individual ring. The aqueous bulk fluid SDBS concentration is obtained from the final equilibrated SDBS solution concentration and the mass of solution extracted per ring ($C \cdot \theta$). Next, the mass sorbed on the solid, (M_{sw}) is obtained from the saturated ring. If the ring is saturated, it follows that there is no air-water interface present in the system. Thus, the difference between M_T and M_w gives the mass of surfactant per dry solid mass, or S . The air-water interface (M_{aw}) is obtained per equation 7. The surface excess, or Γ is obtained by using the adsorption isotherm, (equation 4), where $\Gamma = K_i \cdot C$.

The K_i used for calculation of surface excess is based on (a) measured values using a range of SDBS concentrations in 0.01 NaCl (electrolyte background solution), values shown in Figure 4, and (b) compiled values from Schaefer et al. (2000) and Anwar et al. (2000). These values were put all together and fitted for a general interfacial tension equation (Figure 5, 6).

3. RESULTS & DISCUSSION

3.1 Interfacial Tension Coefficient (K_i) and Interfacial Tension (γ)

Figure 7 shows the measured interfacial tension results combined with literature values reported by (Kim et al. 1997; Schaefer et al., 2000, and Anwar et al., 2000) using similar electrolyte concentrations. The derivative of the regression line (shown in Figure 5) represents the highly non-linear relationship between surface tension (γ) and bulk surfactant aqueous-phase concentration. The slope (or derivative) is the input variable for Gibbs surface isotherm used to calculate K_i (Saripalli et al. (1997). The interfacial-partitioning coefficient (K_i) is calculated based on the linear regression of all aggregate data (not including the Kim et al. data set) in Figure 6. The measured surface tension values from regression line (Figure 6) are only valid for surfactant concentrations smaller than the CMC of 400-414 mg/L (e.g. Kim et al., 1997; Schaefer et al., 2000) where the relationship is linear on a semi-log plot (Figure 6).

When using equation 7 for mass-balance experiments air-water interfacial area (A_{aw}) calculations, K_i is a function of the equilibrated (final) surfactant concentration and surface excess surfactant concentration. This differs from IPTT experiments where the interfacial partition coefficient (K_i) is based on the concentration of surfactant in the injected solution, and specific A_{aw} is obtained indirectly (equation 6), using measured retardation factor (R) from the breakthrough curve data (equation).

The average K_i for obtained from residual-IPTT experiments is 2.99×10^{-3} cm (~ 35 mg/L SDBS) and is very similar to K_i (2.93×10^{-3} cm) values reported by El Ouni (2013) and 2.9×10^{-3} cm by Costanza-Robinson et al. (2012). For this concentration (~ 35

mg/L) of surfactant, Kim et al. (1997) reported a higher K_i value of 5.06×10^{-3} cm, consistent with their measured γ -Ln(C) relationship (Figure 5).

3.2 Sorption Coefficient, K_d

Table 3 show the measured sorption coefficient (K_d) for Vinton soil from saturated tracer tests, IPTT (SDBS 8 and 9). These two experiments average $0.51 \text{ cm}^3/\text{g}$. These values are comparable to other independently measured values also shown in Table 3. The overall average, excluding outliers is $0.5 \text{ cm}^3/\text{g}$. Brusseau et al (2007) reported the 0.56 ml/g value.

For 45/50 media, the sorption coefficient K_d used is $0.05 \text{ cm}^3/\text{g}$ obtained from Brusseau et al. (2008) and El Ouni (2013) for comparable SDBS concentrations (35 mg/L). The sorption coefficient is an essential parameter in determining the amount of tracer that will be available to reside at the air-water interface, for the calculation of retardation factor (R), and consequently for the calculation of air-water total interfacial area. For consistency, the average value ($K_d=0.5 \text{ cm}^3/\text{g}$) for Vinton soil was used for all calculations in this work.

3.3 Aqueous-Phase Residual Interfacial Tracer Test (IPTT)

The breakthrough curves for the first set of experiments (SDBS 1-3) are shown in Figure 7 together with the breakthrough of the non-reactive tracer (PFBA). The non-reactive tracer was used as a baseline ($R=0.99$). The retardation factor (R) and the A_{aw} for all experiments are shown in Table (4). The R of SDBS ranges from 3.17 to 4.20. The

retardation factor of the interfacial tracer increases with decreasing water saturation (0.95-0.77).

For air-water interfacial calculations (A_{aw}), the water content of the porous media was monitored by measuring the weight of the column when saturated, after drainage, during the conditioning prior to surfactant injection, and after the full breakthrough curve. At this stage, all of the surfactant is presumed to have left the column. The column was dismantled and the porous media sectioned, weighed, and oven dried to obtain the final water content at the end of the experiment.

The procedure for entrapment or residual air was revised to measure the water content in the presence of surfactant. For this case, only the arrival-wave curves were recorded prior to water content measurements. In experiments SDBS 4-7 (Figure 8) the columns were originally dry-packed and background electrolyte solution was injected at a higher flow rate to trap air inside the column. The water content measured after the experiment was used for the calculations of interfacial area and water saturation. Table 4 shows the values calculated for R to average 3.37 for S_w of approximately 0.86.

In the first set of experiments (SDBS 1-3), the creation of residual air-content in the column was under secondary imbibition. In the second set of experiments (SDBS 4-7), the air content was trapped under primary imbibition conditions. Differences in experimental conditions may have contributed to differences in the measured interfacial areas, due to differences in the initial fluid-fluid configuration in the system. For a comparable system (i.e. darcy's flux, surfactant concentration, and porous media) Brusseau (2007) and El Ouni (2013) measured A_{aw} under both drainage and imbibition

conditions. However, significant differences in A_{aw} were not observed, suggesting that the aqueous-phase experiments may not be affected by small alterations in fluid-fluid configuration. This is somewhat expected, since IPTT-based measurements are considered to represent the effective air-water interfacial areas in the system (e.g. Anwar et al., 2000).

Figure 9 shows the relationship between air-water interfacial area as a function of water saturation for Vinton soil compared to the Standard IPTT by Brusseau et al. 2007; and El Ouni 2013. The gas-phase interfacial tracer regression curve shown in Figure 9 is based on GPTT tests by Peng and Brusseau (2005a, 2005b) and are shown in this section for reference only. For comparison to the data measured here, the imbibition and drainage data presented in Brusseau et al. (2007) was recalculated with a new interfacial partitioning coefficient ($K_i=2.99E-03$ cm). The new K_i is obtained from the compiled regression (Figure 6) of interfacial tension values as discussed in previous section. These values are reported in Table 4. Overall, evaluation of results in Figure 9 suggests that the A_{aw} measured from residual-IPTT experiments are in range of values reported by Brusseau et al. 2007, and El Ouni 2013 using the standard-IPPT method.

3.4 Mass Balance (MB) Interfacial Tracer Test

Figure 9 shows results for mass balance experiments using Vinton soil. Here significant scatter in measured interfacial area values are observed. These experiments were conducted with the expectation that it would yield interfacial areas at various saturations, ideally covering a much larger saturation range per experiment than

illustrated. Additional mass balance experiments were conducted in Accusand (Figure 10). Results for 45-50 sand also show a smaller range in wetting-phase saturation than expected. The homogeneity in pore size can cause the column to drain rapidly, resulting in a very dry top portion of the column, with a highly saturated bottom. This could potentially explain the saturation gap between middle saturation range 0.4-0.8 in MB1 (Accusand, Figure 11). Conversely, the heterogeneity of Vinton soil should lessen the issue of non-uniform drainage and improve water content gradient in the porous medium. However, results suggest that the mass balance approach yields scattered interfacial area values, and saturation ranges that are complimentary to IPTT measurements. Overall, each individual experiment covers a small range of water saturation.

For Vinton soil, it is possible that the scatter in the data is due to the fine particles that can interfere with UV-analysis. Thus, as a precaution, subsequent experiments (9-11) involved vortexing and extended settling time of samples prior to analysis by the UV-Spectrophotometer. The issue of fine particles was also observed to be problematic during surfactant equilibrium time. The presence of these small particles, which can move during recirculation, may have contributed to diminish conductivity of the capillary membrane. Thus, requiring higher pressures to drain the column, greater than pressures achieved using a hanging water column method. It is also possible that mobile fine particles may have affected overall tracer equilibrium due to sorption. The surfactant mass may have been sorbed onto these particles, which could have travelled and settled elsewhere. Thus, the total surfactant mass per ring may not have included this mobile mass, or the aqueous bulk SDBS mass may have been over estimated.

An independently measurement of sorption coefficient (K_d) was used as a reference of quality, due to significant scatter of the mass balance data. Experiments are considered for analysis when the K_d calculated from the saturated ring was reasonably similar to the independent values. For comparison to IPTT results, the data was calculated using $K_d=0.5 \text{ cm}^3/\text{g}$. Figure 9 compares MB results to IPTT data. The Gas-Phase IPTT and corresponding regression are again used here for reference only (Peng and Brusseau 2005). Additional measurements from Brusseau et al. (2007), El Ouni (2013) is included in Figure 9. Comparison to IPTT results suggests that MB results are highly variable although they are still in the expected range, and comparable to IPTT results. However, the saturation range is not predictable for each experiment (0.4-0.8).

3.5. Implications

The primary objective of this study was to investigate the different tracer-based methods for measurement of air-water interfacial area (A_{aw}) in unsaturated porous media. The dependence of A_{aw} on S_w complicates the comparison between approaches in terms of absolute values. Thus, all results are plotted together in Figure 9 with a regression derived from the gas-IPTT results. This regression line represents the expected range for comparison between the different methods. Note that only two points representing the higher S_w of the GPTT curve are shown for comparison. The different aqueous-test data sets are similar to the gas-IPTT data at high S_w . However, it is clearly observed that values from the GPTT experiments are much higher than the aqueous-phase measurements presented herein for lower saturations. This is expected as the aqueous-

phase based experiments are limited by the areas of surfactant solution accessible to the interface (e.g. Anwar et al., 2000; Schaefer et al., 2000; Brusseau et al., 2006; Brusseau et al., 2007; Araujo et al., 2010). Conversely, gas-phase tracer test results are the closest measurement to the true solid surface area, which includes surface roughness (e.g. Costanza-Robinson and Brusseau, 2002b; Peng and Brusseau, 2005a, 2005b; Brusseau et al., 2006; Brusseau et al., 2007; Sung and Chen, 2011).

Costanza-Robinson and Brusseau (2002b) suggested that that aqueous interfacial tracers and gas-phase tracers measure the A_{aw} corresponding to different domains of the porous media. Primarily, aqueous phase tracers have limited access to film associated interfaces, whereas gas-phase tracers have almost unlimited access to such interfaces. The latter includes domains associated with bulk fluid contributing to advective flow and residual water (e.g. Costanza-Robinson and Brusseau, 2002b). These regions may to some extent be accessed through diffusive processes.

The modified residual-IPTT approach is experimentally simple, using saturated flow conditions. This allows for faster experiments and direct analysis during the experiment. The saturated flow conditions limits the practical water saturation (S_w) range to approximately 0.70-1.0. The standard IPTT test conducted under unsaturated flow conditions is more challenging and requires longer test times due to the imposed boundary conditions. Using this approach, the water content can be reduced further, to an operational range between 1 and approximately 0.50 S_w . The limitation of both aqueous-phase miscible-displacement methods is that only one interfacial area value can be obtained per experiment.

The mass balance method (MB) was designed to circumvent these limitations by enabling A_{aw} interfacial values to be measured for multiple water saturations with a single experiment. This methodology allows for sufficient equilibrium time for the tracer to access the different domains in the system, e.g. air-water, water-solid. Although time consuming, all parameters are measured directly based on mass of surfactant. Thus the water content measured reflects the presence of surfactant, and the aqueous surfactant concentration is the equilibrium concentration. Sorption is measured directly from 'saturated' ring, which can be compared to independently measured values such as those obtained from IPTT test (e.g. SDBS 8, 9). The disadvantage is that one may still need several experiments to obtain A_{aw} values for a full drainage curve, from saturation to drier conditions due to the variability in S_w range. It is worthy of mention that the procedure is significantly more strenuous (2-3 weeks) when applied to highly heterogeneous soils, such as Vinton, than in simple media (e.g. 45-50). In comparison, approximately 5-10 days is required to complete an experiment using the residual IPTT approach. The duration of the experiments is primarily dictated by equilibrium, and drainage procedures, and is highly influenced by user expertise.

Overall, results presented in this study are within the expected values based on simulated gas-phase tracer test results. Significant differences in interfacial measurements were not observed for the different methods of aqueous-phase tracer tests. This indicates that the various methods can provide reasonably similar measures of air-water interfacial area within the restrictions of each method.

Much research has been conducted to measure the air-water interface, and still there has not been a consensus of evidence for which of several approaches used to infer air-water interfacial area (A_{aw}) will yield consistent information. The aqueous tracers are restricted to areas contributing to bulk fluid flow, and thus only a fraction of the total interface can be measured. Varying experimental techniques can further restrict areas available for characterization. For example, microtomography methods (Appendix A, B) cannot resolve water films, or areas associated with surface roughness. Similarly, aqueous-based tracer method results suggest that interfacial areas have access to interfaces near the path of fluid flow (i.e. residual air) that are accessed via diffusion. These experiments are also sensitive to tracer concentration and sorption. Sorption is especially important in measurements using natural soils and sediments.

4. REFERENCES

- Adamson, A. W. (1982), *Physical chemistry of surfaces*, 4th ed., xviii, 664 p. pp., J. Wiley, New York.
- Anwar, A., M. Bettahar, and U. Matsubayashi (2000), A method for determining air-water interfacial area in variably saturated porous media, *Journal of Contaminant Hydrology*, 43(2), 129-146.
- Araújo, J. B., Narter, M., Mainhagu, J., Marble, J., and Brusseau, M.L. (2010), Comparison of methods for measuring air-water interfacial area in porous media, H53D-1066 presented at 2010 Fall Meeting, AGU, San Francisco, Calif., 13-17 Dec.
- Bear, J. (1988, c1972), *Dynamics Of Fluids In Porous Media*, American Elsevier Publishing Company, Inc., Dover, NY.
- Brusseau, M. L. (1999), Innovative subsurface remediation field testing of physical, chemical, and characterization technologies, in *ACS symposium series 725*, edited, pp. 1 online resource (xii, 299 p.), American Chemical Society, Washington, DC.
- Brusseau, M. L., and R. Srivastava (1997), Nonideal transport of reactive solutes in heterogeneous porous media - 2. Quantitative analysis of the Borden natural-gradient field experiment, *Journal of Contaminant Hydrology*, 28(1-2), 115-155.
- Brusseau, M. L., J. Popovicova, and J. A. K. Silva (1997), Characterizing gas-water interfacial and bulk water partitioning for gas phase transport of organic contaminants in unsaturated porous media, *Environmental Science & Technology*, 31(6), 1645-1649.
- Brusseau, M. L., M. Narter, and H. Janousek (2010), Interfacial Partitioning Tracer Test Measurements of Organic-Liquid/Water Interfacial Areas: Application to Soils and the Influence of Surface Roughness, *Environmental Science & Technology*, 44(19), 7596-7600.
- Brusseau, M. L., S. Peng, G. Schnaar, and M. S. Costanza-Robinson (2006), Relationships among air-water interfacial area, capillary pressure, and water saturation for a sandy porous medium, *Water Resources Research*, 42(3).
- Brusseau, M. L., S. Peng, G. Schnaar, and A. Murao (2007), Measuring air-water interfacial areas with X-ray microtomography and interfacial partitioning tracer tests, *Environmental Science & Technology*, 41(6), 1956-1961.
- Brusseau, M. L., H. Janousek, A. Murao, and G. Schnaar (2008), Synchrotron X-ray microtomography and interfacial partitioning tracer test measurements of NAPL-water interfacial areas, *Water Resources Research*, 44(1).

- Celia, M. A., W. G. Gray, C. D. Montemagno, and P. C. Reeves (1998), On the inclusion of interfacial area in models of two-phase flow in porous media, in *Iahs-Aish P*, edited by M. Herbert and K. Kovar, pp. 81-87.
- Costanza-Robinson, M. S., and M. L. Brusseau (2002a), Gas phase advection and dispersion in unsaturated porous media, *Water Resources Research*, 38(4).
- Costanza-Robinson, M. S., and M. L. Brusseau (2002b), Air-water interfacial areas in unsaturated soils: Evaluation of interfacial domains, *Water Resources Research*, 38(10).
- Costanza-Robinson, M. S., and M. L. Brusseau (2006), Gas-Phase Dispersion in Porous Media, *Theor Appl Trans Por*, 20, 121-132.
- El Ouni, A. (2013), Measuring Air-Water Interfacial Area in Unsaturated Porous Media Using the Interfacial Partitioning Tracer Test Method, edited, p. 62 leaves, University of Arizona, University of Arizona.
- Freeze, R. A., and J. A. Cherry (1979), *Groundwater*, Prentice-Hall, Inc., Eaglewood Cliffs, NJ.
- Gvirtzman, H., and P. V. Roberts (1991), Pore Scale Spatial-Analysis of 2 Immiscible Fluids in Porous-Media, *Water Resources Research*, 27(6), 1165-1176.
- Hassanizadeh, S. M., and W. G. Gray (1993), Toward An Improved Description Of The Physics Of 2-Phase Flow, *Advances in Water Resources*, 16(1), 53-67.
- Karkare, M. V., and T. Fort (1994), Flow In Unsaturated Porous-Media Due To Water-Insoluble Surfactants - Role Of Momentum-Transfer From A Spreading Monolayer, *Langmuir*, 10(10), 3701-3704.
- Karkare, M. V., and T. Fort (1996), Determination of the air-water interfacial area in wet "unsaturated" porous media, *Langmuir*, 12(8), 2041-2044.
- Karkare, M. V., H. T. La, and T. Fort (1993), Criteria For Effectiveness Of Surfactants As Water-Moving Agents In Unsaturated Wet Sand, *Langmuir*, 9(7), 1684-1690.
- Kawanishi, T., Y. Hayashi, P. V. Roberts, and M. J. Blunt (1998), Fluid-fluid interfacial area during two and three phase fluid displacement in porous media: a network model study, *Iahs-Aish P*(250), 89-96.
- Kibbey, T. C. G. (2013), The configuration of water on rough natural surfaces: Implications for understanding air-water interfacial area, film thickness, and imaging resolution, *Water Resources Research*, 49(8), 4765-4774.

- Kibbey, T. C. G., and L. X. Chen (2012), A pore network model study of the fluid-fluid interfacial areas measured by dynamic-interface tracer depletion and miscible displacement water phase advective tracer methods, *Water Resources Research*, 48.
- Kim, H., P. S. C. Rao, and M. D. Annable (1997), Determination of effective air-water interfacial area in partially saturated porous media using surfactant adsorption, *Water Resources Research*, 33(12), 2705-2711.
- Kim, H., P. S. C. Rao, and M. D. Annable (1999), Gaseous tracer technique for estimating air-water interfacial areas and interface mobility, *Soil Science Society of America Journal*, 63(6), 1554-1560.
- Kim, H., K. M. Choi, J. W. Moon, and M. D. Annable (2006), Changes in air saturation and air-water interfacial area during surfactant-enhanced air sparging in saturated sand, *Journal of Contaminant Hydrology*, 88(1-2), 23-35.
- Narter, M., and M. L. Brusseau (2010), Comparison of interfacial partitioning tracer test and high-resolution microtomography measurements of fluid-fluid interfacial areas for an ideal porous medium, *Water Resources Research*, 46.
- Peng, S., and M. L. Brusseau (2005a), Impact of soil texture on air-water interfacial areas in unsaturated sandy porous media, *Water Resources Research*, 41(3).
- Peng, S., and M. L. Brusseau (2005b), Gas-phase partitioning tracer test method for water content measurement: Evaluating efficacy for a range of porous-medium textures, *Vadose Zone Journal*, 4(3), 881-884.
- Reeves, P. C., and M. A. Celia (1996), A functional relationship between capillary pressure, saturation, and interfacial area as revealed by a pore-scale network model, *Water Resources Research*, 32(8), 2345-2358.
- Saripalli, K. P., H. Kim, P. S. C. Rao, and M. D. Annable (1997), Measurement of specific fluid - Fluid interfacial areas of immiscible fluids in porous media, *Environmental Science & Technology*, 31(3), 932-936.
- Schaefer, C. E., D. A. DiCarlo, and M. J. Blunt (2000), Determination of Water-Oil Interfacial Area during 3-Phase Gravity Drainage in Porous Media, *J Colloid Interface Sci*, 221(2), 308-312.
- Silverstein, D. L., and T. Fort (1997), Studies in air-water interfacial area for wet unsaturated particulate porous media systems, *Langmuir*, 13(17), 4758-4761.
- Skop, J. (1985), Oxygen Uptake and Transport in Soils: Analysis of the Air-water Interfacial Area, *Soil Science Society of America Journal*, 49(6), 1327-1331.

Sung, M., and B. H. Chen (2011), Using aliphatic alcohols as gaseous tracers in determination of water contents and air-water interfacial areas in unsaturated sands, *J Contam Hydrol*, 126(3-4), 226-234.

Tanford, C. (1974), Theory of Micelle Formation in Aqueous-Solutions, *J Phys Chem-Us*, 78(24), 2469-2479.

TABLES:**Table 1:** Measured surface tension values for SDBS solution in 0.01 M NaCl.

SDBS (mg/L)	Average γ (dyn/cm)	P/(D-d) (--)	F (--)	Corrected value, S (dyn/cm)
150	35.7	35.8	0.89	31.9
135	35.7	35.8	0.89	31.9
120	36.5	36.6	0.89	32.7
105	37.8	37.9	0.90	33.9
90	39.2	39.3	0.90	35.2
75	41.8	41.9	0.90	37.7
60	43.5	43.6	0.90	39.3
45	46.1	46.2	0.91	41.8
30	49.0	49.1	0.91	44.6
15	54.5	54.6	0.92	49.9
NaCl	74.4	74.6	0.94	69.6
H2O	74.5	74.7	0.94	69.7

¹Circumference of Ring (R)=5.983cm; $R_{\text{ring}}/R_{\text{wire}}$ (R/r)=53.59;

²Densities at approximately 20 °C of Air=0.0012041 g/cm³; H₂O=0.999 g/cm³; SDBS=0.18 g/cm³.

Table 2: Porous Medium Characteristics

	Particle Density	median grain diameter d_{50}	porosity	bulk density	U (d_{60}/d_{10})
	(g/cm^3)	(mm)	(--)	(g/cm^3)	(--)
Vinton	2.59	0.28	0.42	1.5	2.4
45/50	2.64	0.35	0.34	1.8	1.1

U_a = uniformity coefficient, d_i is the percentage of grains smaller than a given sieve size

Table 3: Sorption coefficient measurement using Vinton soil and SDBS solution prepared with NaCl as the electrolyte solution.

	R	θ_w	ρ_b	Q	C_0 SDBS	K_d
	(--)	(vol./vol.)	(g/cm ³)	(ml/min)	(mg/l)	(cm ³ /g)
1 (SDBS 8)	2.69	0.43	1.48	0.63	37.8	0.492
2 (SDBS 9)	2.53	0.42	1.48	0.60	40.6	0.523
3	3.67	0.37	1.53	0.2	40.6	0.642
4	2.92	0.38	1.49	0.5	37.5	0.493
5	3.89	0.39	1.56	1.0	36.7	0.723 ^a
6	2.92	0.39	1.56	1.0	34.9	0.482 ^b
7	2.84	0.39	1.56	1.0	34.7	0.461 ^c
8	2.98	0.43	1.53	0.61	35	0.555

The average value for all K_d is 0.501 cm³/g excluding outliers, for 36.8 mg/L SDBS solution.

Measurements 5-7: SDBS solution prepared using Br as the electrolyte, ^a100 mg/l Br- or 128.8 mg/l NaBr; ^b10 mg/l Br- or 12.88 mg/l NaBr; ^c1 mg/l Br- or 1.288 mg/l NaBr.

*Information for measurements 3 and 4 obtained from El Ouni (2013), 5-7 measured by Dr. Hua Zhong, and measurement 8 is measured by Dr. Ann Russo-Lee.

Table 4: Results for residual saturation interfacial partitioning tracer tests (IPTT):

		Condition*	C (mg/L)	θ_w (vol./vol.)	$^a t_R$ (min)	ρ_b (g/cm ³)	S_w (--)	R (--)	K_i (cm)	A_{aw} (cm ⁻¹)	A_{max} (cm ⁻¹)
Full BTC curves	SDBS 1	imbibition	33.8	0.34	39	1.59	0.89	3.48	3.1E-03	16	139
	SDBS 2	imbibition	34.8	0.39	44	1.53	0.95	3.17	3.0E-03	23	442
	SDBS 3	imbibition	36.6	0.30	35	1.58	0.77	4.20	2.8E-03	55	234
Arrival wave only	SDBS 4	imbibition	38.8	0.37	43	1.43	0.83	3.76	2.7E-03	112	648
	SDBS 5	imbibition	38.8	0.38	45	1.47	0.89	3.25	2.7E-03	45	397
	SDBS 6	imbibition	37.1	0.38	45	1.49	0.90	3.06	2.8E-03	14	135
	SDBS 7	imbibition	37.2	0.34	40	1.52	0.83	3.41	2.8E-03	20	119
K _d	SDBS 8	--	37.8	0.43	51	1.48	1.01	2.69	2.8E-03	--	--
	SDBS 9	--	40.6	0.42	51	1.48	0.99	2.85	2.9E-03	--	--

^aHydraulic residence time, L_{column}/v , where $v=Q/(A*\theta)$

*For experiments 1-3, the column was under 2nd imbibition, whereas in experiments 4-7 they were conducted in primary imbibition conditions. K_d for experiments 1-7 0.5 g/cm³.

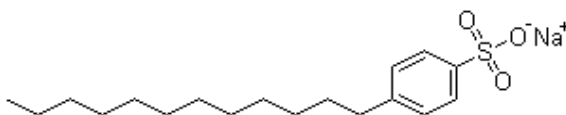
FIGURES:

Figure 1: Chemical structure of sodium linear-dodecylbenzenesulfonate (SDBS) structure.

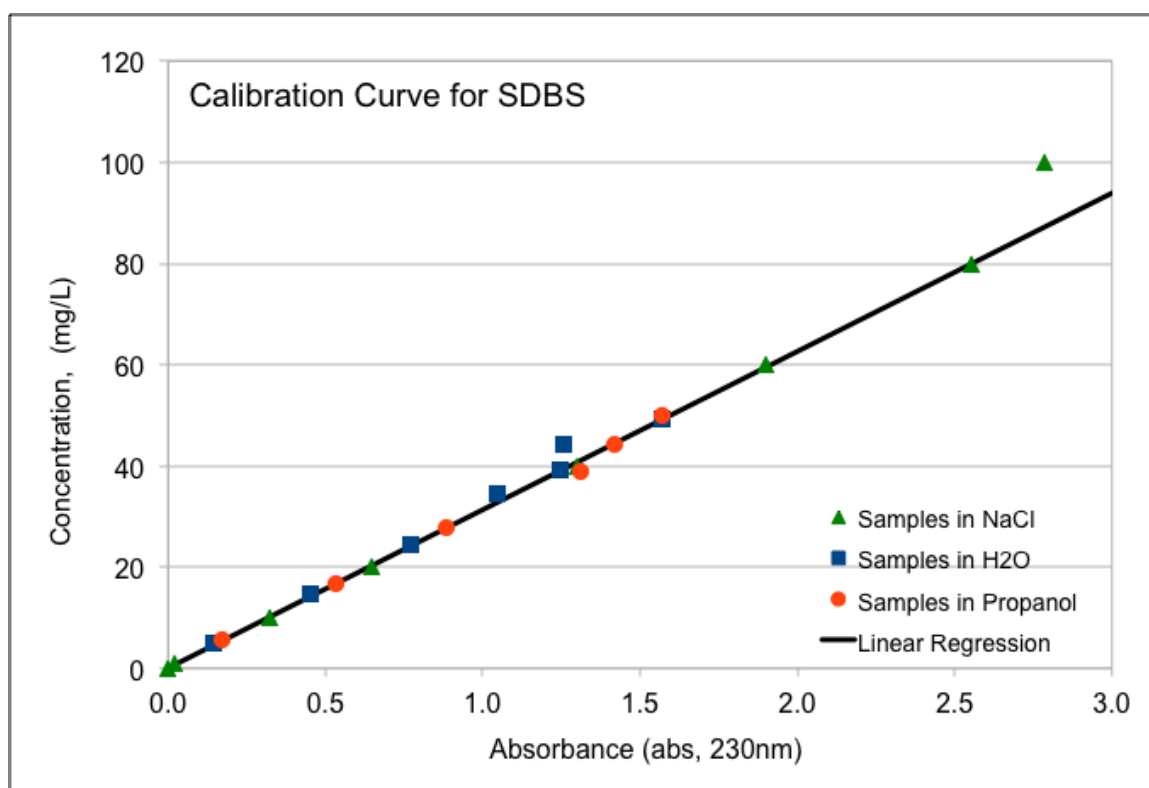


Figure 2: Measured concentration as a function of absorbance. SDBS solution prepared in 0.01M NaCl, water, 2-D propanol. Regression equation used based on NaCl data, $C_i = 31.283 \text{abs} + 0.0469$. Outlier indicates SDBS concentration above linear range.

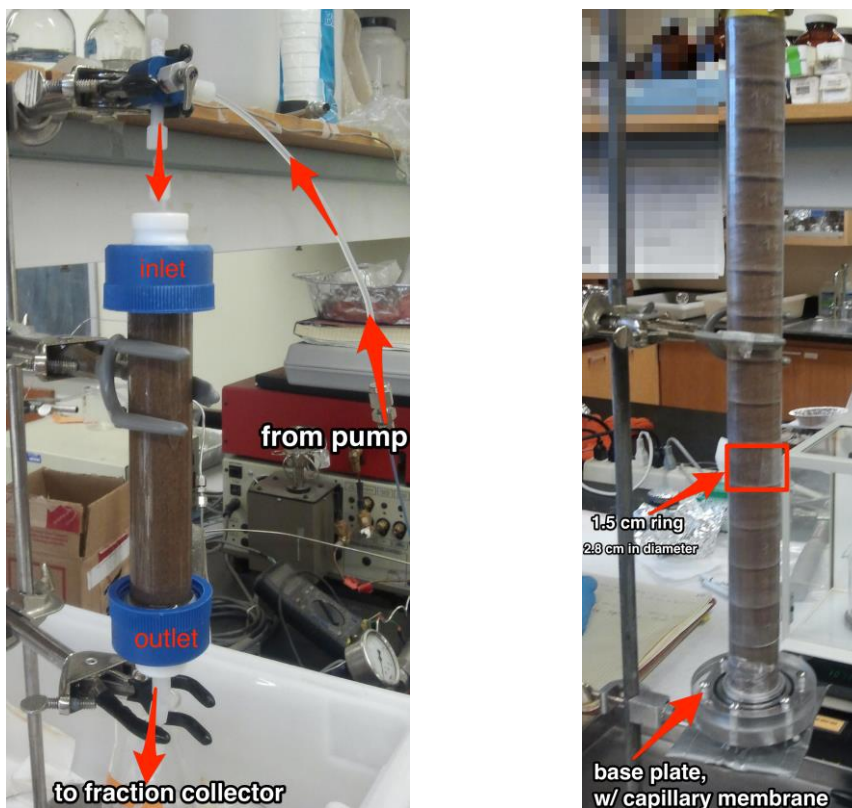


Figure 3: *Left.* Aqueous-phase tracer test set-up example, using 15 cm glass column. Above is a saturated Vinton soil column pack. *Right.* Example of Mass Balance ring column ($d_{in}=2.8$ cm) with Vinton soil. Each ring is 1.5 cm with the exception of the bottom ring right above the base plate (5cm).

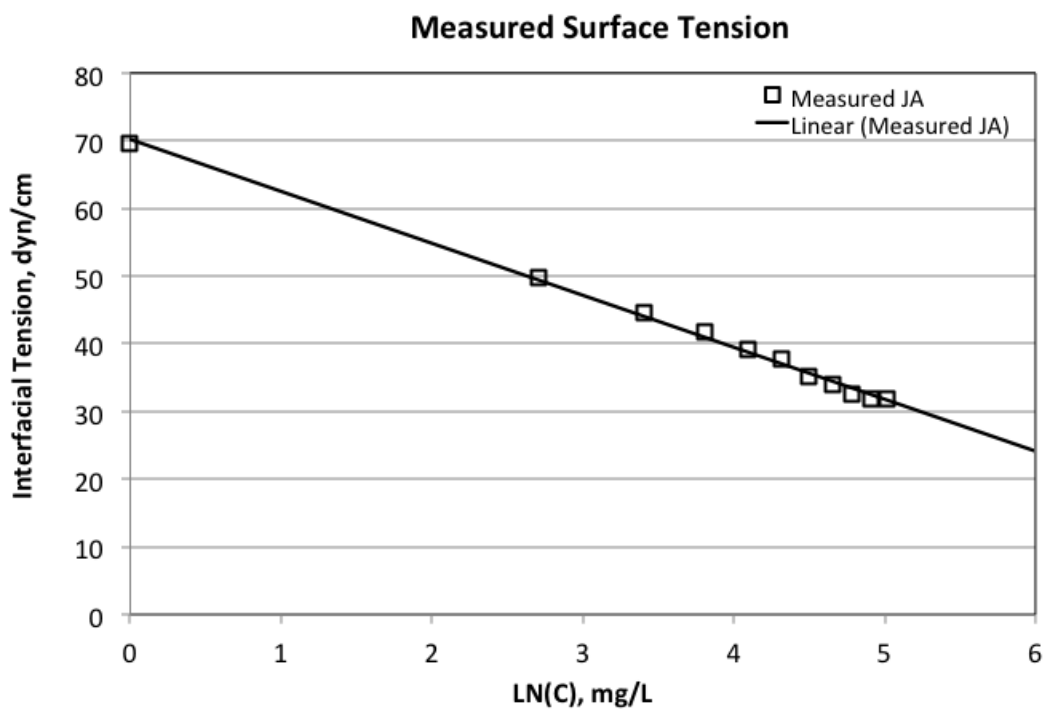


Figure 4: Measured interfacial tension for SDBS in 0.01 M NaCl using the ring method. $\gamma=7.68*\text{LN}(C)+69.576+70.193$, $R^2=0.997$; C is concentration (mg/L), and γ is interfacial tension (dyn/cm).

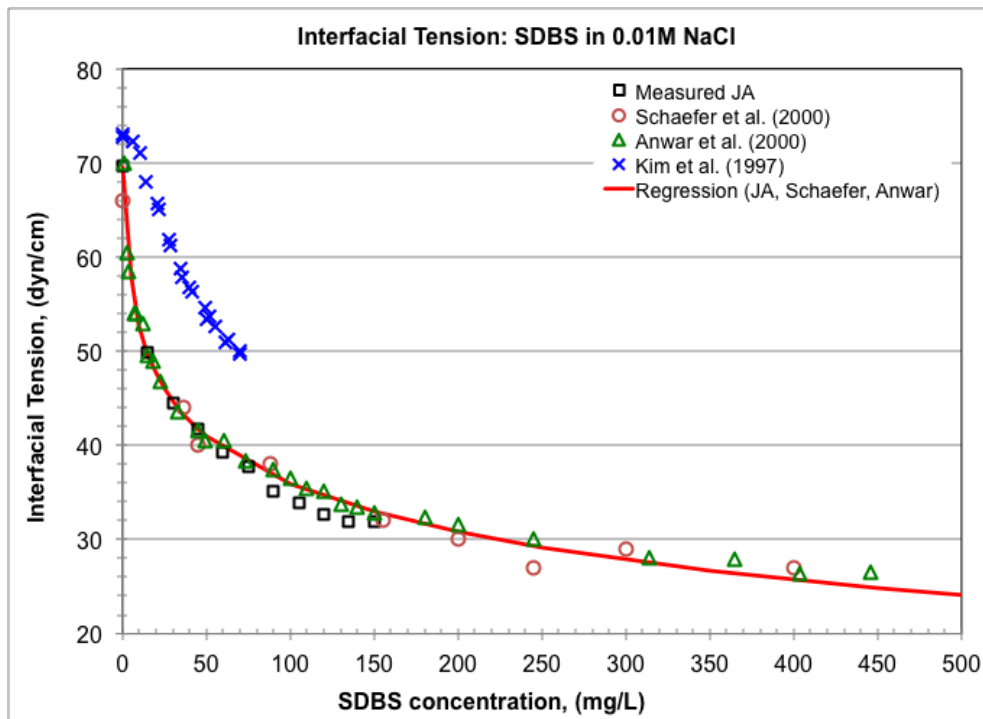


Figure 5: Comparison between measured interfacial tension values and reported values.

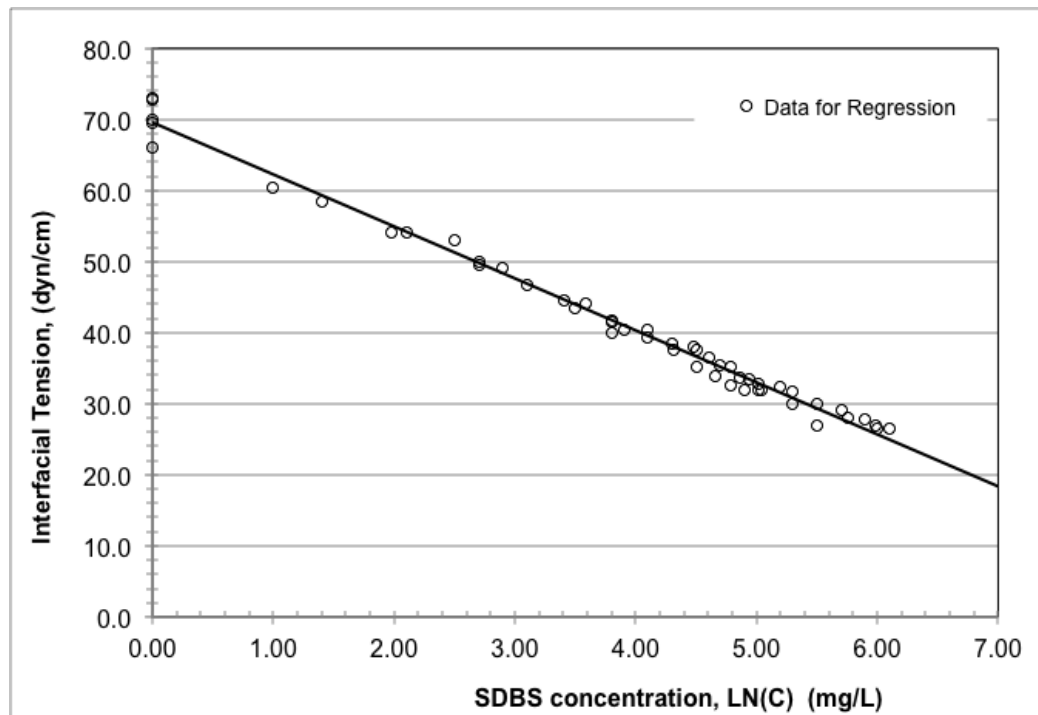


Figure 6: Linear Interfacial tension relationship calculated from measured data. Data includes measured data presented in this study, Schaefer et al. (2000), and Anwar et al. (2000) data. $\gamma=7.3151*\text{LN}(C)+69.576$, $R^2=0.99$; C is concentration (mg/L), and γ is interfacial tension (dyn/cm).

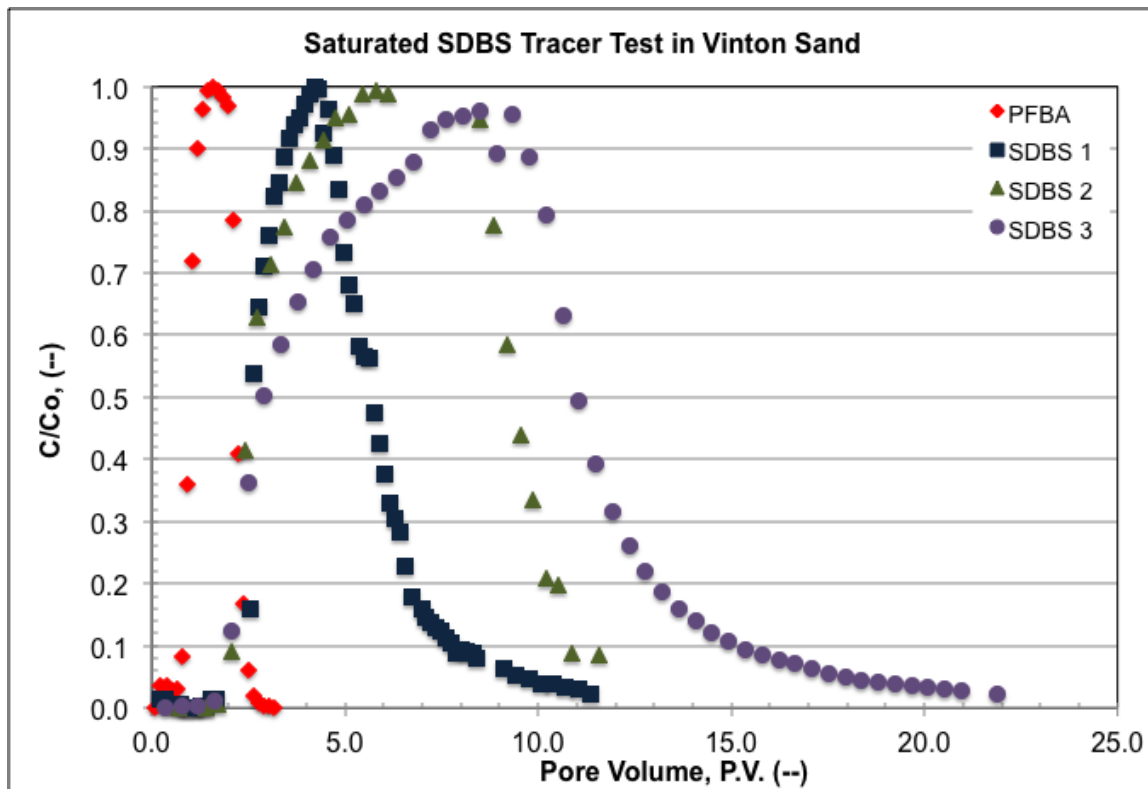


Figure 7: Breakthrough curves for residual-air SDBS experiments 1-3, and conservative tracer test.

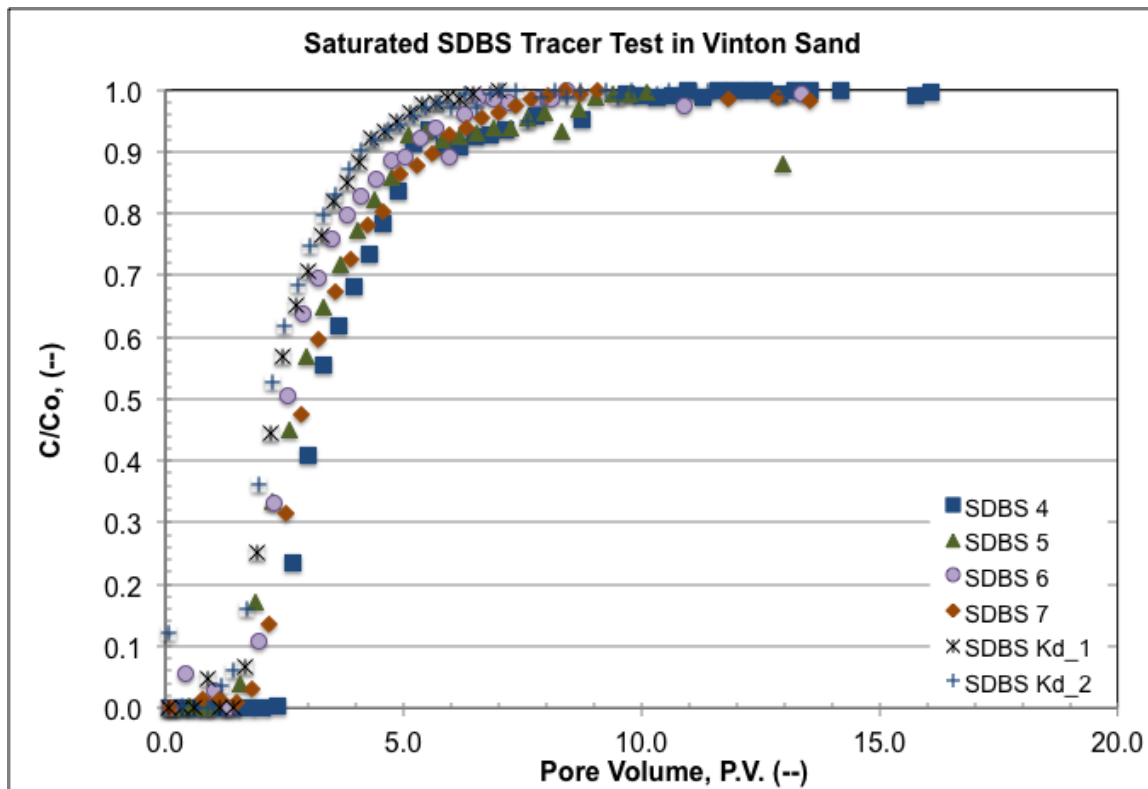


Figure 8: Arrival wave for trapped air SDBS experiments 4-7, and saturated experiments (8-9) from which K_d values were measured.

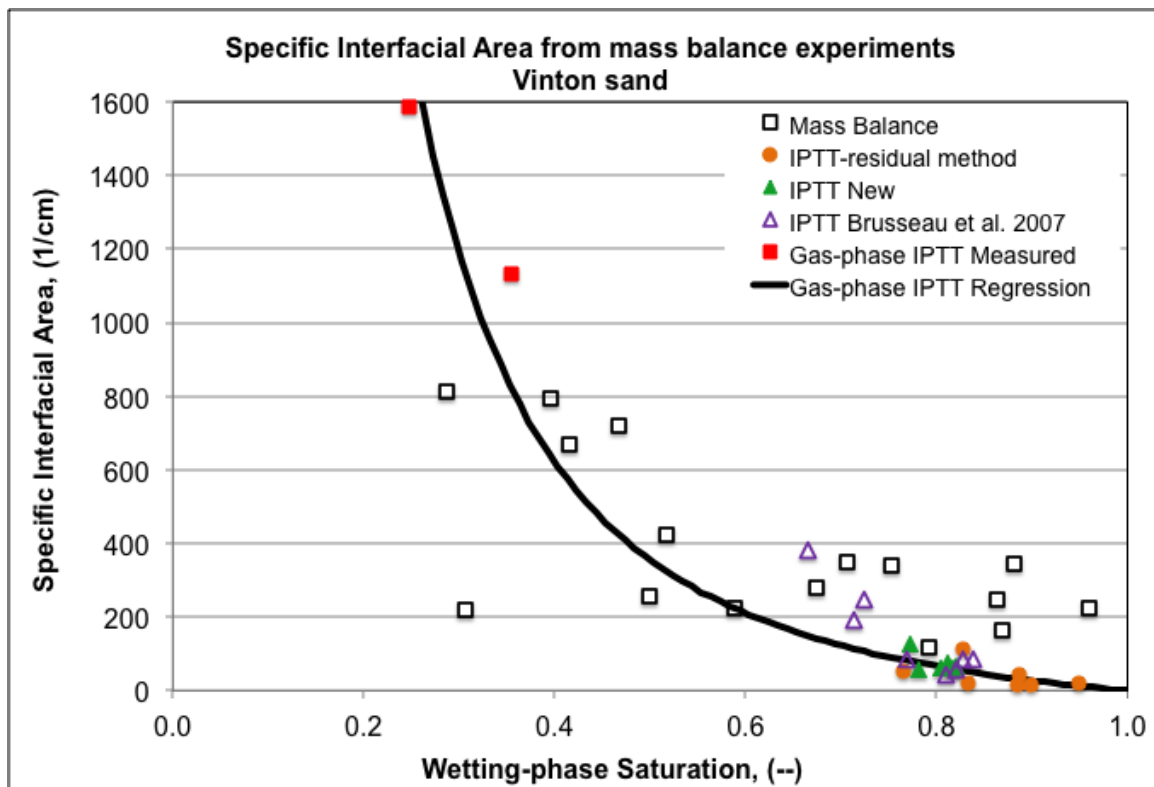


Figure 9: Comparison of compiled Mass Balance (MB) results, Residual interfacial tracer tests (IPTT) and Gas Phase Tracer Tests (Peng and Brusseau 2005). IPTT New (El Ouni 2013) and IPTT (Brusseau et al. 2007) represent aqueous-phase IPTT using the standard method.

5. ADDITIONAL INFORMATION

Table 5: SDBS aqueous-phase IPTT results for unsaturated Vinton soil. Data from Brusseau et al. 2007, recalculated using K_i measured (in this work).

Condition	R	S_w	θ_w	ρ_b (g/cm ³)	Porosity	^a A_{aw} (cm ⁻¹)	^c A_{max} (cm ⁻¹)
imbibition	6.9	0.72	0.28	1.64	0.39	247	895
imbibition	4.9	0.77	0.30	1.64	0.39	85	366
imbibition	4.2	0.8	0.32	1.61	0.40	45	238
imbibition	4.3	0.82	0.33	1.61	0.40	58	324
drainage	8.9	0.67	0.26	1.64	0.39	383	1147
drainage	6.4	0.71	0.28	1.64	0.39	193	673
drainage	4.6	0.83	0.32	1.64	0.39	87	506
drainage	4.6	0.84	0.33	1.65	0.39	83	514

^aRecalculation of interfacial area based on parameters published by Brusseau et al. 2007. Experiments conducted using a vacuum chamber to control the saturation under steady-state conditions (Standard IPTT).

^b $K_d=0.56$ cm³/g. Air-water interfacial area (A_{aw}) calculated with $K_i=2.99-03$ cm.

^cmaximum interfacial area (A_{max})= $A_{aw}/(1-S_w)$.

Table 6: SDBS aqueous-phase IPTT results for unsaturated Mixed Sand. Data from Kim et al. 1997, recalculated using K_i measured (in this work).

Condition	R	S_w	θ_w	^a Aaw (cm ⁻¹)	^{*b} Recalculated	
					Aaw (cm ⁻¹)	^c A _{max} (cm ⁻¹)
drainage	1.07	1	0.36	--	--	--
drainage	1.28	0.9	0.33	12.5	23	225
drainage	1.38	0.74	0.27	14.9	26	100
drainage	1.78	0.58	0.21	27	46	110
drainage	2.59	0.39	0.14	38.9	66	108
drainage	3.44	0.29	0.11	46.4	81	115

*Recalculation of interfacial area based on parameters published by Kim et al. (1997).

Air-water interfacial area (Aaw) calculated with ^a $K_i=5.06E-03$ cm, and ^b $K_i=2.99-03$ cm.

^{a,b} $K_d=0.015$ cm³/g calculated based on saturated experiment, $R=1$, porosity=0.36, bulk density=1.72 g/cm³.

^cMaximum interfacial area (A_{max})=Aaw/(1- S_w).

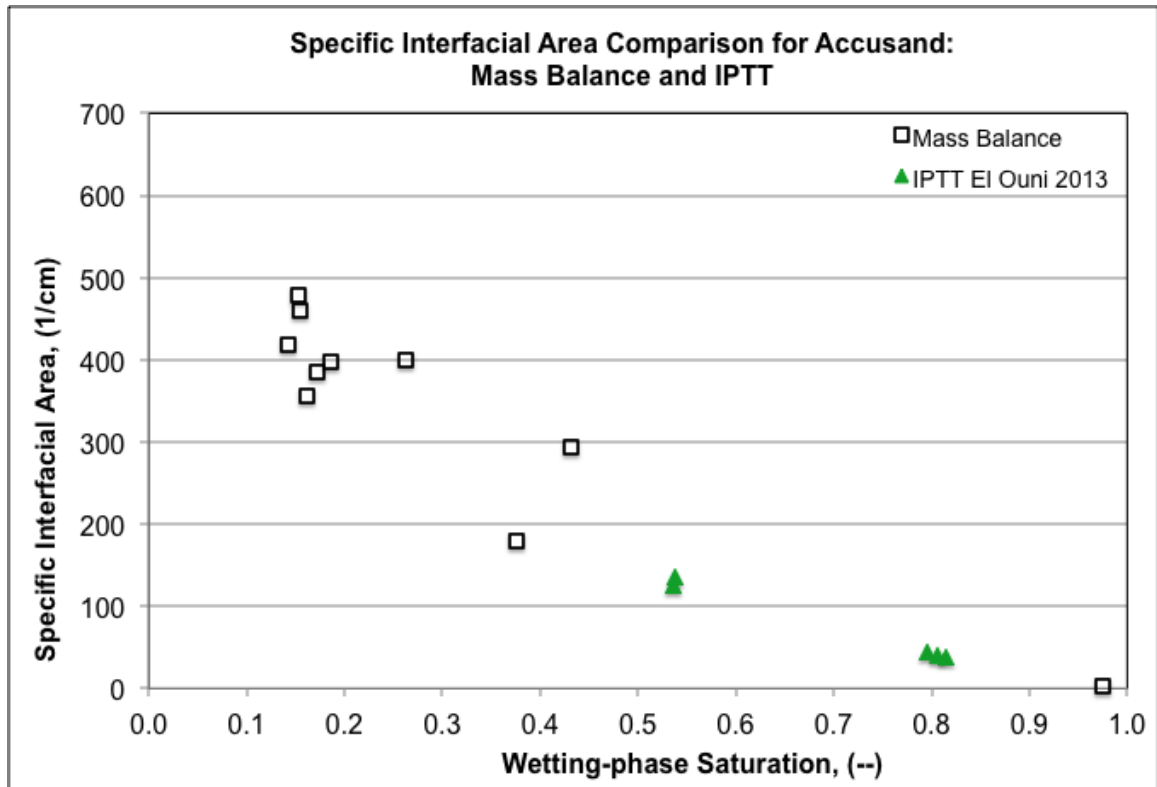


Figure 10: Mass Balance Experiments for Accusand (45-50) and standard IPTT (El Ouni 2013).

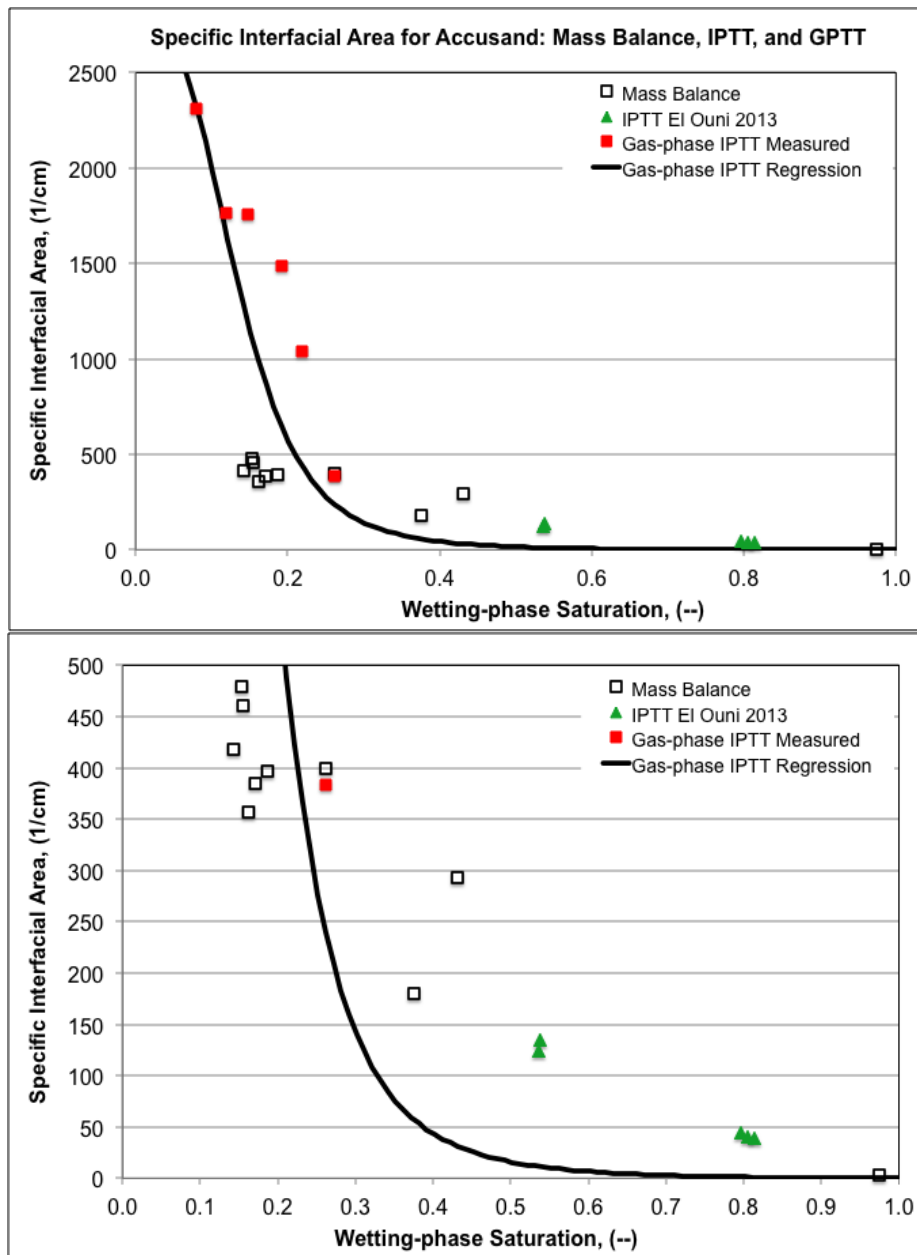


Figure 11: Comparison of interfacial area (A_{a-w}) as a function of water saturation (S_w) using aqueous phase Tracer Tests (IPTT) and Mass Balance Results (MB). Data for Gas-phase IPTT is obtained from Peng and Brusseau (2005). IPTT standard data is based on published data by Brusseau et al. 2007 and experiments performed by El Ouni 2013.

APPENDIX F POROUS MEDIA CHARACTERIZATION

1. Particle Density using Pycnometer Method

Soil was oven dried for at least 72 hours prior to measurements, in sufficient quantities to allow for multiple replicates (2-3 at a time). Deionized water was used. The pycnometer was weighed empty, then filled only with water. After establishing the volume of water, approximately 10 g of dry soil was added to the flask and its weight recorded. The dry sample was carefully saturated with H₂O to approximately 90% of the pycnometer's volume. The cap was inserted, carefully to ensure that fine materials would not escape through the capillary. Using a hypodermic syringe, the flask was filled with water until the top. Measured again to establish the volume displacement.

The temperature table on the Particle Density sheet allowed for precise water density correction based on water temperature. The temperature of water used was measured prior to each measurement set. Equation 1 was used for calculation of particle density (ρ_p), where ρ_w is density of water (g/cm³), W_s is the weight of the pycnometer with soil, W_a with air, W_w is weight of pycnometer filled with water only. The subscript s-w indicates the pycnometer is filled with soil and water (ASTM 2002).

$$\rho_p = \frac{\rho_w \cdot (W_s - W_a)}{(W_s - W_a) - (W_{sw} - W_w)} \quad (1)$$

Reference:

Methods of Soil Analysis. *Soil Science Society of America, IV.* p. 229-240. (2002)

Table 1: Results from Pycnometer particle density (ρ_p) measurements:

Soil	Empty	With oven dried soil	Water only	Water and sand	Temp.	Density of Water	Particle Density	Stand. Dev./ Var.
	(g)	(g)	(g)	(g)	(°C)	(g/cm ³)	(g/cm ³)	
Glass Beads	32.1272	42.1367	59.6880	65.1899	24.0	0.9973	2.215	
	31.0842	39.6846	62.1975	66.9141	24.0	0.9973	2.208	
	32.1302	41.5163	59.6694	64.8336	25.0	0.9970	2.217	
	31.0881	39.1927	62.1929	66.6165	25.0	0.9970	2.195	
	32.1277	41.3735	59.6859	64.7829	24.0	0.9973	2.223	0.01038
							2.213	0.00011
20/30	32.1286	42.2845	59.7527	66.0173	23.0	0.9975	2.603	
	32.1276	41.2997	59.7465	65.4556	23.0	0.9975	2.642	
	32.1275	43.0443	59.7028	66.8665	22.0	0.9978	2.902	
	32.1414	42.5761	59.6935	66.2041	22.7	0.9976	2.653	
	31.0849	38.4898	62.2037	66.8101	22.7	0.9976	2.640	0.12117
							2.688	0.01468
45/50	32.1308	42.2071	59.7218	65.9789	24.0	0.9973	2.631	
	32.1280	42.0221	59.6908	65.8522	24.0	0.9973	2.643	
	31.0888	38.6329	62.2121	66.9051	24.0	0.9973	2.639	0.00621
							2.638	0.00004
70/100	32.1381	42.6990	59.7285	66.2492	24.0	0.9973	2.607	
	31.0904	44.2836	62.1909	70.3906	24.0	0.9973	2.635	
	32.1282	40.3410	59.6714	64.9437	26.0	0.9968	2.784	
	31.0849	41.7619	62.1993	68.8069	26.0	0.9968	2.615	
	34.5841	42.8037	61.3704	66.4509	26.0	0.9968	2.610	0.07557
							2.650	0.00571
Borden	32.1343	42.0779	59.7787	66.1114	22.0	0.9978	2.748	
	32.1277	41.4547	59.7038	65.5652	24.0	0.9973	2.684	
	32.1324	41.3528	59.7059	65.6459	26.5	0.9966	2.801	
	32.1295	43.6173	59.6963	66.9735	26.8	0.9966	2.719	
	31.0842	36.3384	62.1823	65.5372	26.8	0.9966	2.757	
	31.0871	38.7702	62.2032	67.0049	26.5	0.9966	2.658	
	31.0866	38.6679	62.1998	66.9489	24.0	0.9973	2.670	0.05241
							2.719	0.00275

Soil	Empty	With oven dried soil	Water only	Water and sand	Temp.	Density of Water	Particle Density	Stand. Dev./ Var.
	(g)	(g)	(g)	(g)	(°C)	(g/cm ³)	(g/cm ³)	
Eustis	31.0842	40.7926	60.9360	68.4650	22.5	0.9977	4.444	
	32.1388	47.4564	62.1675	69.6521	26.0	0.9968	1.949	
	31.0859	47.8637	59.6677	72.5280	26.0	0.9968	4.269	
	34.5836	49.5641	61.7809	70.9627	26.0	0.9968	2.575	
	32.1269	45.3647	59.7039	67.9726	25.7	0.9969	2.656	
	31.0841	43.8095	62.2008	70.0988	25.7	0.9969	2.628	
	31.0883	41.8523	62.1996	68.8029	25.7	0.9969	2.579	
	32.1308	45.0203	59.6866	67.6972	25.7	0.9969	2.634	0.036
						2.614	0.001	
Vinton	32.1305	41.8755	59.6925	65.7517	23.0	0.9975	2.637	
	31.0884	40.5070	62.1897	67.9275	23.0	0.9975	2.553	
	31.0883	40.0563	62.1871	67.6859	25.0	0.9970	2.577	
	32.1313	40.5781	59.7057	64.9935	25.0	0.9970	2.666	
	34.5963	45.8476	61.4110	68.2360	23.0	0.9975	2.536	0.06
						2.594	0.003	
Hayhook	32.1313	42.6107	59.7156	66.1526	22.5	0.9977	2.586	
	31.0902	41.7535	62.8332	68.5948	22.5	0.9977	2.170	
	32.1396	41.8913	59.6674	65.6019	26.5	0.9966	2.546	
	31.0871	43.2882	62.1739	69.6119	26.5	0.9966	2.553	
	35.5850	47.7509	61.3868	69.3573	26.5	0.9966	2.890	0.26
						2.549	0.07	
Mount Lemmon	32.1355	41.0430	59.7007	65.2683	23.0	0.9975	2.660	
	34.5918	43.1860	61.4252	66.2804	23.0	0.9975	2.293	
	32.1332	39.9589	59.6802	64.3636	26.5	0.9966	2.482	
	31.0879	39.9484	62.1711	67.3622	26.5	0.9966	2.407	
	32.1317	39.0706	59.6873	63.9404	26.8	0.9966	2.575	
	31.0863	38.0726	62.1749	66.4075	26.8	0.9966	2.528	0.13
						2.491	0.02	

2. Soil-Water Characteristic Curves

The soil-water characteristic curve is an important soil property that relates the water content and the matric potential for a given soil. It describes the interconnectivity of pores, and pore size, as it affects both the structure and texture of soil. It is a critical parameter used for modeling of water flow, or in any other application requiring the knowledge of the porous system and its water content, such as drainage experiments. In this case, knowledge of air-entry pressure values gratefully aid experimental design. There are several measurement techniques to obtain an SWC curve (e.g. Freeze and Cheery 1979). The main requirement is that both the water content and the matric potential are known at a specific location.

In the laboratory, it is common to use pressure flow cells (e.g. Tempe Cell), pressure plates, or hanging water columns. The pressure flow cell holds the sample in encased metal rings, and pressure is applied to an initially completely saturated sample. Using the Tempe cell (pressure flow cells) it is possible to apply several pressure steps to the same sample as it drains, and the cells can also be disconnected so that the change in water content can be measured for each pressure step. The applicable matric potential range using this technique is 0 to -1000 cm of water. When necessary, a thermocouple psychrometer or dewpoint water potentiometer can be used in conjunction with the Tempe Cell measurements to obtain matric potentials at higher pressures, where lower water contents are present. The dewpoint water potential meter infers the relative humidity by measuring the dry and wet bulb temperatures. A thermocouple psychrometer uses is a double junction of two different metals, where each are subjected to different

temperatures so that they can generate a voltage difference, based on the electrical current applied, which creates a temperature difference, cooling one while heating the other junction.

The SWC curve for 45/50 sand (Figure 1) and Eustis sand (Figure 2), were measured at The Center for Environmental Physics and Mineralogy (The University of Arizona, Tucson, AZ) using a Tempe Cell and a Dewpoint Tensionmeter. The results were then fitted with the van Genuchten parametric model to obtain a continuous relationship between matric potential and water content. The van Genuchten parametric model (equation 2) was developed in 1980 based on the residual water content (θ_r), saturated water content (θ_s), and a few parameters that are dependent on the shape of the water content versus matric potential (ψ_m) curve (e.g. van Genuchten 1980):

$$\theta(\psi) = \theta_r + \frac{(\theta_s - \theta_r)}{[1 + (\alpha * |\psi|)^n]^{(m)}} \quad (2)$$

In equation (1), α represents the inverse of matric suction at the inflection point of the soil-water characteristic curve, n characterizes the shape of the curve, m is a fitting parameter, $m = 1 - 1/n$, θ_s is the saturated volumetric water content, and θ_r is the residual water content of the porous media. The ψ in equation (2) is defined in terms of soil water head, h in units of length, (L). Equation 2 can be rearranged to solve for the water content, as:

$$\theta = \theta_r + (\theta_s - \theta_r) * \left[\frac{1}{1 + (\alpha * |\psi_m|)^n} \right]^m \quad (3)$$

In order to parameterize and fit the given data, non-linear regression was used in excel following the protocol outlined in Or and Tuller, (2009).

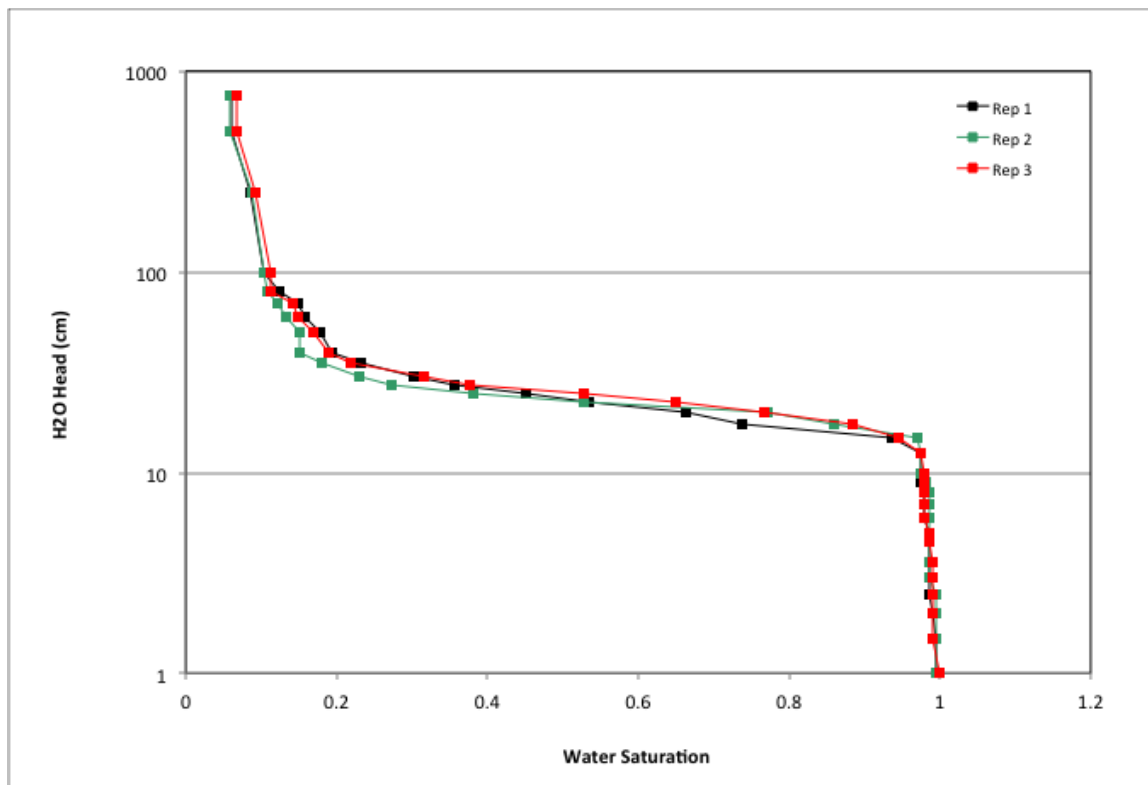


Figure 1: Soil Water Characteristic Curve for 45-50 sand. Rep. 1, 2 and 3 are fitted curves based on van Genuchten (1980) parametric solution model. Fitted parameters, $\alpha= 0.045$, $n= 4$, $\theta_r=0.015$, and $\theta_s=0.294$.

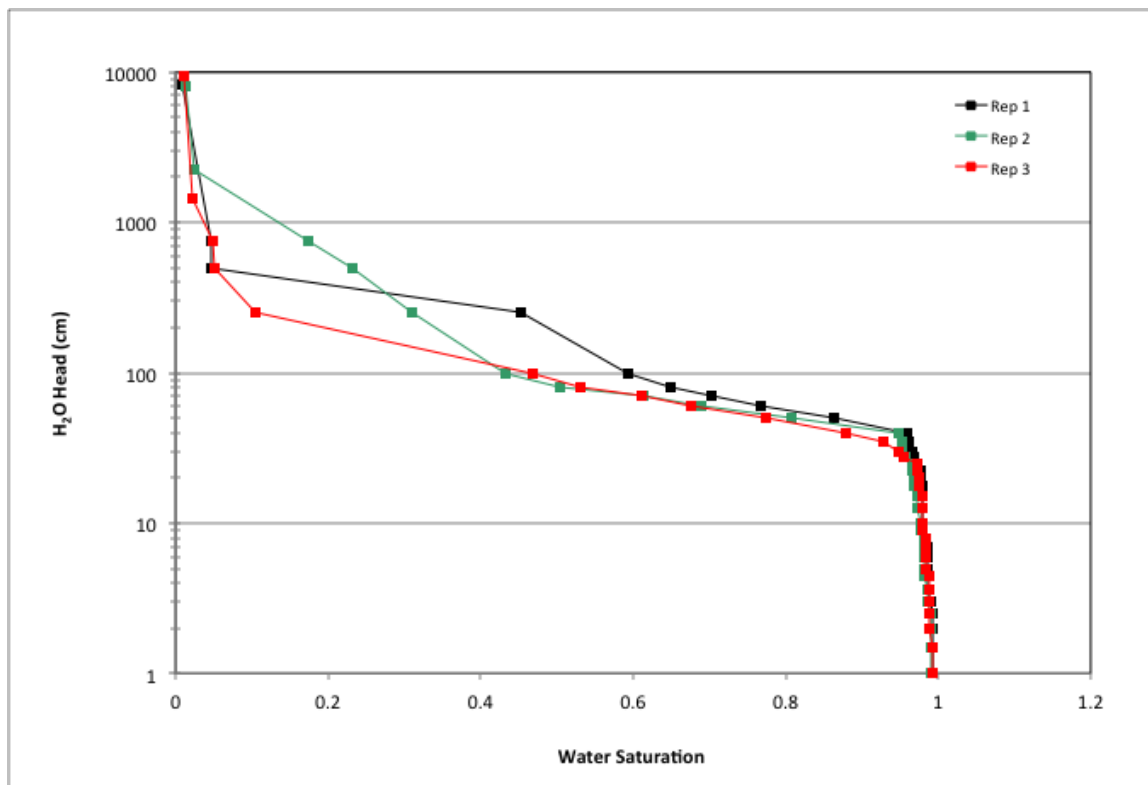


Figure 2: Soil Water Characteristic Curve for Eustis sand. Rep. 1, 2 and 3 are fitted curves based on van Genuchten (1980) parametric solution model. Fitted parameters, $\alpha=0.016$, $n=2.5$, $\theta_r=0.004$, and $\theta_s=0.360$.